Adjustable Inertance Tubes for Pulse Tube Cryocoolers

by

Wenjie Zhou

A dissertation submitted in partial fulfillment of the requirements for the degree of

Doctor of Philosophy

(Mechanical Engineering)

at the

UNIVERSITY OF WISCONSIN – MADISON

2016

This page is left blank intentionally.

APPROVED BY

_____

PROFESSOR JOHN M. PFOTENHAUER

_____

PROFESSOR GREGORY F. NELLIS

DATE:_____

Adjustable Inertance Tubes for Pulse Tube Cryocoolers

Wenjie Zhou

Under the supervision of Prof. John Pfotenhauer and Prof. Gregory Nellis at the University of Wisconsin – Madison

Abstract

Inertance tubes are widely used to adjust the phase angle between the mass flow rate and pressure wave at the cold end of pulse tube cryocoolers for the purpose of improving their performance and optimizing their efficiency. The phase shift mechanism is very sensitive to the dimensions of the inertance tube, such as diameter and length. However, due to variations in fabrication or assembly, it is often uncertain whether the installed fixed dimensions inertance tubes produce the desired phase shift. Therefore, the variable inertance tubes allowing continuous adjustments to their geometry during operation has been constructed and mounted on a linear compressor to explore the phase shift behavior of the inertance tube.

The first chapter summarizes the background and gives a broad review of inertance tubes using in the pulse tube cryocooler. The history of the inertance tube development will be described based on the previous work by other researchers. Also, some key innovation ideas of phase shift mechanism will be discussed. Finally, the objectives and motivation of this research are clearly stated at the end of this chapter.

The second chapter describes the theoretical simulations of the linear adjustable inertance tubes. Details regarding the adjustable length inertance tube are provided along with a description of the mass flow meter and other components utilized in the verification test, including a LabVIEW-based lock-in amplifier. In order to predict the behavior of the linear adjustable inertance tubes, the Distributed Component Model (DCM) is discussed to help the design of the inertance tubes. Based on the distributed component model, the design method of the adjustable inertance tube is generated by using Matlab internal functions. A figure of merit for the different adjustable inertance tubes is also discussed in this thesis. Then, the experimental results are compared with the DCM predictions. Although there are some discrepancies between the measured and calculated phase angle, the trend of its dependence on the length of the inertance tube fits well with the model prediction.

After the simulation and experimental test of the linear adjustable length inertance tube, the design approach and comparison between the conical adjustable diameter inertance and threaded adjustable inertance tube are provided in the third chapter. The chapter provides the design methods of the conical and threaded adjustable diameter inertance tube. Also, details about how to fabricate the prototype of the conical adjustable diameter inertance tube will be described in this chapter. Then, based on DCM simulations, the design of the threaded adjustable inertance tube will be provided. The experimental set-up is given by using the threaded adjustable inertance tube. Details about how to fabricate a physical threaded adjustable inertance, such as Teflon coating, fin heat exchanger around the reservoir and tensile strength of the bolts, are also described in this chapter. By using the threaded adjustable inertance tube, the hydraulic

diameter changes from 7 mm to 10 mm and the length changes from 1.5 m to 3.6 m. The charge pressure and the operating frequency are also varied in order to find the phase shift mechanism of the threaded adjustable inertance tube.

The fourth section describes the modified Distributed Component Model, regarding the leakage and entrance effects from the cylindrical threaded adjustable inertance tube. The calculated model results match the experimental data at different working conditions. The detailed adjustable inertance tube experimental operation procedure and test results are illustrated in this chapter.

The fifth chapter summarizes the entire adjustable inertance tube model and experimental results. Because of the leaks and entrance effects inside the threaded adjustable inertance tube, some recommendations on how to reduce the leaks are proposed such as, increase the engagement length of the thread and generate another inertance tube in parallel. Also, an adjustable inertance tube design tool based on the modified distributed component model is also discussed in this chapter for the convenience of future researchers.

Acknowledgements

During my Ph. D. study in University of Wisconsin Madison, I owe a great number of thanks to my professors, colleagues, and friends in my life. My research and life would not be so enjoyable without their help.

To begin with, I would like to show great thanks to my advisers: Prof. Dr. John M. Pfotenhauer and Prof. Dr. Gregory F. Nellis. Thanks for helping me revise the papers and my Ph. D. thesis. Thanks for your patience and great help when I submitted the CEC/ICMC 2013 conference paper late in the night at Anchorage, Prof. Pfotenhauer. Thanks for your prompt reply every time when I met problems in my research, Prof. Nellis. Thanks for the useful discussion every Tuesday with both of you so that I can figure out problems and solve them very quickly. Thanks for assigning me different Teaching Assistant positions, so that I can learn how to communicate with people nicely and mentoring my students to learn new knowledge. Also, thanks very much for your strong support on my research and future career. I learned a lot from both of you not only on my study and research, but also on my life and personal character building, which will benefit me deeply in my future career and life.

Also, I would like to say thank you to Prof. Dr. Sandy Klein, Prof. Dr. Franklin Miller, and Prof. Dr. Douglas Reindl for your great help and discussion on my research. Thanks for holding the SEL seminar every other Tuesday to let us share our research progress and problems and also practice our presentation skills, Prof. Klein. Thanks for your useful recommendations and discussion on my research and future career searching,

Prof. Miller. Thanks so much for letting me join your Ammonia Safety course and forum for preparation of my future career, Prof. Reindl.

I would like to express my greatest gratitude to Mike Hughes, David Arawinko and Joel Ballweg for many valuable discussions and fabrication of the threaded adjustable inertance tube. Thanks for your time, effort and help on the drawings discussions and your great machining skills on fabricating the pieces for the experiment, Mr. Mike Hughes. Also, my great thanks to Jim Maddocks and Patrick Maddocks for your help on my experiment, each time I messed up with something in the lab, you were always willing to help me solve the problems and arrange the experiments.

The colleagues and scholars in the Solar Energy Lab have made my work over the past five years so enjoyable. Thanks to Xiaoqin Zhi, Dongsheng Zhang, Renzhuo Wang, Qicong Wang, Diego Fonseca, Frederick Schwartz, Dan Schick, Eric Alar, Rodrigo Barraza, Mike Cheadle, John Edlebeck, Mark Rodarte, Russell Knudson, and Doug Gavic for helping me when I have some trouble in my experiment, study and research. With your help, my life in SEL was very comfortable and enjoyable. Thanks for my great officemates Amy Van Asselt, Evan Sheehan, and Chris Hummel for generating a great environment for study and research. Thanks to our awesome colleagues in SEL making the lab a warmly community: Yan Yan, Ana Dyreson, Jack Hinze, Christian Herrera, Patrick Hruska, Courtney Leeds, Rachel Felber, Mason Mok, Brennan Fentzlaff, Amanda Pertzborn, Amir Jahromi, John Dyreby, Soenke Teichel, Brad Moore, Avi Friedman, Nathan Haggerty, Kelsey McCusker, Kyle Rule, Katheryn Yoder, Joe Shinners, etc.

Thanks to Prof. Dr. Christopher Rutland, Prof. Dr. Michael Corradini for serving on my committee.

Last but not least, thanks to my family and friends that helped me to have a happy time during my study abroad in USA. Thanks to my mom, dad, and my sister's encouragement during my study abroad. It was a challenge for me at beginning but leaving my back to you makes me feel undefeated. Thanks to my great friends, Jian Gong and Mingwei Yuan, David Lopez and Noi, Jerry Lehman and Marilyn Lehman, Jean Rene, Ann Rulseh and Tom Rulseh for accompany with me in a lot of enjoyable activities in Madison. Thanks to all the people I didn't mention but helped and smiled to me before. Thank GOD.

Table of Contents

List of Figures

List of Tables

List of Variables

Nomenclature

a	empty space between each fins
C_{ent}	leak discharge coefficient
Cp	constant pressure specific heat
D	diameter of the inertance tube
f	operation frequency
f_{lk}	friction factor of the leak passage
FOM	figure of merit
h	over all heat transfer coefficient
I	current
k	thermal conductivity
L	length of the inertance tube
L^{+}	length to diameter ratio
m	mass flow rate of the working fluid
N	number of nodes or elements

num total number of turns of adjustable threaded inertance tube

P pressure measurements

Pr pressure ratio

ΔP_{ent} pressure difference through leak passage

q heat transfer rate

Re Reynolds number

Rg universal gas constant of the work fluid

$Span$ pressure or voltage range in the measurement

T temperature

th thickness of the corresponding properties

U Uncertainty

V volume of the reservoir

v velocity of the fluid through the leaks

V_{meas} Measured voltage during the calibration of pressure transducer

W acoustic power

Z impedance of the fluid in the inertance tube

Greek symbols

β	ratio of leak diameter to inertance tube diameter
γ	specific heat ratio of working fluid
ρ	density of the working fluid
ϑ	phase angle difference
σ	critical tensile strength of certain material
μ	viscosity of the working fluid

Subscripts

0	Average or mean value in the system
ac	acoustic power
act	accuracy uncertainty
C	fluid compliance
cal	theoretical predictions
d	pressure amplitude of the oscillation flow
dot	rate value

eff effective diameter

ent entrance effect

exp experimental measurements

fin parameters of the fin heat exchanger

in inner diameter or inlet of the inertance tube

IT inertance tube

L fluid inertia

leak properties of leaks

lk parameter of leaks

max maximum value

min minimum value

n number of nodes in the modified distributed component model

pt pulse tube

pre precision uncertainty

R resistance of the fluid in the inertance tube

res reservoir

vg with vacuum grease on the threads

1 Introduction

1.1 Background

1.1.1 Overview

Cryocoolers are widely used in aerospace applications, environment studies, transportations, medical applications and scientific studies etc., which has resulted in a rapid development of these cryocoolers. There are several refrigerators using different cooling cycles, such as the J-T refrigerator, reverse-Brayton refrigerator, G-M cryocooler, and Stirling cryocooler. G-M cryocoolers and Stirling cryocoolers are regenerative cryocoolers having the merits of simple structure and high efficiency. However, they have moving parts at the cold end, so that the reliability, life, and vibration etc. is restricted. Emerging new applications increase the requirements of the cryocooler, such as high efficiency, high reliability, low vibrations, and resistance to electromagnetic interference, all of which have contributed to the development and improvement of the Pulse Tube Cryocooler (PTC).

PTCs were born in the 1960s[1], but only put into use in the middle of 1980s[2]. In contrast with G-M cryocooler and Stirling Cryocoolers, PTCs have no displacer at the cold tip, replacing it with a hollow tube called the pulse tube. The phase angle between the pressure and flow-oscillations is typically controlled by a phase shifting mechanism at the warm end of the pulse tube. The absence of moving parts in the low temperature region eliminates the sliding wear, mechanical vibration, gap seal and other issues. Therefore, PTCs with their advantage of very low vibration and long life provide the

possibility of replacing the traditional small cryocoolers, and have become the newest member of the cryocooler family[3].

1.1.2 Research background

Similar to the difference between GM cryocoolers and Stirling Cryocoolers, the difference between the G-M PTC and Stirling PTC is that the G-M cryocooler uses a switching valve after the helium compressor while the Stirling PTC uses a linear compressor. FIGURE 1-1 shows the two PTC configurations. The left hand picture of FIGURE 1-1 shows the compressor along with a switching valve to generate the high pressure and low pressure. As shown in the right hand side of FIGURE 1-1, the Stirling PTC, uses a valve-less compressor to generate the approximately sinusoidal pressure wave, and communicates the pressure directly into the cold head without a check valve. Due to the structural differences, the G-M PTC typically operates at a lower frequency, while the Stirling PTC operates at higher frequencies, typically 30 Hz or more. Accordingly, the Stirling PTC is also known as the high-frequency pulse tube cryocooler.

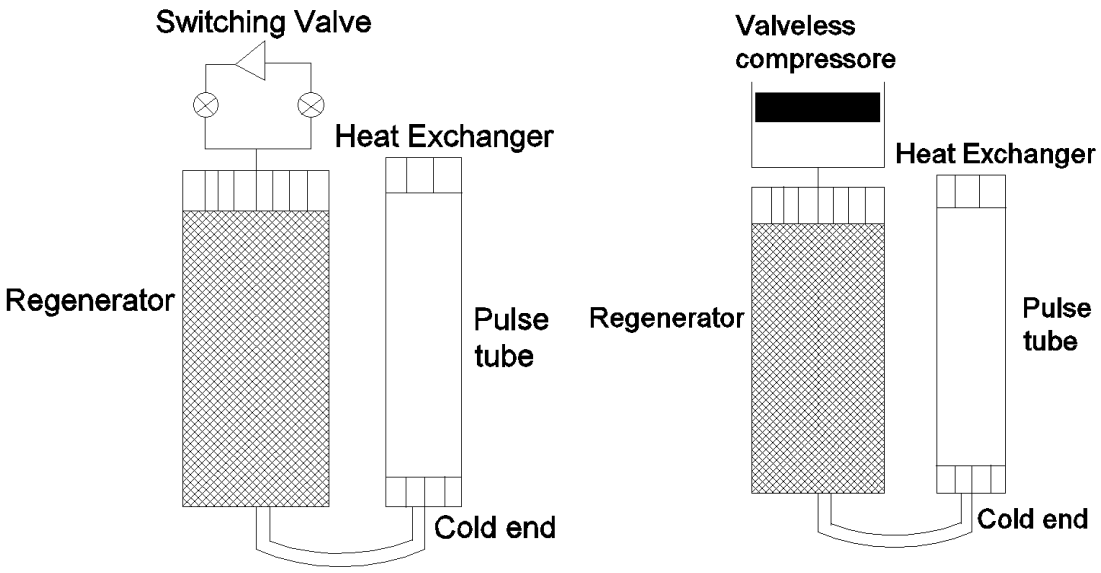

FIGURE 1-1 G-M type PTC (left) and Stirling type PTC (right)

In contrast with the G-M type PTC, Stirling PTCs do not have a switching valve; therefore, they are more compact, have less weight, higher reliability, generate smaller vibration and provide other advantages[4, 5]. Recent research indicates that, in the temperature range above 60 K, its efficiency is significantly higher than the G-M type pulse tube cryocooler.

Table 1-1 The application field of Stirling PTC[6]

Application fields	**Temperature range**	**Cooling power**
Aerospace application, Infrared cameras	50-80 K	0.1-10W
Filters, SQUID, Superconductors	50-80 K	0.1-10W
MRI, SMES, High-Temp Superconductors	BSCCO:20-30 K YBCO: 50-65 K	10-100W

Superconducting generators and motors, current limiter, power storage devices	BSCCO: 25-40K YBCO: 50-80 K	10-1000W
Cryo-condensation pumps, Cryogenic preservation of biological and medical applications	Above 10 K	1-10W

Stirling PTCs have the same application field as the traditional Stirling cryocooler. Table 1-1 summarizes the existing and likely future major application areas for the Stirling PTC, including infrared sensors, high-temperature superconducting devices as well as the production of liquefied cryogenic gases and others[7]. Infrared sensors need to be cooled to 50 – 80 K, requiring several watts or less of cooling capacity. The preliminary considerations for this application are the refrigerator volume, weight, life, vibration, etc. Therefore, it became an early application area for Stirling PTCs. Stirling PTCs have been put into practical use in the space exploration field, and have demonstrated the ability of long-term reliable operation.

Another important application field of the Stirling PTC is to cool high-temperature superconducting materials. Currently, the most promising high-temperature superconducting materials are BSCCO, YBCO and MgB2. As the second-generation high-temperature superconductors, the yttrium-based material works best in the temperature of about 50-80 K. Electronic devices based on type-II superconducting materials, such as filters, SQUIDs, etc. only need watts of cooling capacity. However, superconducting magnets and electric power equipment based on type-II superconducting materials need tens-, hundreds- or even thousands of watts of cooling capacity. In the 80 K region, single stage Stirling PTCs can fulfill the requirements[6].

1.2 The development of phase shifting mechanism for PTCs

1.2.1 Basic PTCs

The pulse tube cooling effect was first accidentally discovered by Gifford and Longsworth at Syracuse University during the development of a GM refrigerator. They noticed that a pressure fluctuation in one end of a closed tube generated heat at this closed end, and a refrigeration effect at the open end. After installing a regenerator and a laminar flow component to optimize the geometry, along with water cooling; the performance of the cooler was significantly improved, achieving a lowest temperature of 124K[1]. FIGURE 1-2 shows the schematic of their basic pulse tube refrigerator. The basic pulse tube cryocooler consists of a compressor, a switching valve, regenerator, cold end heat exchanger, pulse tube, and cooling water component.

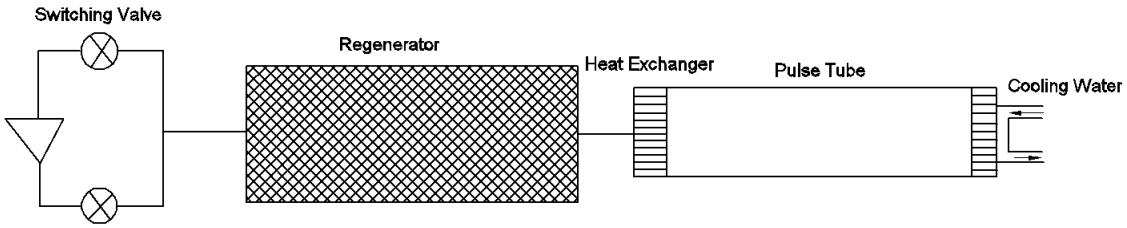

FIGURE 1-2 Schematic of basic pulse tube cryocooler

At the beginning of their experiment, they used a switching valve to generate the high and low pressure oscillations in the pulse tube. This structure is very similar to the GM refrigerator, only missing a displacer, and is therefore called a GM type pulse tube refrigerator. Gifford, noting that the repeated switching of gas flow through the valve of

the GM-type pulse tube cryocooler generated very large flow losses, used a valve-less compressor to replace the switching valve compressor and thereby generated an approximately sinusoidal pressure wave to drive the pulse tube cryocooler. They called this type of cryocooler a reversible pulse tube cryocooler. In fact it is very similar to Stirling cryocooler, only lacking the moving displacer at the cold end, so it is now called a Stirling type pulse tube refrigerator. The efficiency of the basic pulse tube cryocooler turned out to be relatively low, and was not further developed after being first discovered.

1.2.2 Orifice phase shifting mechanism for PTCs

The basic pulse tube cryocooler did not generate much interest because it was relatively inefficient and demonstrated significantly poorer performance than Stirling and GM refrigerators. In 1984, Mikulin[2] from Moscow Bauman Technical College added a hole and reservoir at the hot end heat exchanger of the pulse tube. Using air as the working fluid, he achieved a cold tip temperature of 105 K. The introduction of gas storage and holes increases the mass flow going into and out of the pulse tube, and strengthens the heat transfer at the hot end of pulse tube, which improved the performance of the pulse tube greatly. This form is called an orifice pulse tube refrigerator.

In 1985, Dr. Radebaugh etc. moved the hole outside of the hot end heat exchanger and used a needle valve to replace the hole, allowing an adjustment of the valve during runtime. He used helium as working fluid, and achieved a lowest temperature of 60 K[8]. FIGURE 1-3 shows the schematic drawings of the orifice-type PTCs. In 1989, Dr. Liang

from the China National Academy of Cryogenic Center optimized the structural parameters of the pulse tube, and improved the structure of the hot end heat exchanger, enabling the orifice pulse tube refrigerator to reach the low temperature of 49K and provide 12W of cooling at 77K.

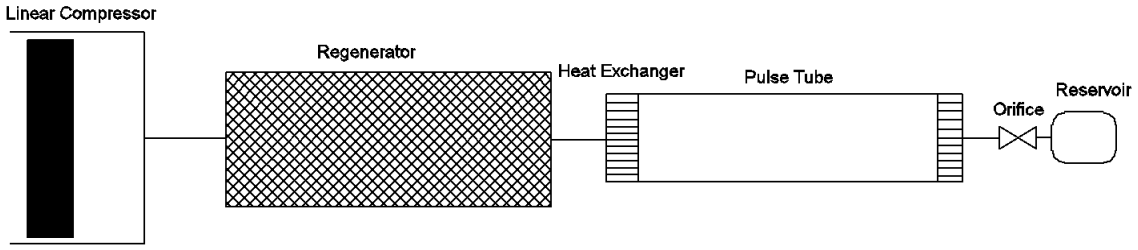

FIGURE 1-3 Schematic of Orifice-type PTCs

1.2.3 Double-inlet and Multi-bypass PTCs

In 1990, Dr. Zhu Shaowei and Dr. Wu Peiyi found that a portion of the mass flow going through the cold end does not produce a cooling effect, thereby restricting the efficiency of pulse tube cryocooler. Therefore, they introduced the concept of a second valve connecting the pulse tube hot end and the compressor. Because of the second flow path, a portion of the working fluid goes directly to the pulse tube hot end, thereby decreasing the regenerative loss. This type of PTC is called a double-inlet pulse tube refrigerator, and is shown in FIGURE 1-4. In order to get a high performance of pulse tube cryocooler, one typically wants the phase angle between the flow and pressure oscillation to be zero in the middle of the regenerator, and therefore one desires a negative phase angle at the cold end of the pulse tube. Analysis showed that the phase angle between the mass flow rate and pressure wave at the cold end of a double-inlet

PTCs can be further reduced to +10°. Thus, it has a large performance improvement compared to Orifice-type PTCs.

Dr. Zhu Shaowei[9] used the double-inlet pulse tube refrigerator to achieve 42 K low temperature, which set a new record for the lowest PTC temperature. The performance of the double-inlet PTC has been very close to or even better than traditional GM refrigerators and Stirling coolers, an observation that greatly promoted the practical application of PTCs. During the 1990's many PTCs adopted the double-inlet configuration as the phase shifting device. In particular, several GM type PTC products with double-inlet structure have been put into the market.

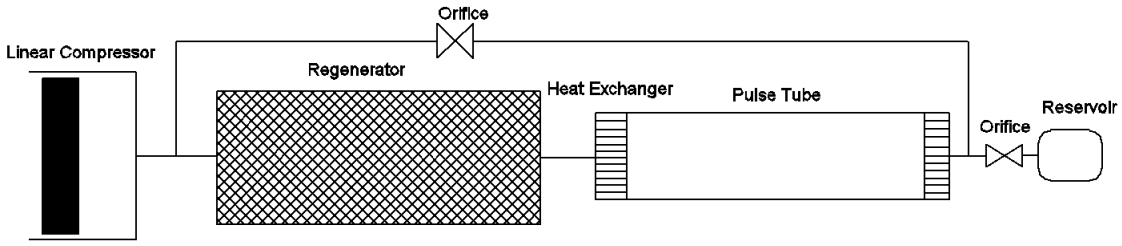

FIGURE 1-4 Schematic of Double inlet PTCs

However, along with the introduction of a double-inlet valve, a secondary DC flow path is formed from the regenerator to the pulse tube hot end through the double-inlet orifice leading to a thermal loss mechanism. Although the portion of DC flow is quite small, it has a significant influence on the performance of the cryocooler. A large amount of cooling power transfers from the cold end to the hot end by the DC flow, and deteriorates the refrigerating performance. Prof. Chen Guobang[10] from Zhejiang

University developed a double orifice type scheme, connecting the compression chamber and reservoir to regulate the ratio of the DC flow. The method using a pair of reverse-direction needle valves mounted in parallel very effectively controls the DC flow in the GM type PTC [11-13].

1.2.4 Inertance-type PTCs

In 1994, Kanao etc.[14] reported using a long neck tube instead of the small orifice between the reservoir and pulse tube, and were able to achieve a decrease in the no-load cooling temperature from 127 K to 114 K. In 1996, Godshalk[15] identified an effective phase shift in the pulse tube when running a 350 Hz orifice pulse tube cryocooler. Therefore, they realized that the inertial effect can be used to regulate the phase angle between the mass flow and pressure oscillations. This inertial effect can be further strengthened by connecting the pulse tube and reservoir with a long neck tube, which is called an inertance tube. FIGURE 1-5 shows the details of the inertance tube type PTC. Theoretical analysis and experimental results indicate that the inertance tube not only has a strong phase shifting capability, but also can amplify the pressure ratio in the pulse tube. Because there is no loop structure, it also eliminates the DC flow associated with the double-inlet pulse tube refrigerator.

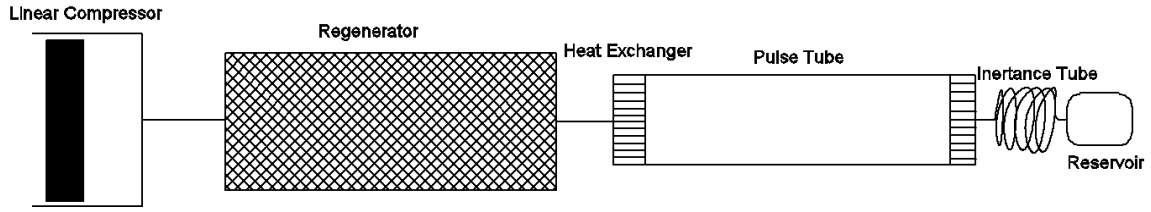

FIGURE 1-5 Schematic of inertance tube type PTC

Gardner and Swift[16] from Los Alamos National Laboratory used an acoustic-electric analogy method to analyze the inertance tube phase modulation effect, noting that the inertance tube can provide a wide range of phase shift angles, not only for high-power pulse tube refrigerators, but also to some degree for small compact pulse tube refrigerator phase shifting requirements. Phase analysis showed that the phase shifting capability of an inertance tube cryocooler is much higher than the double inlet PTCs, making the equivalent PV diagram at the cold head close to the PV diagram of Stirling type PTCs. By now there are some commercial products using inertance tubes as the phase adjusting device for PTCs.

1.2.5 Other phase shifting forms

In 1988, Matsubara[17] proposed a dual-piston type pulse tube refrigerator. It had some similarities to the Stirling PTC, because it had a piston at the hot end of the pulse tube. A piston at the hot end can actively modulate the phase angle, reuse the expansion work and eliminate the irreversible loss at the orifice, and therefore increases the efficiency of the PTCs. Compared to the Stirling Cryocooler, the double piston PTC moves the expansion piston from the cold end to the room temperature end, increasing the reliability of the pulse tube cryocooler. In 1992, Ishizaki etc[18] used the double

piston PTC to achieve the lowest temperature of 23.5 K. A dual piston type pulse tube refrigerator is only applicable to Stirling type PTCs.

In 1996, Tanida etc[19] developed a four valve pulse tube refrigerator. The hot end of the pulse tube was connected to the compressor by a switching valve and a flow regulating valve. The four valve pulse tube cryocooler appears more compact than the double inlet PTC because the reservoir is eliminated. In 1998, Li Rui and Kanao developed a single stage four valve pulse tube refrigerator reaching the lowest temperature of 20.5 K, and able to provide 33.5W of cooling capacity at 80K.

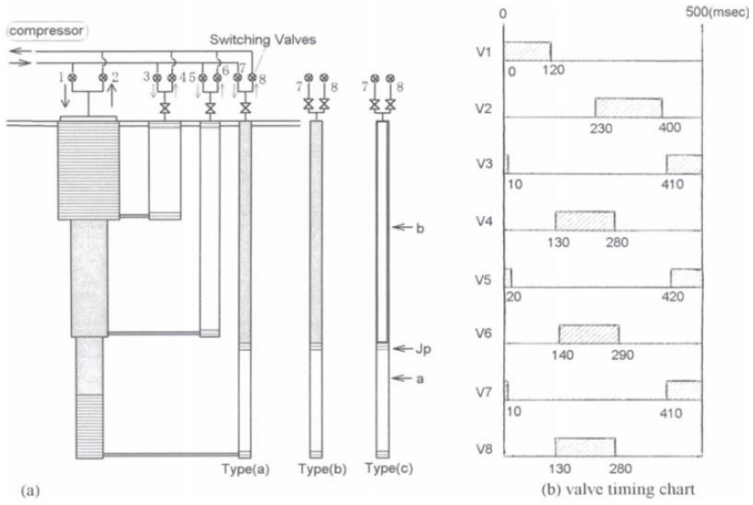

FIGURE 1-6 Three stage pulse tube refrigerator by Tanida[19]

In 1996, Zhu Shaowei[20] invented an active buffer pulse tube cryocooler in which multiple reservoirs (buffer tanks) connect to the hot end of the pulse tube. By controlling the timing of valves between the buffer tanks and the pulse tube, the working fluid flows into and out of the reservoirs with different pressures and a modulated phase

angle. Irreversible losses from the cold and warm end of the pulse tube are reduced, and the efficiency of the pulse tube refrigerator is greatly improved. With 3.65 kW of electric power input, this configuration achieves a no-load temperature down to 28 K, and generates 160 W of cooling power at 80 K with 11% of Carnot efficiency. Because of the use of switching valves to connect the high and low pressures, the four valve PTC and the active buffer PTC can only be used on the GM type pulse tube refrigerator.

Some researchers have tried using a liquid column to increase the acoustic inertance because of the larger density of the liquid compared to that of the gas[21]. FIGURE 1-7 shows the geometry of the liquid displacer in the form of a U-tube from C. D. West's paper in 1983[21]. The liquid in the U-tube serves as an acoustic power output component in a Stirling engine, and could be used as an acoustic power consumption term in the pulse tube cryocooler to adjust the phase angle at the warm end of the pulse tube.

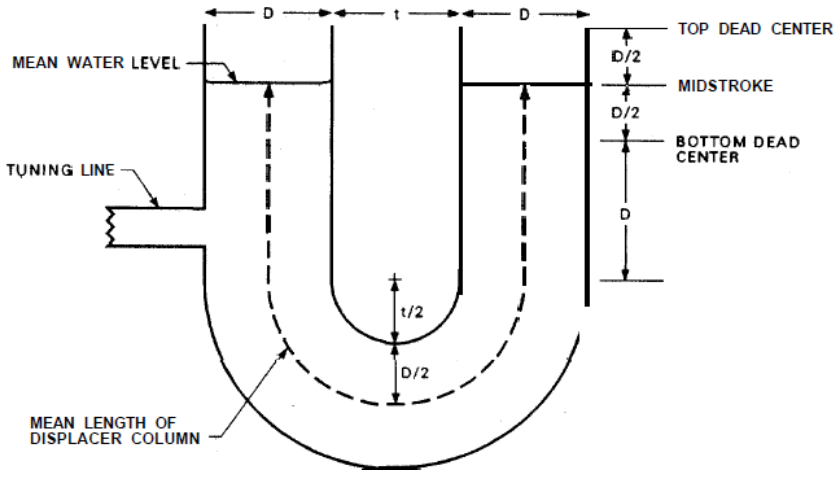

FIGURE 1-7 Geometry of liquid displacer in U-tube[21]

Another idea is to use the liquid piston inside a thermoacoustic engine as reported by Tang [22] in 2009, whose geometry is shown in FIGURE 1-8 below. The liquid in the U-tube provides an extra acoustic inertance in the thermoacoustic engine. The engine with a liquid water column operates with a relatively low resonant frequency, less than 10 Hz, and a higher amplitude in the pressure oscillation with a much shorter resonant tube. This liquid U-tube could also be the phase shifter in a pulse tube cryocooler.

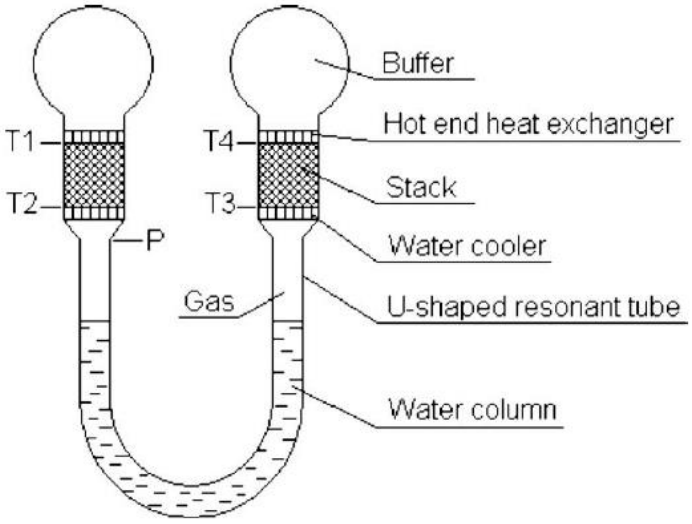

FIGURE 1-8 Schematic of Thermoacoustic engine using liquid column[22]

Mike Cheadle introduced a phase shifting mechanism by using a current damper and bellows[23]. The configuration of his active phase shifter is shown below. The damping for the phase shifter is provided by an eddy current damper and can be controlled via an applied external magnetic field that provides active real-time phase control.

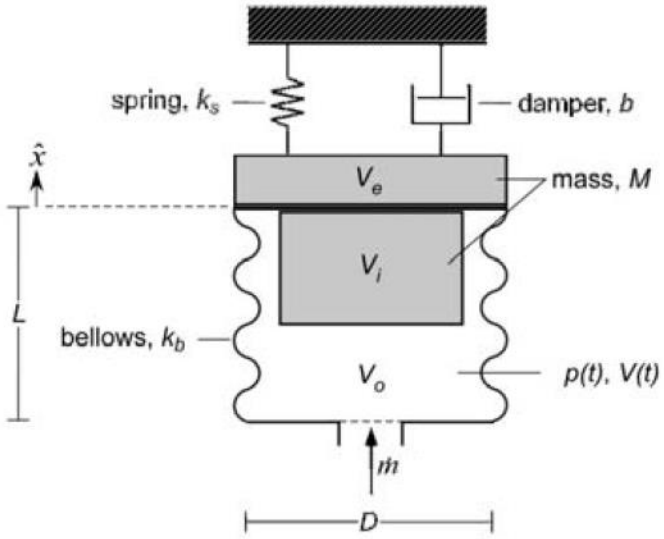

FIGURE 1-9 Mechanical phase shifter at equilibrium condition[23]

1.3 Previous work on the inertance tube

1.3.1 Brief history of the inertance tube

Inertance tube PTCs use the inertia of gas flow through the inertance tube to modulate the phase angle between the pressure and mass flow oscillations. The inertance tube can provide a large phase shift without increasing the electric power input. Also, the inertance tube will not enable the DC flow losses that can exist in the double inlet orifice refrigerator. For this reason, the inertance tube is the most widely used phase shifting mechanism for Stirling type PTCs.

The inertance tube was first used in the pulse tube refrigerator in 1994 by Kanao from Japan[14]. In the experiment, they first used a long-neck tube to connect the hot end

of the pulse tube to the reservoir. The lowest temperature obtained was 98 K with 60 W of input power. An optimum tube length was also found in the experiment. Including a needle valve on the same refrigerator did not improve the performance. Since then, this long neck tube has been used extensively to fix the phase between the pressure and mass flow oscillations in the high frequency PTCs. FIGURE 1-10 shows a picture of the first pulse tube refrigerator using the inertance tube as a passive phase shifter.

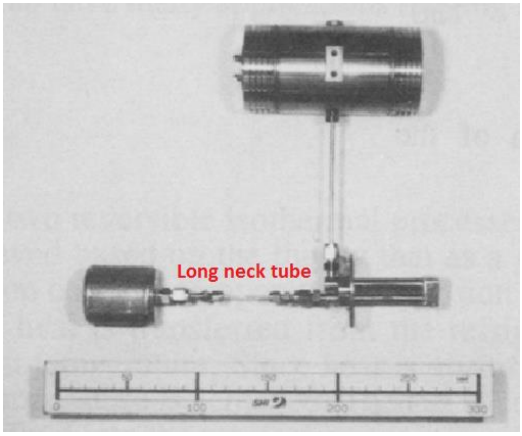

FIGURE 1-10 Photo of the first inertance tube PTC[14]

Haruyama and Inoue reported the investigation of a miniature pulse tube refrigerator with a flexure spring compressor in 1995[24]. They achieved a lowest temperature of 99.6 K by using a capillary tube between the pulse tube and the reservoir. They indicated that the cold end temperature was still 50K higher than that of the Stirling refrigerator, and thus, the cooling mechanism and losses peculiar to the capillary miniature pulse tube should be further studied.

In 1996, Zhu[20] announced that the long neck tube can obviously improve the performance of the PTC, because it can generate a larger phase shift than either the

orifice or double inlet configurations. He also compared the performance of an orifice pulse tube with that of an inertance tube PTC. In the case of the orifice pulse tube, the phase shift effect generated by the orifice and reservoir is not adequate. The double inlet could approach the PV shape of the idealized Stirling cycle, but that configuration requires additional work input. From their computer simulation, they concluded that the long neck tube with a reservoir provided an improved PV diagram with no additional work.

Gardner and Swift[16] introduced a lumped component model to describe the complex impedance inside the inertance tube. The phase shift between the oscillating pressure and oscillating velocity at the cold end can be shifted to the more efficient Stirling values by adding an inertance in series with the orifice. The term inertance refers to the inertial effects of moving gas and is the acoustic analog of an electrical inductance. Roach[25] used a simplified electrical analogy to show the advantages of using a long neck tube in the design of a pulse tube refrigerator. The lumped component model introduced by Gardner and Swift showed that the geometry of an optimized inertance tube depends primarily on the volumes in the refrigerator system and not on the impedance of the regenerator. Hofmann[26] provided a simple means for finding the optimum phase shift between pressure and flow oscillation for PTCs operated with different kinds of phase shifters such as the orifice system, the inertance tube, and the double inlet arrangement.

In 2001, Hou[27] presented results from an experimental study on a high frequency miniature pulse tube refrigerator with an inertance tube. From the experiment, they found that the benefit of using only an inertance tube was not apparent in a miniature PTR. The lowest temperature achieved by the inertance tube PTC was only 107.3 K, which is higher than the lowest temperature of 101.6 K achieved by the bypass PTCs.

Luo *et. al*[28], in 2004, developed the laminar flow thermoacoustic transmission line model and a turbulent flow thermoacoustic model that accounts for both turbulent flow and heat transfer. In order to verify the accuracy of the models, experimental measurements were carried out with frequencies between 20 Hz and 90 Hz and with the acoustic power flows less than about 50 W. The turbulent flow model agrees reasonable with the experimental results for most of the experimental conditions.

Park *et. al*[29] also did an experimental study with a coaxial inertance tube pulse tube refrigerator. The pressure ratio in the pulse tube decreases as the inner diameter of the inertance tube increases. Thus the inner diameter of the inertance tube has more significant effects than the length on the performance of a PTC, and an inertance tube with a larger inner diameter may be improper for the PTC. Also, the author did not provide the acoustic power match between the pulse tube side and the inertance tube side.

Flake *et. al*[30, 31] presented an analytic solution for incompressible oscillatory flow in an infinite tube to find the phase shift between pressure and mass flow. They also demonstrated a capability for CFD predictions of inertance tube performance. The CFD results match with analytic prediction for the case of incompressible flow.

Lewis *et. al*[32-34] developed a measurement technique using a hot wire anemometer to measure mass flows at the inlet of an inertance tube and the phase shift with respect to the compressor pressure. The experimental results for the impedance of an inertance tube were compared with a transmission line model. The results showed that the transmission line model predicted the impedance values about 25% lower than the measured values. They also provided various methods for mass flow measurements at the inlet to the inertance tube, such as hot-wire anemometry, the pressure drop across stacked screens, and the pressure drop across a laminar flow element. He also tested a set of frequencies: 50, 60, 70 Hz; and reservoir volumes: 30, 83, 134, 334 cm^3. The experiments agreed well with the model and confirmed the existence of the resonance condition at the reservoir volume predicted by the model.

Schunk L. O., Nellis G. F. and Pfotenhauer J. M.[35] reported a new distributed component model to predict the behavior of the inertance tube. The inertance tube is divided into a large number of increments; each increment is associated with a resistance, compliance, and inertance. The model predictions demonstrate a relatively good agreement with the experimental measurements over a large range of operating conditions.

Dai *et. al*[36] compared two different ways of using an inertance tube in a pulse tube cryocooler, which is shown in FIGURE 1-11 left. In the paper, they note that an inertance tube with or without a reservoir produce similar results and both produce much better results than the orifice configuration. The configuration of a pulse tube using an

inertance tube without a reservoir is more compact and can reduce the amount of gas required to charge the system. Masuyama *et. al*[37] reported an active phase control device in 2005. They placed an electrically driven and mechanically damped linear compressor at the end of the orifice as an active phase shifter. The cool down characteristic of this active phase controller PTC is similar to the inertance tube PTC. The lowest temperature of 96.3 K was obtained when the orifice was attached between the warm end of the pulse tube and the active phase controller. The schematic diagram of this active phase shifter PTC is shown in FIGURE 1-11 right.

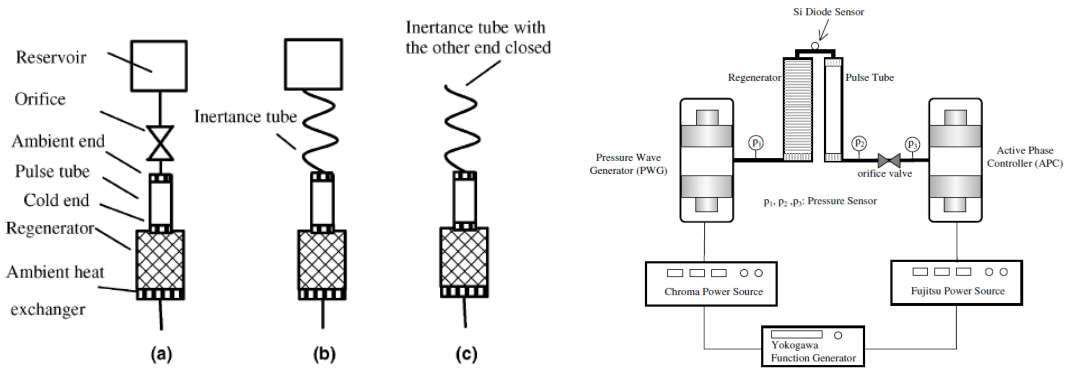

FIGURE 1-11 Dai's inertance tube without reservoir (left) and Masuyama's active reservoir

Gan *et. al*[38-40] reported a two stage Stirling pulse tube cryocooler with a cold inertance tube. In their experiment, a lowest cooling temperature of 23.7 K and a cooling power of 0.5 W at 33.9 K were obtained with an input electric power of 150 W and an operating frequency of 40 Hz. Their data demonstrated the significant result that the increased density of the cold helium gas in the inertance tube allows a system with even a small acoustic power to have a significant phase shift from an inertance tube.

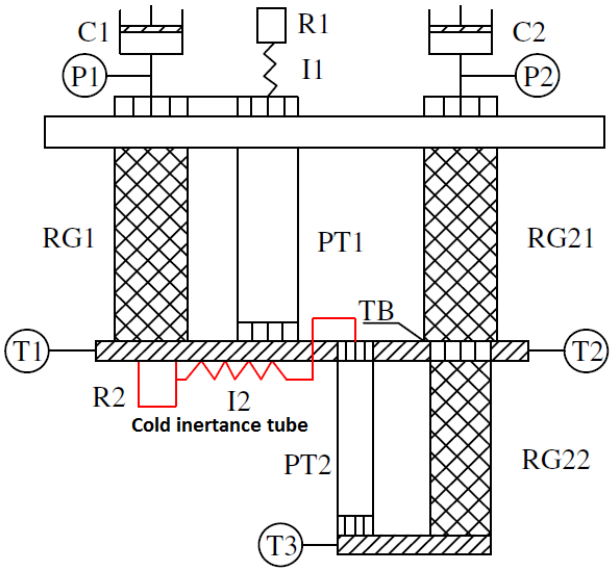

FIGURE 1-12 Schematic of Gan's cold inertance tube PTC[38]

1.3.2 Phase angle measurement in the inertance tube

The objective of the inertance tube is to adjust the phase angle in the middle of the regenerator to be zero degree in order to optimize the performance of the cryocooler. The phase characteristic is important for the performance and efficiency of the refrigerator. It is relatively difficult to measure the phase angle inside the refrigerator, due to the oscillating flow. Reports by Radebaugh[41], Storch[42], Rawlins[43] describe methods to measure the phase angle.

Dr. Radebaugh[41] used the enthalpy flow phase modulation theory, which is based on the conservation of mass and energy, to qualitatively analyze the phase angle inside the orifice PTC and Stirling cryocooler. The orifice is a purely resistive element, and the mass flow is at the same phase with the pressure wave in the orifice; as a result,

in the orifice pulse tube refrigerator, the mass flow at the center of the regenerator leads the pressure wave. In the Stirling cryocooler, both the compressor and expander can be directly controlled in order to modulate the phase angle at the center of the regenerator. Because the orifice is only a resistive element in the pulse tube, it decreases the efficiency of the pulse tube refrigerator.

Storch and Radebaugh[42] carried out experiments to measure the mass flow and refrigeration power, noting that refrigeration power is proportional to the average pressure, the pulse tube frequency, the mass flow ratio, and the square of the dynamic pressure ratio. They compared their experimental results with predictions from their phasor analysis model, finding that as the result of the simplifying assumptions, the magnitudes of the refrigeration power from the phasor model were between 3 and 5 times greater than experimental values. Rawlins and Radebaugh[43] measured the instantaneous mass flow (using a constant temperature anemometer) and temperature in the orifice pulse tube refrigerator. The measurement results are compared with the enthalpy flow model prediction. The enthalpy at the cold end from the experiments is about 60-85% of the model calculation. In subsequent studies these authors used this method of measuring the mass flow rate to study phase shifting in pulse tubes[32].

Ju *et.al*[44], in 2003, measured the flow resistance and flow inductance of inertance tubes at high acoustic power. They measured the flow resistance and flow inductance of the inertance tubes at high acoustic power with different inner diameters and various length and operation frequency. From their experimental results, they saw the

difference of the flow resistance and flow inductance of inertance tubes at low and high acoustic power.

Bradley et. al[45] carried out a series of experiments on the phase characteristics of the PTC working for the medical probe at 180 K. They measured the displacement of the compressor, and the pressure at the compressor outlet, the hot end of the pulse tube and at the reservoir. They used these simple measurements to find the mass flow, pressure and acoustic power inside pulse tube. The calculated mass flow agrees well with their model predictions, and the simple test method can be used to evaluate the design of the key components of the PTC, compressor and inertance tube.

Pfotenhauer *et. al*[46, 47] used a mass flow meter to detect the mass flow rate at the inlet of the inertance tube. They mounted two pressure transducers at the warm end of the pulse tube. A set of copper screens are positioned between the two pressure transducers (P1 and P2). Since the mass flow rate is in phase with, and proportional to, the pressure difference between the two pressure transducers, the phase angle of the mass flow rate is equal to the phase difference between P1 and (P1-P2). The mass flow meter used in our experiments is also the same as the mass flow meter described in these two papers.

1.4 Research significance and motivation

From the previous research, we can see that the inertance tube is a key component for increasing the performance and efficiency of the PTCs. The orifice is only a resistance element in the fluid network, and cannot provide a sufficiently large phase

angle shift in order to optimize the performance of the pulse tube. The inertance tube introduces resistance, inductance, and compliance together in the pulse tube refrigerator, and has a very strong phase shifting ability. Therefore, the inertance tube has been a very hot topic in pulse tube refrigerator research.

Furthermore, the phase angle produced by the inertance tube is sensitive to the length and diameter of the inertance tube in certain ranges of tube lengths and diameters, and is insensitive to the same parameter in other ranges of the lengths and diameters. The acoustic wavelength of the operating fluid plays a significant role in the periodicity of this feature[46]. Because of this sensitivity, and the significance to the pulse tube cooling power of the phase shift produced by the inertance tube, one may easily recognize the convenience of using an inertance tube whose length, diameter or both could be continuously adjustable. Also, in some cases, the calculated phase shift for a specific inertance tube can be different than that realized by the same tube in the experiment set-up due to various fabrication or assembly factors. Finally, as noted by Radebaugh[48], the optimum phase angle during the cool down of a pulse tube refrigerator is typically not the same as the optimum phase angle for steady state operation.

Because of the significance of the inertance tube in the PTCs and the above issues, it must be fairly beneficial to use an easily variable inertance tube and the associated variable phase angle. However, in the real experiment, the process of replacing one tube of a given length and diameter with another usually requires shutting down the entire experiment, waiting for the cold end to warm to room temperature, and then

depressurizing and disassembling the entire system. Following the replacement of one inertance tube with another, the system must be reassembled, evacuated, leak checked, and repressurized before it can be re-cooled. Such a process is time consuming and complicated. In order to avoid this complicated procedure and provide an approach for adjusting the phase angle, we have explored an adjustable inertance tube that allows real-time continuous adjustment while the pulse tube is operating. Three different versions of adjustable inertance tubes have been investigated: a linear adjustable inertance tube, a conical adjustable inertance tube and a threaded adjustable inertance tube. The linear adjustable inertance tube and threaded adjustable inertance tube were fabricated in order to experimentally measure the phase angle at the beginning of the inertance tube and compare the experimental results with the theoretical predictions.

2 Linear Adjustable Inertance Tube

2.1 Distributed component model[35]

The distributed component model is introduced to characterize the inertance tube as a function of its diameter and length[35]. In the distributed component model, the inertance tube is separated into several segments. Typically, the oscillation flow impedance inside the inertance tube is regarded as the combination of a fluid resistance R, compliance C, and inertance I. Because of the physical characteristics of the inertance tube, it may be more appropriate to call this long neck tube an “Impedance Tube” rather than an “Inertance tube”. The reservoir is regarded as a fluid compliance (Z_res_C) combined with a resistance that stands for the entrance effect (Z_res_R) associated with the fluid expansion and contraction at the reservoir inlet and the pulse tube side of the inertance tube. There are n segments of the inertance tube as shown in FIGURE 2-1.The i^{th} section of the inertance tube has inertance impedance Zi_L in series with resistance impedance Zi_R, and these are in parallel with the compliance impedance Zi_C. The mean pressure P0 and pressure amplitude Pd_pt are given as the boundary conditions.

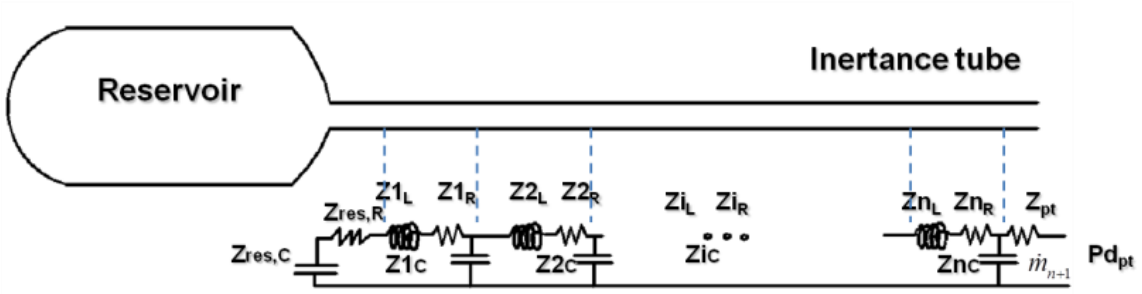

FIGURE 2-1 Schematic diagram of Distributed Component Model

There are a number of benefits of using the distributed component model. To begin with, it considers the entrance effect associated with the expansion and contraction of the gas as the working fluid goes in and out of the reservoir and pulse tube. It also accounts for the spatial variation in the flow conditions along the tube by varying the characteristics of the impedance components according to the local conditions.

The inputs to the distributed component model are the average pressure P_0, the pressure amplitude P_d at the inlet of the inertance tube, the inner diameter D_{in} and length L of the inertance tube, and the frequency ω of the oscillations. Nominal values for these parameters, used within the present report, are shown in Table 2-1(the length, L, and diameters, D_{in}, are varied). With these inputs and the known fluids properties, the mass flow, acoustic power, and also the phase shift at each node of the inertance tube can be easily calculated. The details of the Distributed Component Model for the adjustable inertance tube can be found in Schunk L. O., Nellis G. F. and Pfotenhauer J. M.[35].

Table 2-1 Input parameters for distributed component model

P0 (pa)	2.07e6	Frequency (Hz)	50
Pd (pa)	2.28e5	T (K)	293
D_{in} (m)	6e-3	V_{res} (m^3)	1.5e-3
L (m)	2.5	N	100
Rg(J/kg-K)	2077	C_p(J/kg-K)	5192
μ (pa-s)	1.968e-5	ρ (kg/m^3)	3.4

FIGURE 2-2 the flow chart illustrates the algorithm of the calculation method. The basis parameters, which are shown in Table 2-1, are entered into a Matlab code. The inertance tube is divided into n nodes. In order to set up the entire fluid circuit of the inertance tube, the Reynolds numbers for each node are estimated at the beginning of the program. Since we know the impedance of each node and the pressure amplitude at the pulse tube side, Kirchhoff"s Law is applied to find the mass flow rate and new Reynolds numbers for each node. The new Reynolds number at each location is subtracted from the old Reynolds number, and if the error between those two is smaller than ε, which is about 10e-10, then we can jump out of the 'while' loop to continue the calculation of phase angle and acoustic power consumption by the inertance tube.

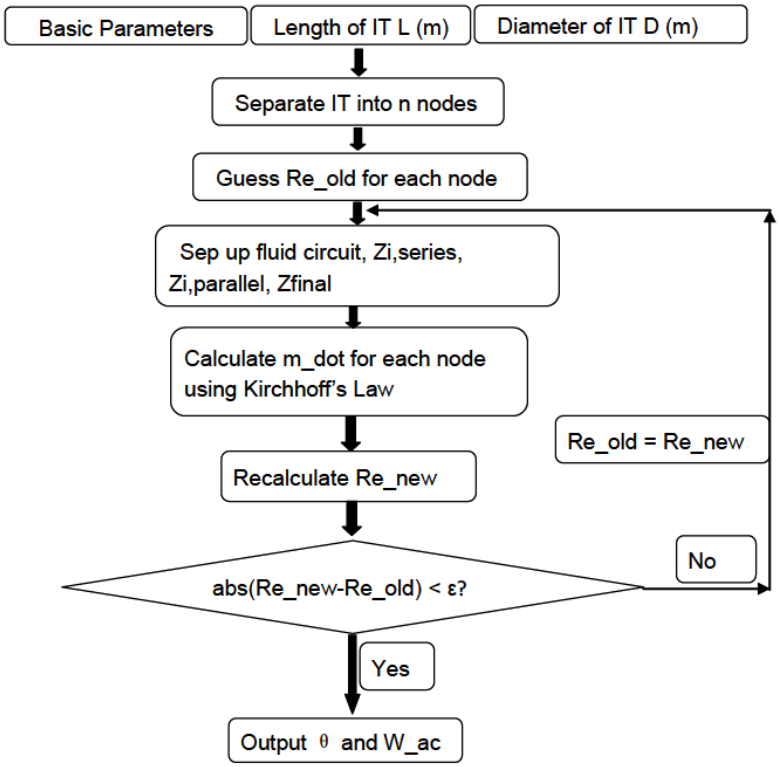

FIGURE 2-2 Flow chart of distributed component model

A sensitivity study has also been carried out that addresses the total number of nodes n, that is, the number of components used to model the inertance tube. From FIGURE 2-3, we can see that, if the total number of segments approaches 100, both the phase angle and the acoustic power approach stable values. Thus, the number 100 has been used in this study of the adjustable inertance tube.

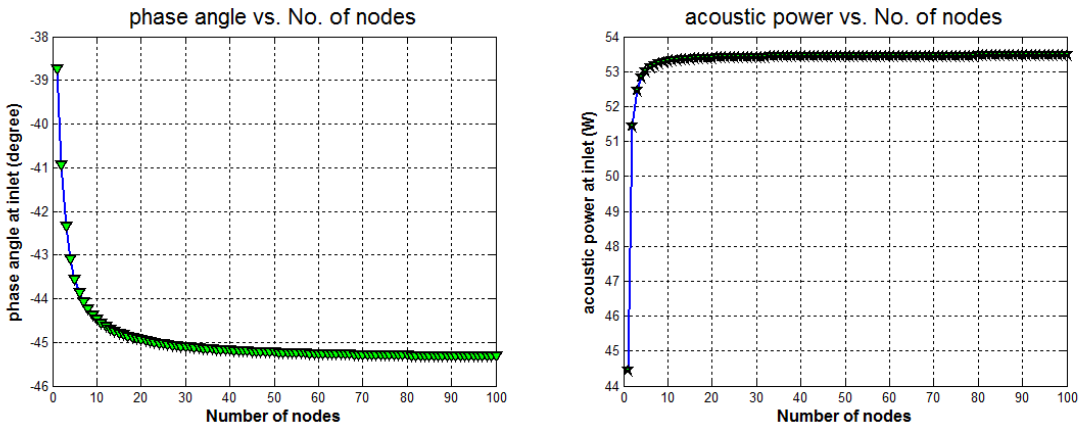

FIGURE 2-3 Sensitivity study determining total node n for the model

2.2 Multi-section Distributed Component Model

A single-section distributed component model is introduced by Schunk (2005). However, as is typical in many experimental situations, two tubes or three tubes with different diameters are also used in order to acquire the desired phase angle shift. Therefore, a multi section distributed component model is also utilized in this work. The boundary conditions for the multi-section inertance tubes are different from the single-section inertance tube. The geometry and fluid properties are almost same, except there are different lengths and diameters.

Table 2-2 Comparison of Two model results

DCM Diameter(mm)	6	Phase angle (°)	**-62.4**
DCM Length(m)	2.5	Acoustic Power (W)	**112.1**
Multi-DCM D1(mm)	6	Phase angle (°)	**-62.4**
Multi-DCM D2(mm)	6		
Multi-DCM L1(m)	1.25	Acoustic Power (W)	**112.1**
Multi-DCM L2(m)	1.25		

In order to confirm the accuracy of the Multi-Section Distributed Component Model, the calculation results are compared with the single-section distributed component model. Here, the diameters D1 and D2 are both 6 mm, and the lengths L1 and L2 are both 1.25 m, providing a total length of 2.5m; the same as the input parameters of the single-section Distributed Component Model. Table 2-2 shows the calculation results: From Table 2-2, we can see the two models have almost the same results with the same boundary conditions. Thus, we can change the diameters and lengths of the Multi-section Distributed Component model in different experimental situations to obtain the required phase angle and acoustic power.

2.3 Figure of Merit for the adjustable inertance tube

In commercial applications, it may be advantageous to vary the phase angle while keeping the acoustic power as stable as possible. It is therefore helpful to know whether changing the diameter or adjusting the length is more effective for producing a significant

phase shift and an insignificant acoustic power change. A figure of merit for adjustable inertance tubes is proposed in order to compare such effectiveness for various inertance tubes arrangements.

$$FOM_D = \frac{\left(\frac{\partial \theta}{\partial D}\right)_L / \left(\frac{\theta_{original}}{D_{original}}\right)}{\left(\frac{\partial W}{\partial D}\right)_L / \left(\frac{W_{original}}{D_{original}}\right)} \tag{2-1}$$

$$FOM_L = \frac{\left(\frac{\partial \theta}{\partial L}\right)_D / \left(\frac{\theta_{original}}{L_{original}}\right)}{\left(\frac{\partial W}{\partial L}\right)_D / \left(\frac{W_{original}}{L_{original}}\right)} \tag{2-2}$$

The above equations define two figures of merit, FOM_D and FOM_L. FOM_D shows the ratio of the sensitivity of a phase shift to a change in diameter to the sensitivity of the acoustic power shift to the same change of diameter while at constant length. FOM_L provides the ratio of the sensitivity of a phase shift to a change of length to the sensitivity of acoustic power shift to the same change the length while at a constant diameter. The differential form of these equations enables a description of their measure for localized regions of phase and acoustic power. For example, the figure of merit for adjustable inertance tubes in the specific region of -50˚ is shown in FIGURE 2-4. As the acoustic power increases from 50 W to 300 W, FOM_D decreases while FOM_L increases. In this case, if the acoustic power is smaller than 104 W, FOM_D is larger than FOM_L indicating that in this acoustic power region (50 W to 104 W), changing the diameter is more effective than adjusting length for a sensitive phase angle shift and an insensitive acoustic power variation. If the acoustic power is larger than 104 W, FOM_L is larger than FOM_D.

Other phase angles will result in different ranges where FOM_L and FOM_D are larger and therefore indicate which type of adjustable inertance tube would be better suited to provide a significant phase shift with minimal acoustic power change. Figure 2-5 displays the same analysis for the specific region of a -60˚ phase angle.

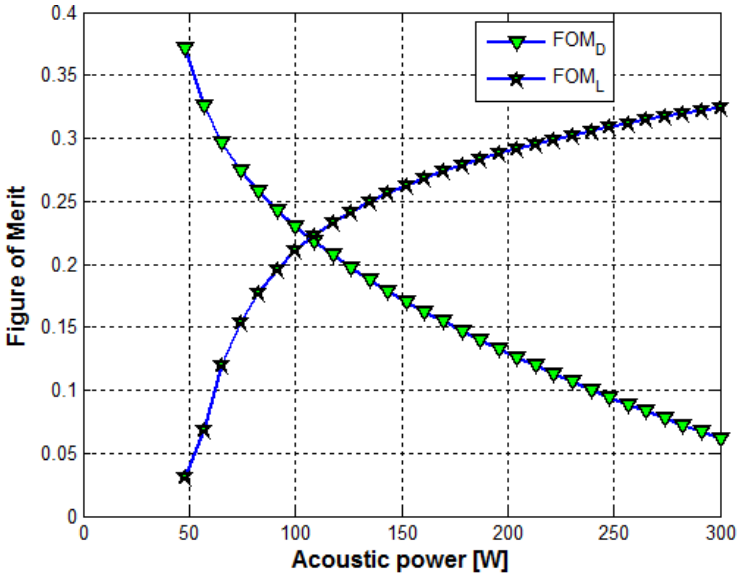

FIGURE 2-4 FOM_D and FOM_L vary with acoustic powers at -50°.

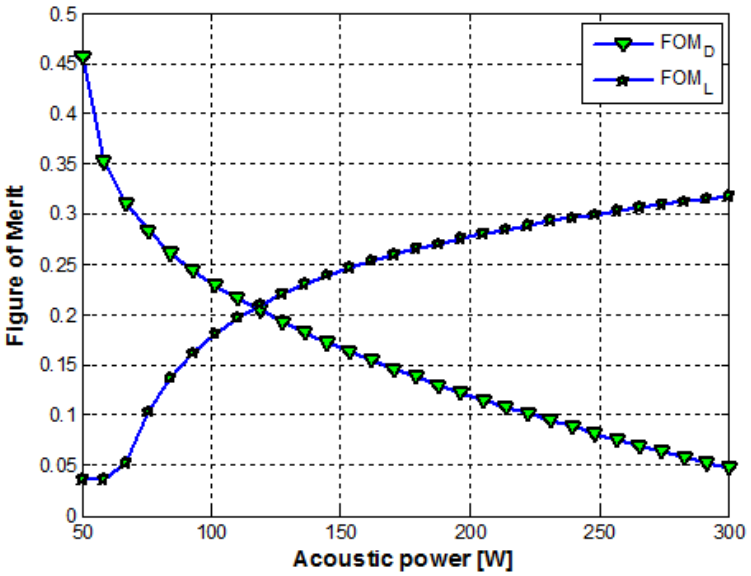

FIGURE 2-5 FOM_D and FOM_L vary with acoustic powers at -60°.

2.4 Design of a linear adjustable inertance tube (IT#1)

2.4.1 Configurations of the linear adjustable inertance tube[46]

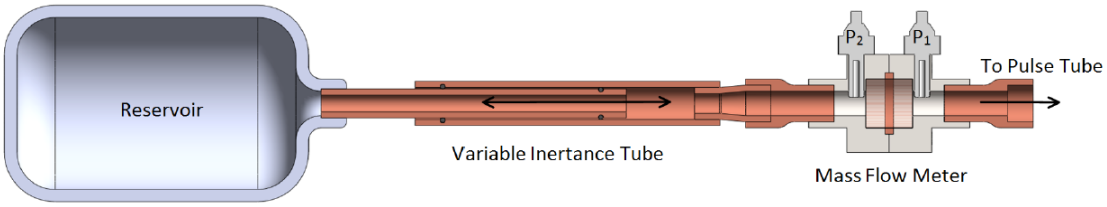

FIGURE 2-6 Configurations of linear adjustable inertance tube (IT#1)

The linear adjustable length inertance tube component uses a sliding tube-in-tube design as depicted in FIGURE . There are three pieces in this configuration including a reservoir, variable length inertance tube, and a mass flow meter. One of the smaller tubes connects to the reservoir, while the larger tube connects to the mass flow meter. Modeling results reveal that the phase angle produced by the inertance tube can be pretty

sensitive to the length of the inertance tube in a certain range of tube lengths, and fairly insensitive to the same parameter in other ranges of the length.

2.4.2 Experimental set-up equipment

There are several unique components used to characterize the continuously variable phase shift mechanism. These working pieces are an adjustable inertance tube, a mass flow meter, and a LabVIEW based lock-in amplifier. These components are mounted on a two-stage pulse tube refrigerator to directly observe the influence of the variable inertance tube at the warm end of each pulse tube. The pressure transducer in the experiment of the variable inertance tube has been set up to capture the dynamic pressure at the inlet of the inertance tube.

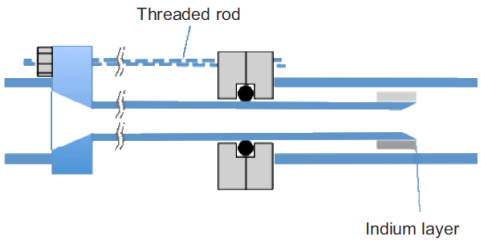

FIGURE 2-7 Schematic of adjustable length inertance tube

FIGURE illustrates the schematic of the telescoping embodiment of the continuously variable inertance tube. From this figure one can see that in order to minimize the flow of gas into and out of the annular gap between the two tubes, a 0.3mm thick times 10mm long layer of indium is applied to the outer diameter at one end of the inner tube. The leak-free seal between the pressurized tubes and the surrounding

environment is realized by trapping a single Viton O-ring between two flanges, with a groove designed to squeeze the O-ring down around the inner tube. A threaded rod is used to hold the two tubes together under pressure, and also allows for 24 cm of continuous length adjustment, giving the inertance tube a range of total lengths from 1.27m to 1.54m.

TABLE 2-3 Geometric parameters of the adjustable length inertance tube

	Outer Diameter (m)	Inner Diameter (m)	Length (m)
Outer tube 1	9.53e-3	7.04e-3	0.356
Inner Tube	6.53e-3	4.83e-3	0.327
Outer tube 2	9.53e-3	7.04e-3	0.886

TABLE 2-3 shows the detailed dimensions of the variable length inertance tube. The adjustable length inertance tube is a tube-in-tube device. The diameter of the outer and inner tubes is 9.53 mm and 6.53 mm respectively. During the operation of the pulse tube refrigerator, we can turn the bolts and nuts of the adjustable inertance tube to change the length in the real time. Due to the length limitation, the designed adjustable inertance tube can only vary its length between 1.27 m and 1.54 m. The difference of the longest length and shortest length is only 15% of the total length, which provides only a moderate phase shift.

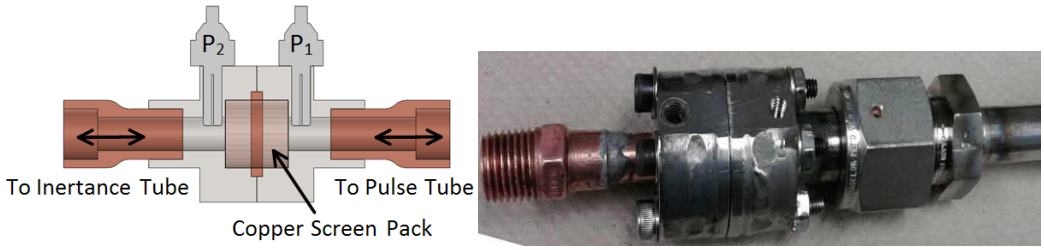

FIGURE 2-8 Mass flow meter to measure the oscillation flow

The mass flow device is shown in FIGURE . It was initially constructed by stacking 110 copper screens into the space between two conflate flanges as depicted FIGURE . The pressure drop through the screen pack is dominated by the flow resistance and measured using two separate Endevco pressure transducers mounted at each end of the screen pack. Because of the large number of copper screens between the two flanges, the pressure drop in the mass flow meter resulted in an excessive loss of acoustic power. Subsequently, a 6-piece copper screen pack (80 mesh) has been mounted in the mass flow meter in order to measure the pressure drop between the two pressure transducers. The mass flow meter has been calibrated so that the amplitude of the pressure drop across the screen pack can be directly related to a mass flow rate.

In order to measure the phase difference between the mass flow rate and pressure wave, a lock-in amplifier was developed entirely within LabVIEW^{TM} software based on the LabVIEW^{TM} Lock-in Start-up kit, which is shown in FIGURE . The kit was modified to use the pressure P1 as the reference and the difference in pressure P1-P2 across the screen pack as the signal. All data is stored in an external file for subsequent analysis. A 14 bit NI USB-6009 low cost DAQ was used for the data acquisition. There are four

analog inputs in this NI USB multi-functional device, allowing a quick software switch between the mass flow meters during operation.

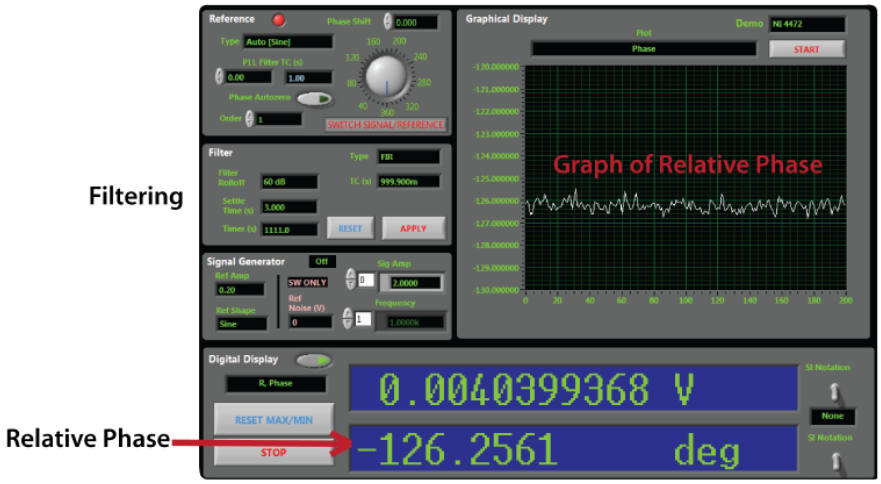

FIGURE 2-9 LabVIEW Lock-in Amplifier

The mass flow meter measures the pressure wave both before and after the screen pack. The pressure waves at the mass flow meter are shown in FIGURE . The average pressure in this example is 2.07 MPa, and the pressure amplitude at the warm end of the pulse tube Pd is about 0.205 MPa. Due to the nonzero flow impedance across the screen pack, the pressure amplitude at the inlet of the inertance tube is about 0.155 MPa. With this pressure difference, the Lock-in amplifier can easily obtain the phase shift between the mass flow and pressure wave at the warm end of the pulse tube. In the case shown in FIGURE , the operating frequency is 50 Hz, the length of the variable inertance tube is 1.409 m, and a -28.93 º phase shift is measured between the mass flow and pressure oscillations.

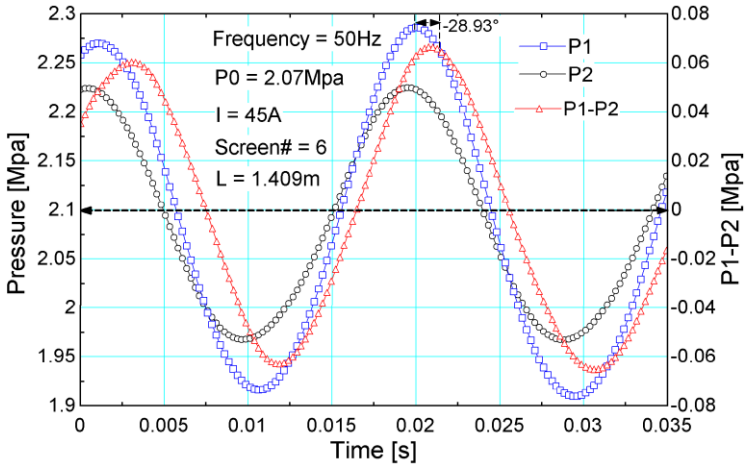

FIGURE 2-10 Phase shift between mass flow and pressure

2.5 Comparison of the model and experimental results

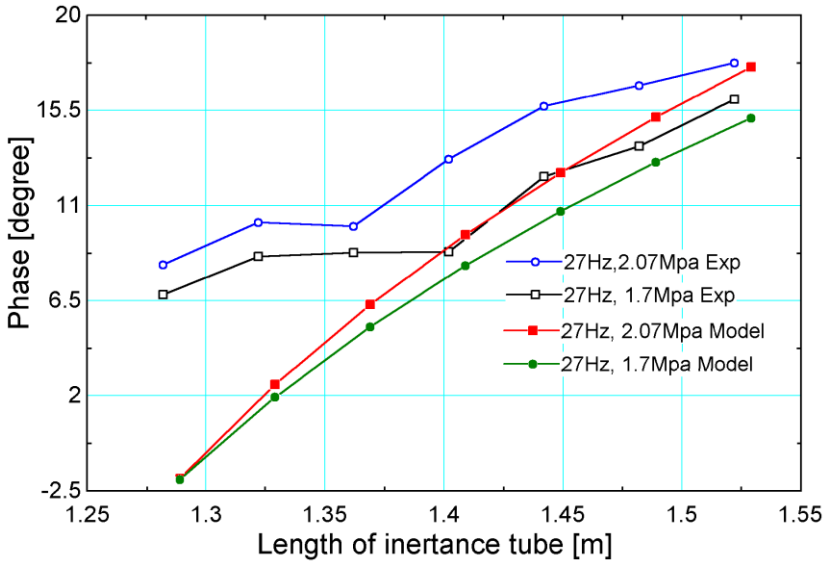

FIGURE 2-11 Phase shift change with length at 27 Hz

The influence of the inertance tube length on the phase shift between the mass flow and pressure oscillations at 27 Hz is shown in FIGURE for two different average

pressures, 2.07 MPa and 1.7 MPa. The phase angle changes from 7.5 º to 18.5 º as the length varies from 1.289 m to 1.529 m, a 15.6% change in length. As a comparison, the phase shift from the distributed component model is also shown. A small, but noticeable discrepancy exists at the shorter length, but the curves converge as the length increases. Also, the change of phase over this length change is about 12 ºfrom the model compared to 11 ºfrom the experiment.

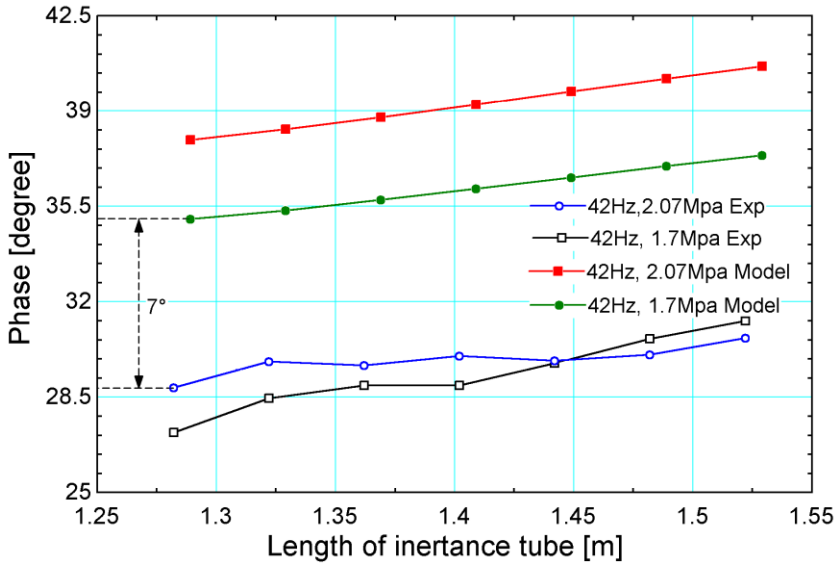

FIGURE 2-12 Phase shift change with length at 42 Hz

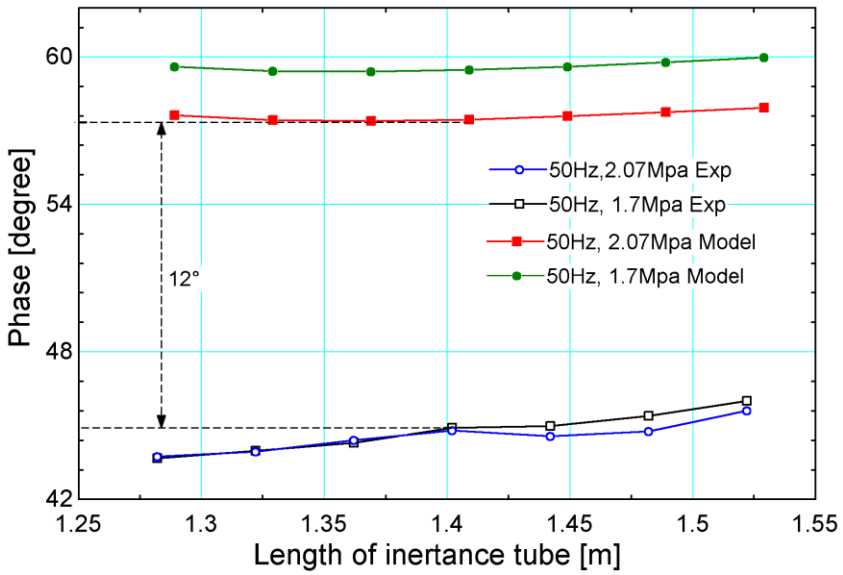

FIGURE 2-13 Phase shift change with length at 50 Hz

Additional experiments have been carried out by varying the frequency from 27 Hz to 50 Hz. The phase shift as a function of inertance tube length at 42 Hz and 50 Hz are shown in FIGURE and FIGURE , respectively. The phase angle shifts from 26.5 ºto 31.5 º as the length changes from 1.289 m to 1.529 m at 42 Hz. The same trend is predicted by the model. From FIGURE , there is only a 3.5 ºphase shift as the length of the inertance tube varies from 1.289 m to 1.529 m at 50 Hz. Although there are some discrepancies between the experimental data and model calculation, both display the same trends in FIGURE and FIGURE . Various mechanisms such as tube roughness, heat transfer and exit/entrance effects are being explored to resolve the discrepancy. However, both the experiment and model reflect the same change of phase caused by the change in inertance tube length. From the data presented in FIGURE , FIGURE , and FIGURE , one can conclude that the phase shift is more sensitive to changes in the inertance tube length at lower frequencies than at higher frequencies.

Phase angle changes as a function of frequency from 52 Hz to 27 Hz at average pressures of 2.07 MPa and 1.7 MPa are displayed in Figure 2-14 and Figure 2-15. The measured phase generally decreases from around -10 º to around -45 º as the operating frequency increases from 27 Hz to 52 Hz. Both the experimental data and model data reflect the same trend. Although the discrepancy between the model and measurements are minor at the lower frequencies, these increase as the frequency increases. Figure 2-14 and Figure 2-15 also reflect a sensitive dependence of the phase shift on length at lower frequencies, such as 27 Hz, but a significantly reduced sensitivity at higher frequencies. A larger change in length is required in order to obtain a large phase shift if the cryocooler runs at a higher frequency.

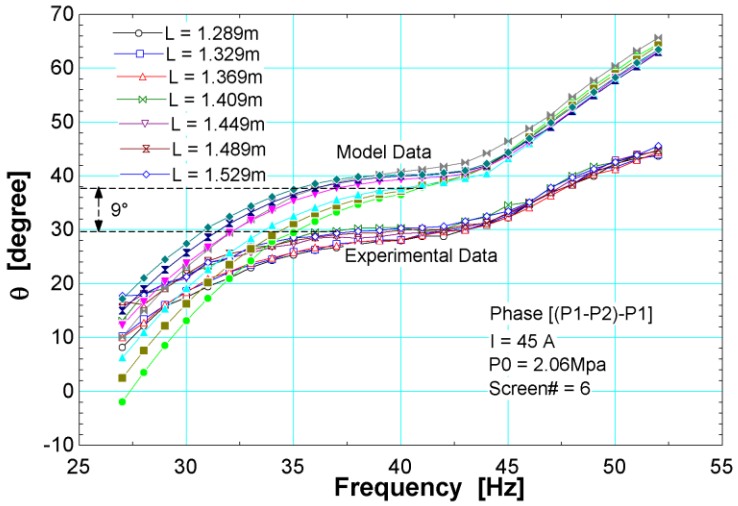

FIGURE 2-14 Phase shift changes with frequency at 2.06Mpa

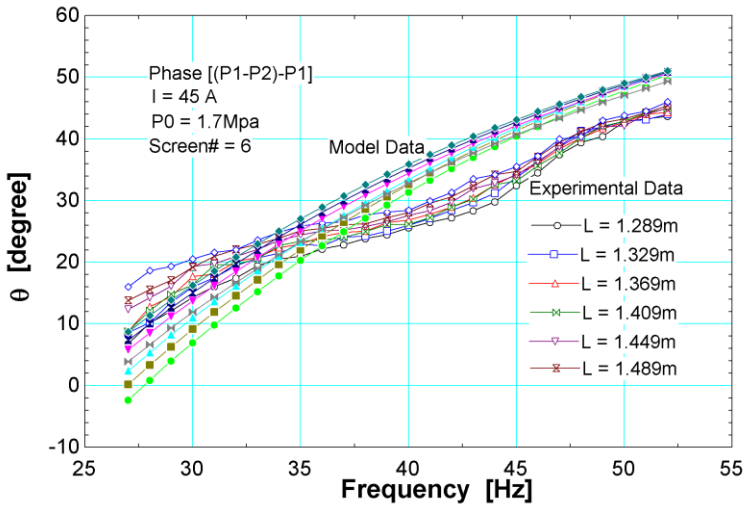

FIGURE 2-15 Phase shift changes with frequency at 1.7Mpa

Adjusting the length of the inertance tube and the operating frequency not only varies the phase angle between the mass flow and pressure oscillations, but also the mass flow amplitude and acoustic power at the warm end of pulse tube. FIGURE 2-16 displays the variation of mass flow amplitude with length at different frequencies. The trend of the measurements and model again are very similar. At 27 Hz, the model fits the experiment very well. However, at the higher frequencies, such as 42 Hz and 50 Hz, small discrepancies may be observed. The peak in the mass flow amplitude around 42 Hz is in keeping with expectations presented by Lou *et al.*[6]. From the mass flow, pressure amplitude and phase angle between these two parameters, the acoustic power is easily obtained via the simple acoustic power expression.

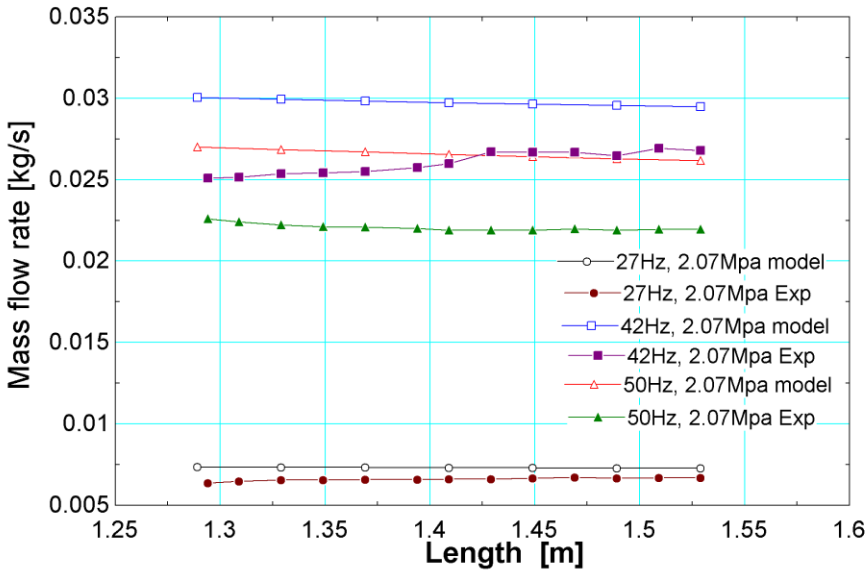

FIGURE 2-16 Mass flow change with length

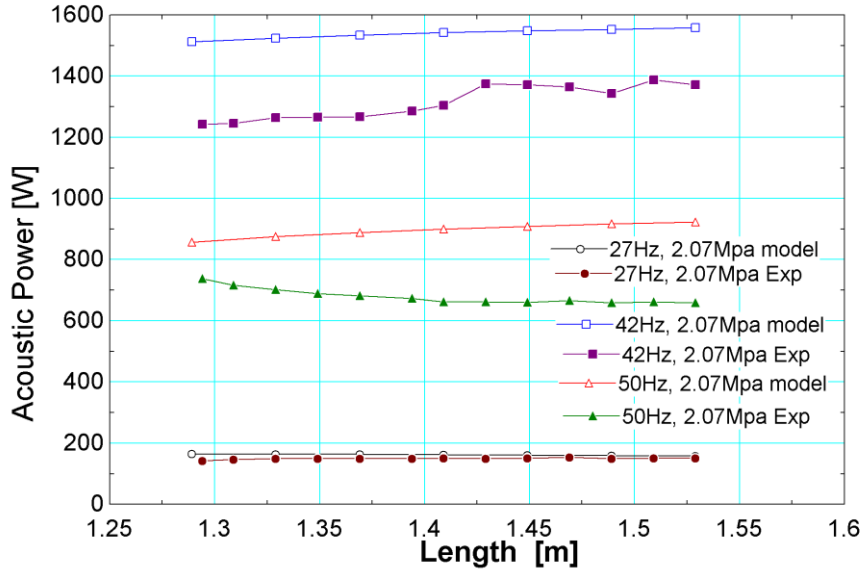

FIGURE 2-17 Acoustic power change with length

The change in acoustic power with the length is shown in FIGURE 2-17. The acoustic power increases slightly from 141.6W to 150W as the length ranges from 1.289m to 1.529m at 27 Hz. These small changes are a result of the configuration limitations in our experiment. The largest percentage change to the inertance tube length in our present configuration is limited to only 16% of total length.

FIGURE 2-18 and FIGURE 2-19 display the variations of mass flow amplitude and acoustic power as a function of the operating frequency and inertance tube length. For our inertance tube, a maximum in both the mass flow amplitude and acoustic power is observed around 42Hz. Notice that a small length change can generate a relatively large variation in the mass flow amplitude and acoustic power at this frequency. Both the measurements and the model display the same trends as a function of frequency and length.

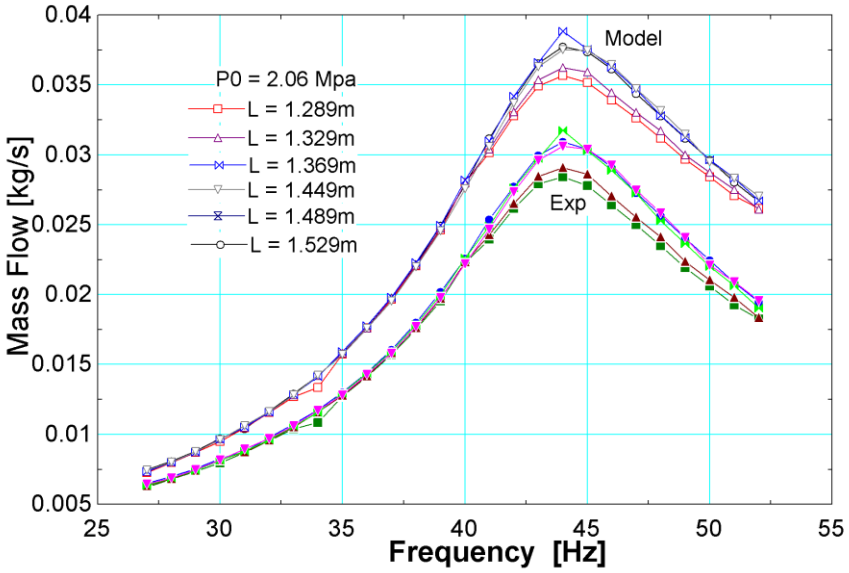

FIGURE 2-18 Mass flow change with frequency

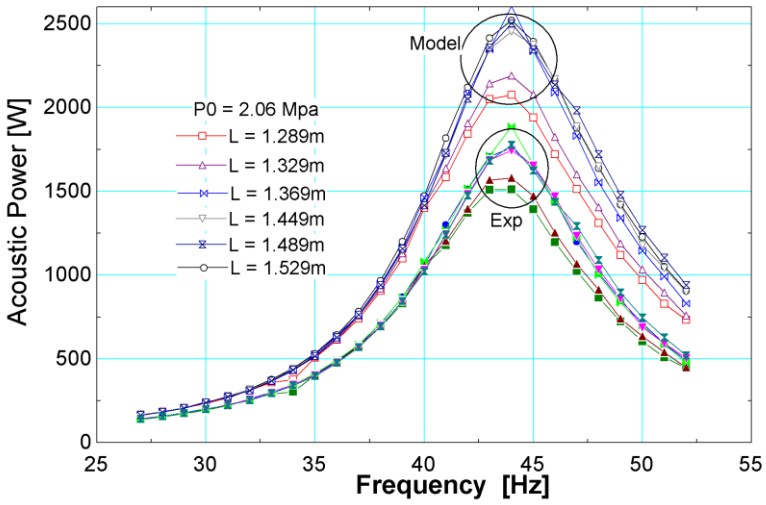

FIGURE 2-19 Acoustic power change with frequency

In an effort to confirm the predictions of the model with other published data, we display in FIGURE 2-20 the data and modeling results for the single case of L= 1.289 m, D=4.83 mm, and P_0 = 2.06 MPa, along with that reported by Lewis et al.[8] for L = 2.36 m, D= 5.74 mm and P_0 = 2.5 MPa. Note that the distributed component model accurately predicts both sets of data. Furthermore, the peaking behavior evident in both sets of data correlates well with the predictions of Luo et al. In figure 3 of Luo et al. a maximum in the acoustic power is found near the dimensionless lengths of 0.35 and 0.8 (allowing for large, but finite sized reservoirs), with the larger peak at the dimensionless length of 0.35. At 42 Hz our dimensionless length is 0.33 while at 57 Hz, the dimensionless length associated with the data presented by Lewis et al. is 0.82.

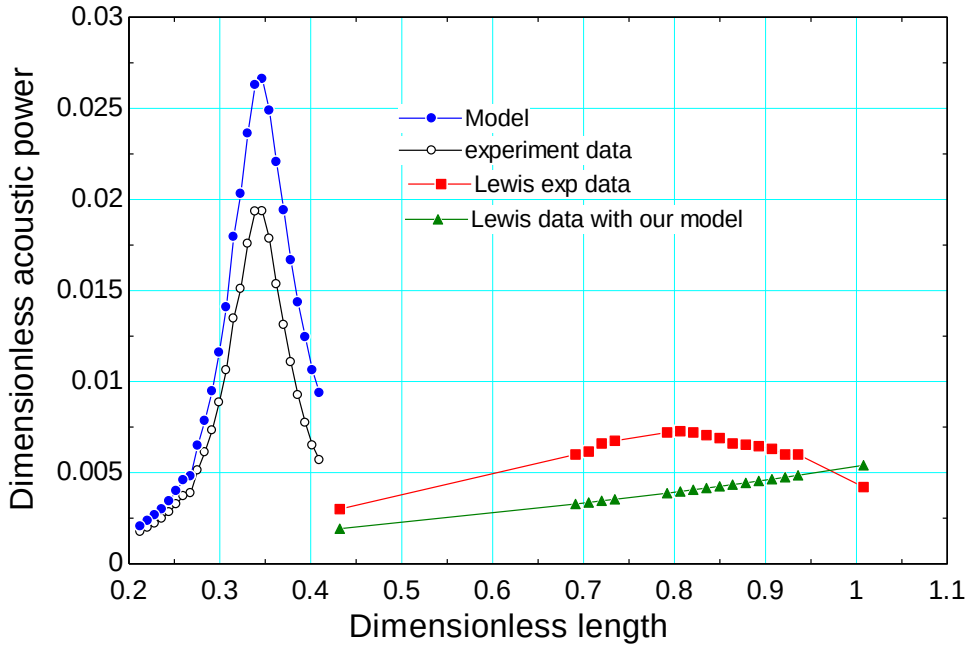

FIGURE 2-20 Comparison of the other paper's data

2.6 Summary

The measured trends of a linear adjustable inertance tube, in terms of phase shift, mass flow amplitude, and acoustic power resultant from variations in inertance tube length and operating frequency match the predictions of the distributed component model. The mass flow and pressure oscillations, as well as the phase difference between them at the inlet of the inertance tube are measured from the experiment, and these also match the model predictions. At lower frequencies, such as 27 Hz, the phase shift is sensitive to the length changes of the inertance tubes. A maximum is observed in the mass flow amplitude and acoustic power around 42 Hz, also in agreement with the model.

The largest percentage change to the inertance tube length in this linear configuration is limited to only 16% of total length. Therefore, some efforts must be directed at modifying and increasing the possible change of length, and adjusting the diameter of the inertance tube to obtain a large phase shift.

3 Design of Conical and Threaded Adjustable Inertance Tube

Since a phase shift of only 11 degrees results from changing the length of the inertance tube via the linear adjustable inertance tube (IT#1), conical (adjustable diameter only, which is IT#2) and threaded adjustable inertance tubes (IT#3) are proposed in order to obtain a large phase angle shift. The conical adjustable inertance tube consists of two conical screws together; the hydraulic diameter varies as the inner conical screw moves up and down. The threaded adjustable inertance tube allows both the diameter and length to change while the pulse tube is operating. The details of the configurations will be shown in the following part of this section.

3.1 Conical adjustable inertance tube [47]

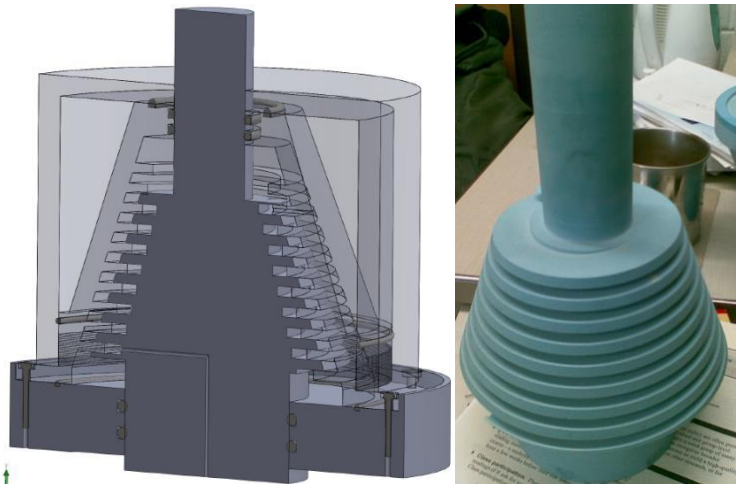

FIGURE 3-1 Configurations of conical screw inertance tube

The design of the conical inertance tube is shown in FIGURE 3-1. Here, two concentric conical screws are attached together, and the gap along their teeth generates the channel of the inertance tube. The reservoir is the gap between the outer screw and the cylinder. The channel at the bottom of the inner screw connects the inertance tube to the pulse tube. The diameter of the inertance tube can be continuously adjusted by turning the inner screw up and down inside the outer screw during the operation of pulse tube cryocooler. In this configuration, the effective diameter can vary from 8 mm to 14 mm, while spring loaded stops appropriately mounted near the ends of the inner and outer screws enable the total length to be changed at the same time from 1.87 m to 2.49 m. O-rings are utilized to seal the tube/reservoir so that they can be pressurized above ambient conditions. An imperfect but sufficient seal between the threads enables the inertance tube to sustain the pressure oscillation above and below the average pressure that exists in the reservoir. TABLE 3-1 shows some basic design parameters of this specific conical adjustable inertance tube.

TABLE 3-1 Basic parameters of the conical inertance tube

Total turns	8	Variable Turns	2
L_{min} (m)	1.87	L_{max}(m)	2.49
D_{min}(m)	8e-3	D_{max}(m)	14e-3

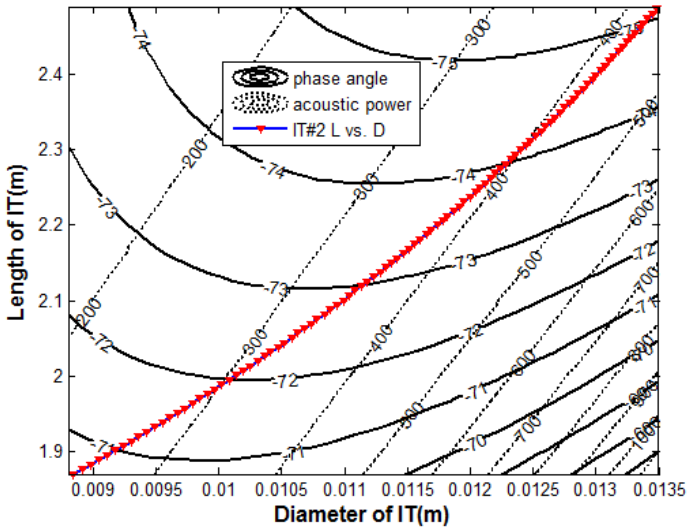

FIGURE 3-2 Contour plot of phase and acoustic power vs. length and diameter for conical adjustable inertance tube

If the inner screw in FIGURE 3-1 is moved from its uppermost location to its lowest location, the hydraulic diameter will increase from 8 mm to 14 mm, while the length increases from 1.87 m to 2.49 m. The associated changes of length and diameter are shown in FIGURE 3-2 as the dark thick line. The contour lines included in FIGURE 3-2 describe the corresponding phase angle and acoustic power shift as a function of the length and diameter of the conical adjustable inertance tube. From the thick curve in FIGURE 3-2, one may see that the acoustic power varies from 250 W to 400 W; and the phase angle changes from -71° to -75° as the inner screw travels from its highest to lowest position. The dark thick line in the middle of the plot nearly follows a line of constant acoustic power, suggesting the possibility for producing a phase angle shift while maintain a constant acoustic power.

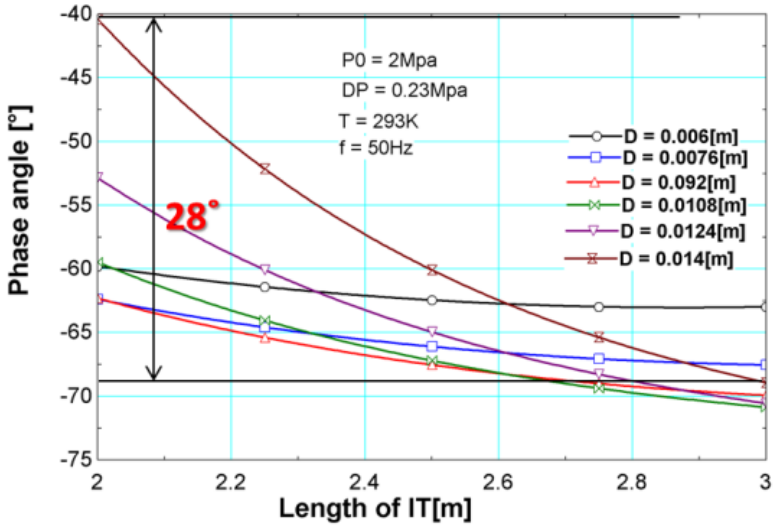

FIGURE 3-3 Phase shift with length for linear adjustable inertance tube

FIGURE 3-3 shows a specific example of the conical inertance tube. A number of interesting features may be noted by comparing the performance of the linear adjustable inertance tube and conical adjustable inertance tube over a certain range of diameters and lengths. Consider for example, a length change between 2 m and 3 m, and a diameter variation between 6 mm to 14 mm. The variation of phase angle with length for IT#1 is plotted in FIGURE 3-3 for the indicated operating conditions. The length of the inertance tube is changed from 2 m to 3 m, resulting in a change of phase shift from -40° to -68°. In the plot, the diameter also varies from 6 mm to 14 mm. The largest phase shift is achieved when the diameter of the inertance tube is about 14 mm. In a real application, it would be awkward to change the length of the inertance tube shown in FIGURE 3-3 from 2 m to 3 m, since the space in the lab or other machines is limited. Notice that the phase shift is more sensitive to a change of length at large diameters, such as 14 mm, than it is at smaller diameters, such as 6 mm. Changing the length from 2 m to 3 m results in

nearly a 28° phase shift with a 14 mm diameter, and only a 2 ° phase shift with the 6 mm diameter. The phase shift is sensitive to combinations of the diameter and length under certain working conditions, indicating that some combination of diameter and length would provide an optimum sensitivity for a conical inertance tube.

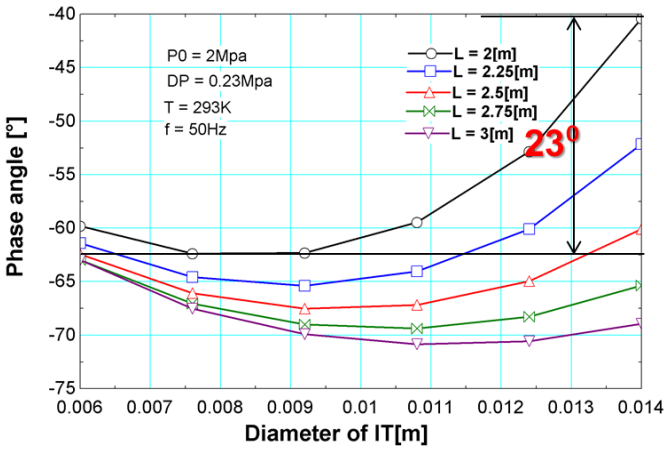

FIGURE 3-4 Phase change with Diameter (IT#2).

FIGURE displays the dependence of phase angle on the diameter of conical adjustable inertance tube for various lengths. The operating conditions are the same as those in FIGURE 3-3. The diameter of the conical adjustable inertance tube changes from 6 mm to 14 mm, producing a change in the phase angle from -63° to -40° with a 2 m length. Notice the convenience of adjusting the diameter from 6 mm to 14 mm simply by turning the inner screw from the topmost to the bottommost position. A phase shift of almost 23° is obtained from this conical adjustable diameter inertance tube. Although fabricating the conical inertance tubes presents a more complex process than the adjustable length design, the diameter is easily adjusted, allowing a convenient method

for producing a continuously adjustable and significant phase shift during the operation of a pulse tube cryocooler.

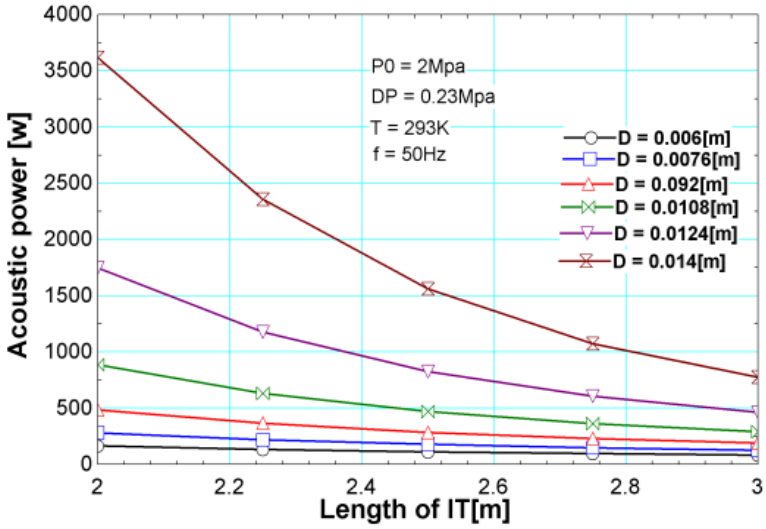

FIGURE 3-5 Acoustic power vs. Length (IT#1).

The other important parameter that must be considered with respect to an adjustable inertance tube is the acoustic power. In order to control the cooling capacity at the cold end of pulse tube cryocooler by adjusting the phase angle at the inlet of the inertance tube, it is desirable to maintain a constant acoustic power to optimize the overall system efficiency. However, as evidenced in FIGURE 3-5 and FIGURE 3-6, the acoustic power does not remain constant when a large shift is produced by changing the diameter or length. FIGURE 3-5 shows an acoustic power change of almost 3000 W when the length of IT#1 shifts from 2 m to 3 m at the 14 mm diameter. With the small diameters, the change in acoustic power is small, but the phase shift is also insignificant. Similar behavior occurs with the conical geometry, IT#2. FIGURE 3-6 displays a change

of almost 5000 W in acoustic power when the diameter of conical adjustable inertance tube changes from 6 mm to 14 mm with a length of 2 m. The change of acoustic power is smaller for the 3 m case, but still, the associated phase change is also small. These observations lead to a third design, which is threaded adjustable inertance tube (IT#3).

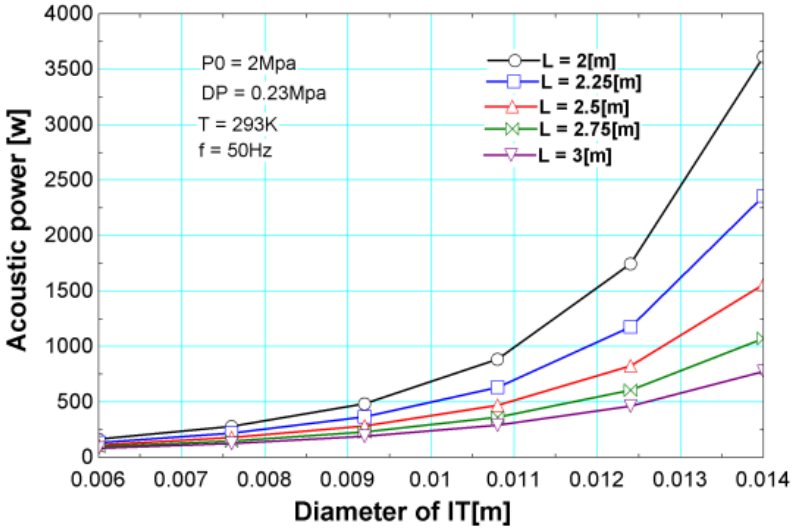

FIGURE 3-6 Acoustic power vs. Diameter (IT#2).

3.2 Design of the threaded adjustable inertance tube (IT#3)

As shown above the phase angle shift for the linear adjustable inertance tube (IT#1) is relatively small as a result of changing the length of the inertance tube in the real time. Although the conical adjustable diameter inertance tube can provide a significant phase shift by changing the diameter, the acoustic power consumption also varies a lot when only changing the diameter of the inertance tube. Therefore, the threaded adjustable inertance tube (IT#3) is proposed to solve these two problems. IT#3

is designed to enable adjustment of the diameter and length of the inertance tube while the pulse tube cryocooler is operating.

Continuing the idea of an adjustable diameter inertance tube via concentric screws, a third design has been developed that also enables a change of both the length and diameter of the inertance tube at the same time. The configuration of the threaded inertance tube is shown in FIGURE 3-7. Here, the inertance tube is created by the helical gap between the root of the inner screw and the teeth of the outer screw, and its effective diameter varies by turning the inner screw from right to left thereby adjusting the percentages of a series connected large-and small-diameter inertance tube. A spring loaded stop at the left end of the inner screw and a corresponding spring loaded stop at the right end of the outer screw define the length of the inertance tube. Thus, as the inner screw and the left end stop are moved toward the right, the overall length decreases at the same time that the effective diameter decreases. The empty chamber on the far right serves as the reservoir whose volume changes as the position of the inner screw is adjusted. The smallest extent of the reservoir volume is chosen so that the relative changes do not alter its influence on the system performance.

For the threaded inertance tube, the length and diameter both increase when the inner screw moves from right to the left. The effective diameter for each inertance tube is calculated according to the definition of effective diameter:

$$D_{eff} = \frac{2WL}{W + L} \tag{3-1}$$

Here W is the radial width of the gap between the two screws, and L is the axial extent of the channel.

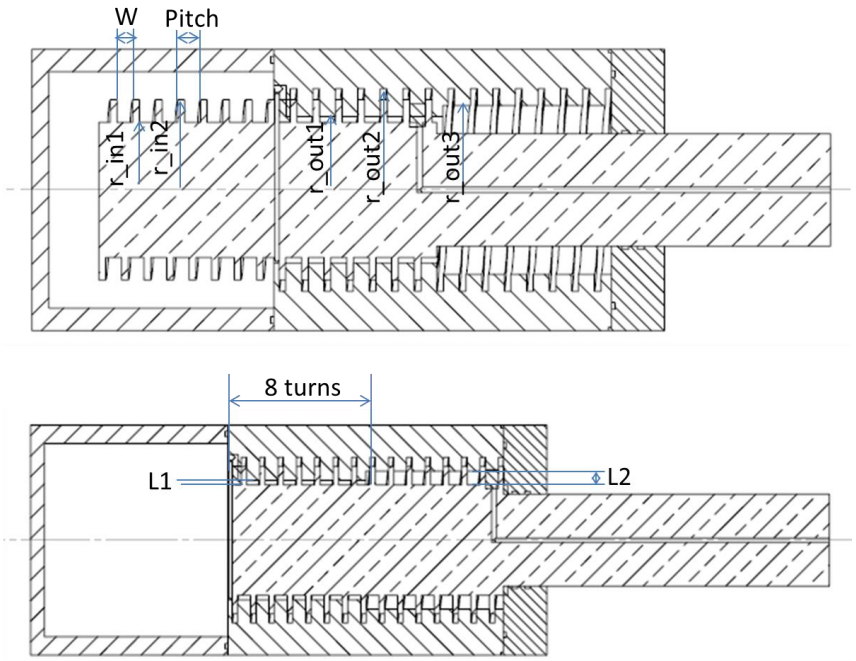

FIGURE 3-7 Configuration of threaded adjustable inertance tube (IT#3, the upper picture is at the position where it has small diameter and short length; the bottom one is at the position where it has the largest diameter and longest length)

The basic dimensions of the threaded cylindrical adjustable inertance tube are listed in TABLE 3-2. The parameters in the table are corresponding to the dimensions labeled in FIGURE 3-7.

TABLE 3-2 Dimensions of cylindrical adjustable inertance tube.

r_in1(mm)	60	r_in2(mm)	80	r_out1(mm)	65
r_out2(mm)	90	r_out3(mm)	75	W(mm)	14
Pitch(mm)	20	L1 (mm)	5	L2 (mm)	15

FIGURE 3-8 displays the change of length and effective diameter vs. the number of turns comprising the inertance tube as the inner screw goes from right to left. The total length goes from 3.8 m to 7.5 m. The effective diameter changes from 7 mm to 11 mm. The range of this diameter and length agree well with the future experiment needs.

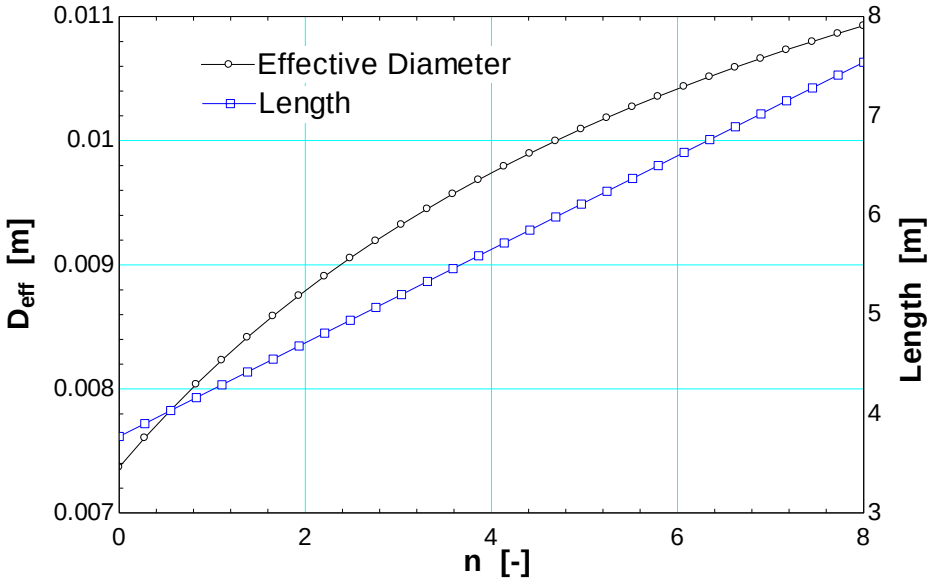

FIGURE 3-8 Length and diameter vs. turns (IT#3).

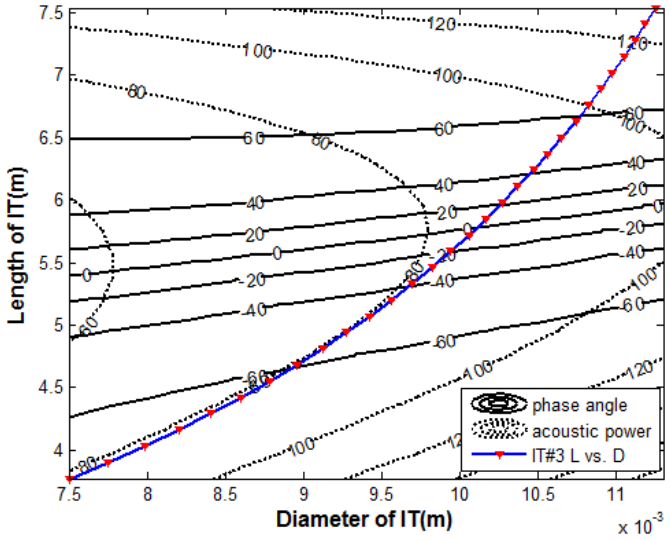

FIGURE 3-9 Contour plots of phase angle and acoustic power changes with D and L (IT#3).

FIGURE 3-9 shows the contour plots for the phase angle and acoustic power associated with various inertance tube diameters and lengths as calculated by the Distributed Component Model using the charge pressure, frequency and pressure ratio as the input parameters. FIGURE 3-9 describes the contour of constant phase angle shifts from -60° to 60° (the nearly horizontal lines sloping slightly upward from left to right in the middle of the graph) and contours of constant acoustic power ranging from 60W to 120 W. The dark thick line in the middle of the plot displays the same values of length vs. diameter from FIGURE 3-8. Notice that the curve provides an almost constant acoustic power of 80 W as the diameter increases from 7.5 mm to 9.5 mm when the phase shifts from -60° to -20°. Therefore, the threaded adjustable inertance tube can provide a large phase shift while maintaining a constant acoustic power.

From the theoretical calculations, the threaded adjustable inertance tube has the potential to maintain the acoustic power constant while generating a large phase change. Therefore, we have carried out a detailed design of the threaded adjustable inertance tube. The configuration of the threaded adjustable inertance tube is shown in FIGURE 3-100. This configuration also includes the reservoir and fin heat exchanger around the reservoir.

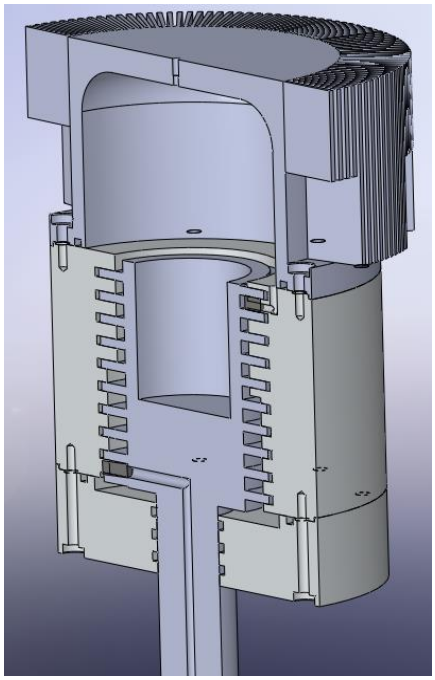

FIGURE 3-10 Configuration of threaded adjustable inertance tube

The threaded adjustable inertance tube consists of an inner screw, outer screw, reservoir, and bottom flange, which is shown in FIGURE 3-100. Several O-rings are used to seal the 2.0 MPa average pressure inside the inertance tube. There are fins around the reservoir to cool down the temperature of the reservoir during the operation of the pulse tube. An anodized coating is used on the teeth of the inner and outer screws to decrease

the friction between the two screws. Bolts strength calculations have been applied to determine the type and number of the bolts used on the device. There is a long channel from the inlet of the inner screw to the adjustable inertance tube inlet. The diameter is sufficiently large to ensure that the pressure drop along this channel is significantly smaller than the pressure amplitude of the oscillations. Details of these various design features are discussed later.

3.2.1 Fin heat exchanger design around the reservoir

During the pulse tube refrigerator operation, there may be a significant amount of acoustic power consumption in the concentric screw configuration. The fin heat exchanger is added on the outside of the reservoir to maintain the temperature below 50 C. FIGURE 3-11 shows the configuration of the fin heat exchanger around the reservoir. The reservoir cover is attached on the outer screw by 8 bolts. The bolts strength verification will also be provided in the following discussion.

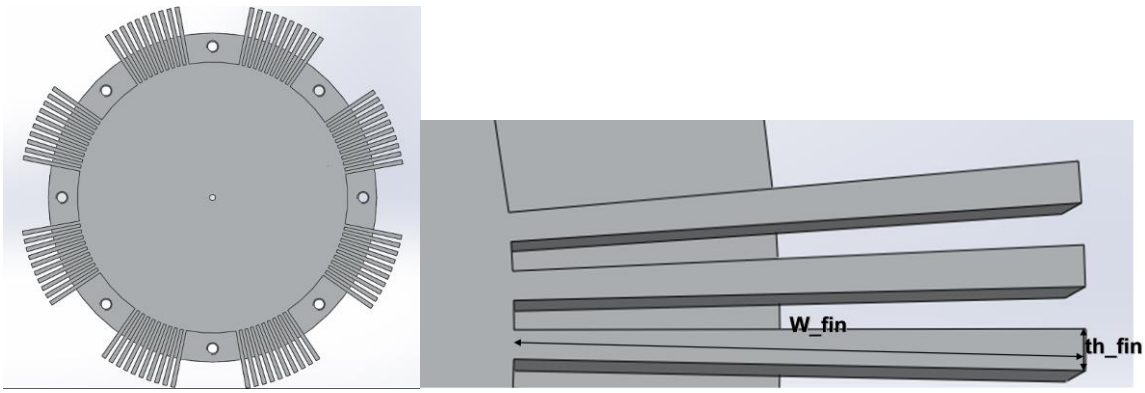

FIGURE 3-11 Fins heat exchanger around the reservoir.

TABLE 3-3 displays the basic parameters of the fin heat exchanger. The device is constructed out of aluminum 6061. The fin thickness is 2 mm, with 38 mm length in

radial direction and 102 mm width in axial direction. An acoustic power dissipation of 300 W is estimated based on the power generated by the linear compressor in the experiment. The surface temperature of the reservoir is set to be no higher than 50 C. All the input parameters are entered into EES to find the best fin thickness and number of fins.

TABLE 3-3 Basic fin design parameters.

T_air (K)	293	k_fin (W/m-K)	177
W_fin (m)	0.102	th_fin (m)	0.002
L_fin (m)	0.038	Dia_cylinder (m)	0.178
a_fin (m)	0.002	h_fin (W/m^2-K)	20
q_dot_fin (W)	300	N_fin	68

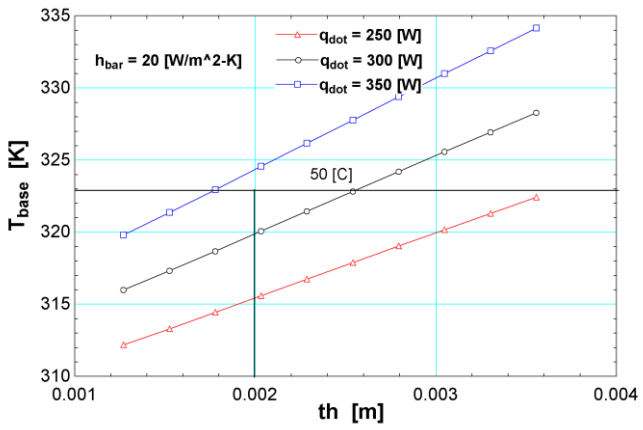

FIGURE 3-12 Temperature of the reservoir vs. thickness of the fins

From FIGURE 3-12, we can see that if the fin thickness is about 2 mm, the surface temperature will be less than 50 C when the acoustic power is no greater than 300 W. The total number of the fins around the reservoir is 68 in this design.

3.2.2 Torque calculations using the hard anodized coating

The inner screw and outer screw are all made from aluminum. The friction coefficient between two aluminum pieces is relatively high. Therefore, a hard anodized coating will be applied on both inner and outer threads. According to the "aluminumsurface.blogspot.com" website, we can expect a friction coefficient between the two hard anodized coating surfaces of about 0.04. The calculation results are shown in FIGURE 3-13. From this figure, the torque to turn the outer screw up and down is only 25 N-m, which is a small number. Thus, we can change the diameter and length of the threaded adjustable inertance tube relatively easily during real time operation of the PTC.

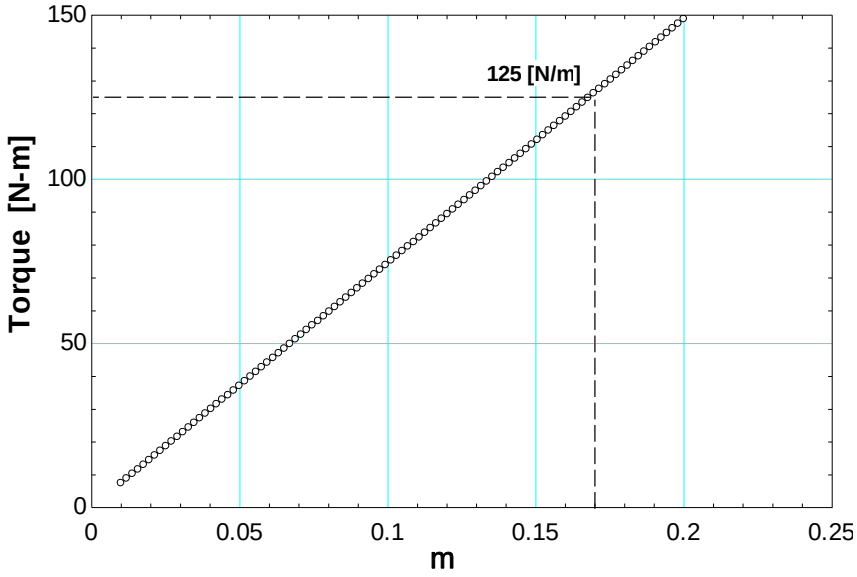

FIGURE 3-13 Screw torque vs. friction coefficient.

3.2.3 Bolt strength calculation

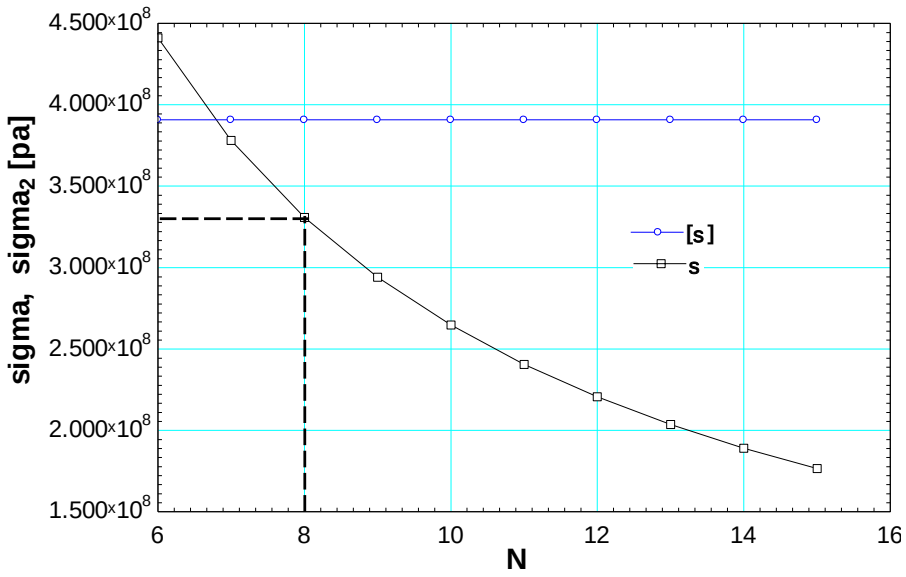

FIGURE 3-14 Tensile strength vs. number of bolts

FIGURE 3-14 shows the bolts tensile strength calculation. The critical tensile strength [σ] is 3.9e8 pa when using a 5/16" diameter bolt. 8 bolts are used to fix the reservoir and the outer screw together. The maximum tensile strength on each bolt is about 3.3e8 pa, which is smaller than the critical strength. Thus, it is safe to use 8 bolts while maintaining a pressure of 2.0 MPa inside the reservoir.

3.2.4 Pressure drop along the channel

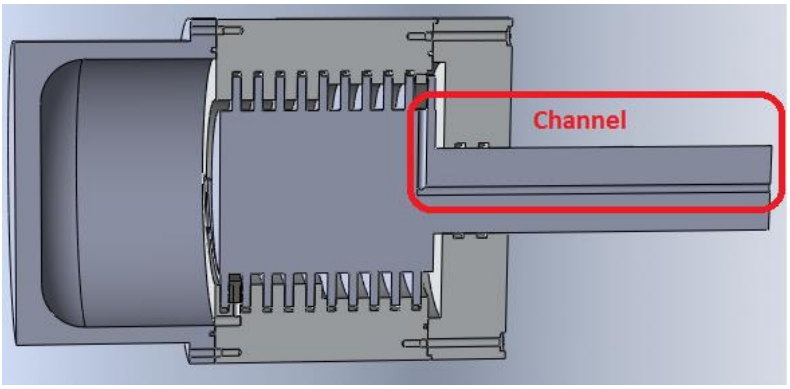

FIGURE 3-15 Channel from inner screw inlet to the adjustable inertance tube inlet

In the geometry of the threaded adjustable inertance tube, there is a long channel from the inner screw inlet to the adjustable inertance tube inlet, as shown in FIGURE 3-15. If the pressure drop along this channel is as large as the pressure amplitude in the inertance tube, the performance of the adjustable inertance tube will be completely degraded. The pressure drop along the channel is very sensitive to the diameter of the channel. The calculation of the pressure drop in this channel is shown in FIGURE 3-16.

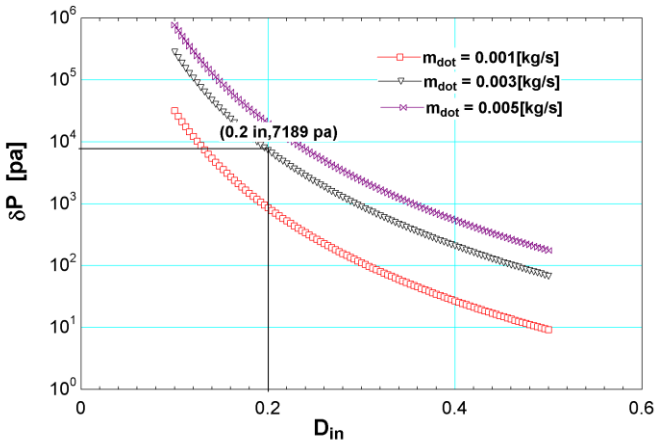

FIGURE 3-16 Pressure drop along the channel

The typical mass flow rate in the inertance tube is about 0.003 kg/s. The pressure drop along a 0.2” diameter channel is about 7189 Pa, which is smaller than the pressure amplitude of 228010 Pa in the variable inertance tube. Thus, 0.2” diameter channel is chosen to connect the pulse tube warm end and the inlet of the adjustable inertance tube.

3.3 Key parameters from the model prediction

In order to achieve a significant phase angle change when we change the diameter and length of the threaded adjustable inertance tube, it is helpful to determine the adjustable range of the diameter and length. The range of the diameter and length are determined both by the model prediction and by fabrication feasibility. After several iterative discussions with machinists, the final length and diameter for the adjustable inertance tube are chosen, as shown in TABLE 3-4.

TABLE 3-4 Parameters of the threaded adjustable inertance tube

L (m)	1.6~3.4	D (m)	0.0069~0.0010
f (Hz)	30~60	P_0 (MPa)	1.8~2.5
V_res (m^3)	1.5e-3~2e-3	m_dot (kg/s)	0.0005~0.004

The length of the adjustable inertance tube can vary from 1.6 m to 3.4 m, while the effective diameter changes from 7 mm to 10 mm. The change in phase angle and acoustic power corresponding to these length and diameter variations are shown in

FIGURE 3-17 and FIGURE 3-18. FIGURE 3-17 displays the threaded adjustable inertance tube phase shifting ability at 30 Hz. The solid line represents the phase angle and the dash line stands for acoustic power. The phase angle changes from -30° to 0° and the acoustic power varies from 1200 W to 1400 W when the threaded adjustable inertance tube diameter changes from 7 mm to 9 mm and length changes from 1.25 m to 3.14 m.

In FIGURE 3-18, the operating frequency is 45 Hz. The phase angle shifts from -40° to -65° as the diameter changes from 7 mm to 9 mm. With a 45 Hz operating frequency, the threaded inertance tube can provide a 25° phase shift. **Error! Reference source not found.** shows phase shift and acoustic power change at 60 Hz. The phase angle shifts from -62° to -74°, only 12° phase change. These calculations suggest a significant influence of the operating frequency on the resulting phase angle shift ability for the threaded adjustable inertance tube. Therefore the experimental measurements, explore the phase shifting abilities under working frequencies between 30 Hz and 60 Hz.

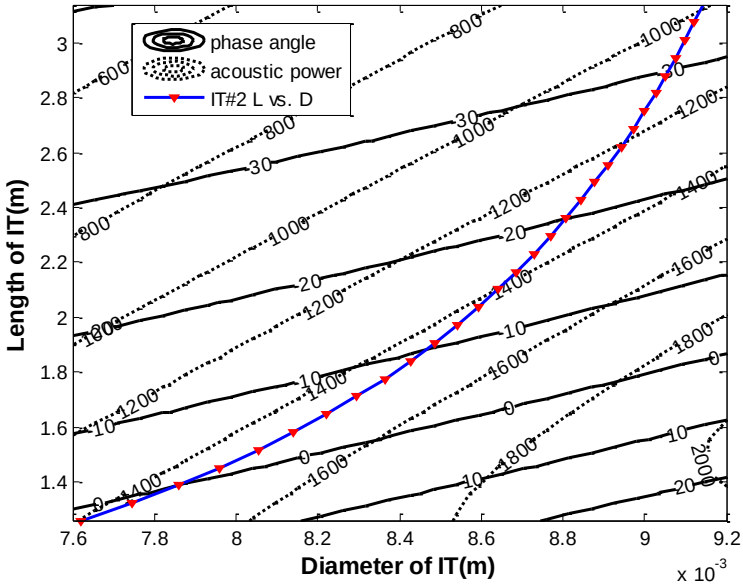

FIGURE 3-17 Contour plot of phase angle shift of IT#3 at 30 Hz

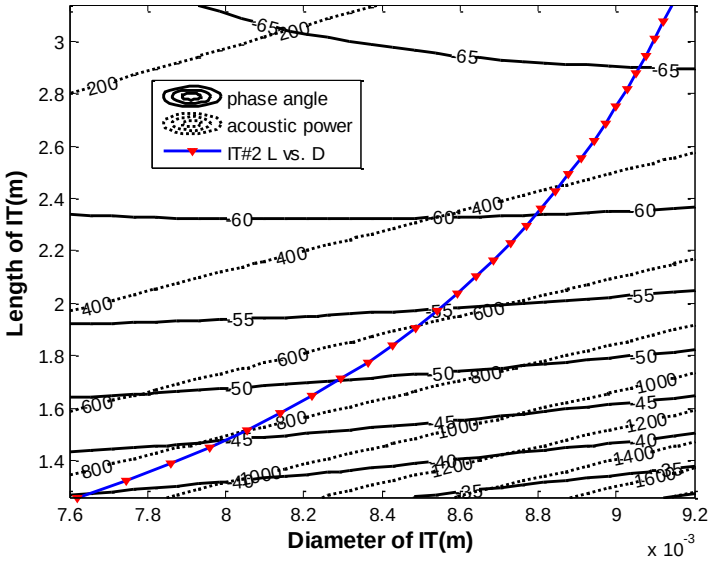

FIGURE 3-18 Contour plot of phase angle shift of IT#3 at 45 Hz

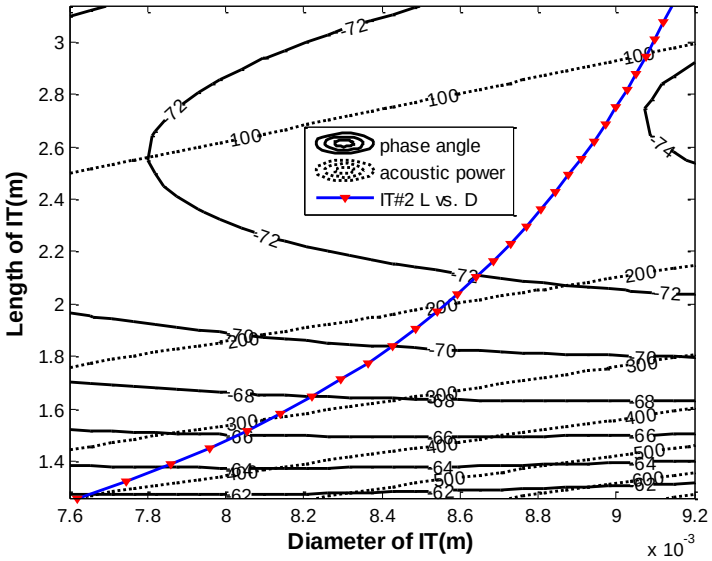

FIGURE 3-19 Contour plot of phase angle shift of IT#3 at 60 Hz

The phase angle between the pressure wave and mass flow rate is not only sensitive to the operating frequency, but also to other working parameters, such as the reservoir volume and charge pressure, as suggested by the parameters shown in TABLE 3-4.

Error! Reference source not found. shows the phase angle shift corresponding to the change of the reservoir volume. The working conditions are shown on the figure. The phase angle changes from -73.56° to -73.64° when the volume of the reservoir changes from 1.5 L to 2 L. The phase angle change is only 0.08° with a very large change of the reservoir volume. From this perspective, the phase angle change with the reservoir volume is not as sensitive as its change as a function of the diameter. FIGURE 3-21 displays the phase shift at different charge pressures. The phase angle changes from -72° to -77° when the mean charge pressure varies from 1.8 MPa to 2.5 MPa. There is 5°

phase angle shift with the change of the mean pressure, which is not very large. The phase angle shift is not that sensitive to the change of the mean pressure.

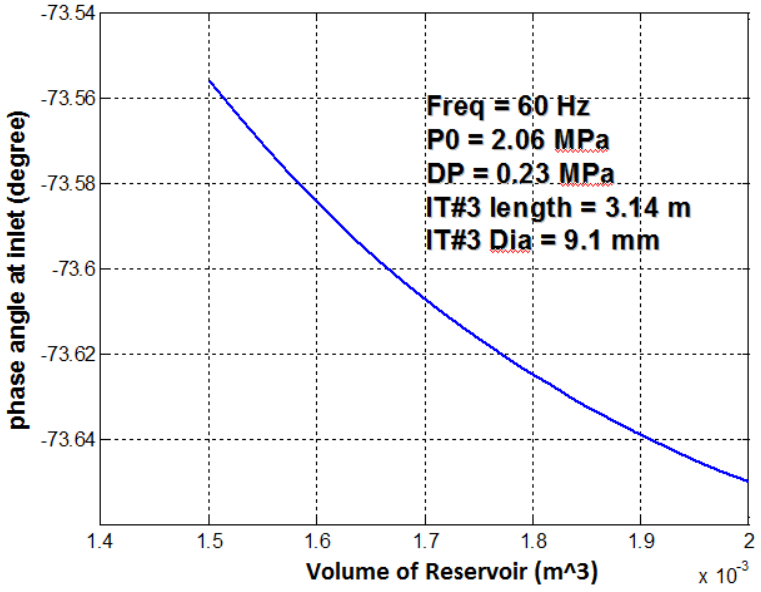

FIGURE 3-20 Phase angle vs. volume of the reservoir.

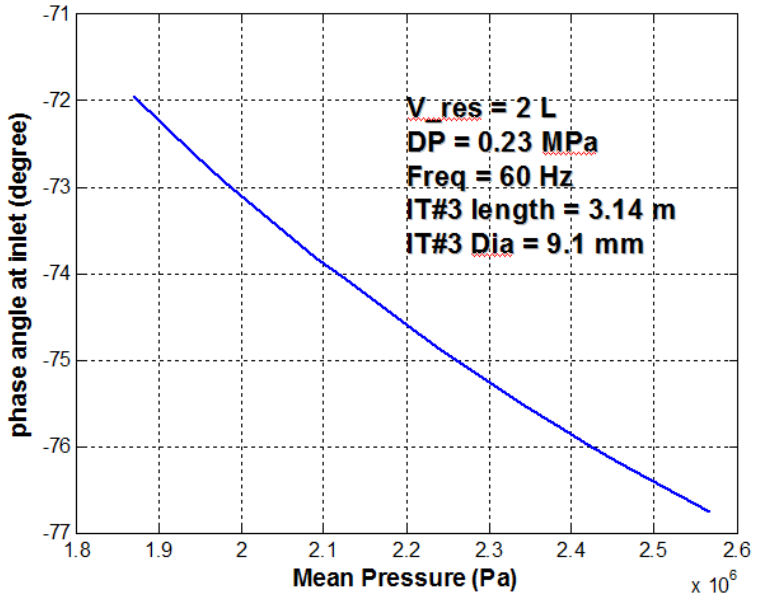

FIGURE 3-21 Phase angle vs. mean pressure.

Error! Reference source not found. shows the phase angle shift vs. working frequency. As the frequency goes from 30 Hz to 60 Hz, the phase angle changes from -35° to -75°, a 40° phase shift. The experimental measurements also explore the significant influence of frequency on the phase shift. **Error! Reference source not found.** displays the phase angle change vs. the change of pressure amplitude. There is almost a 9° phase shift as a result of changing the pressure amplitude from 0.16 MPa to 0.3 MPa. In the experiment, a change of the input current to the linear compressor enables an equivalent pressure amplitude change.

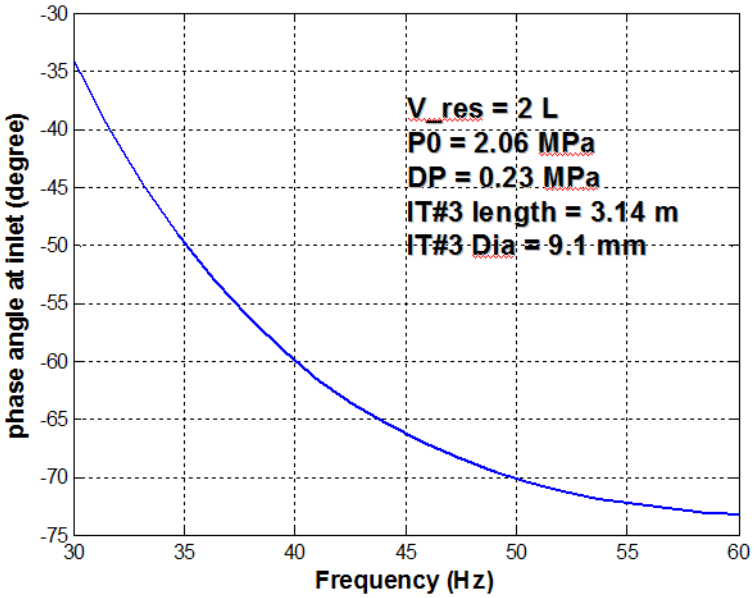

FIGURE 3-22 Phase angle vs. working frequency

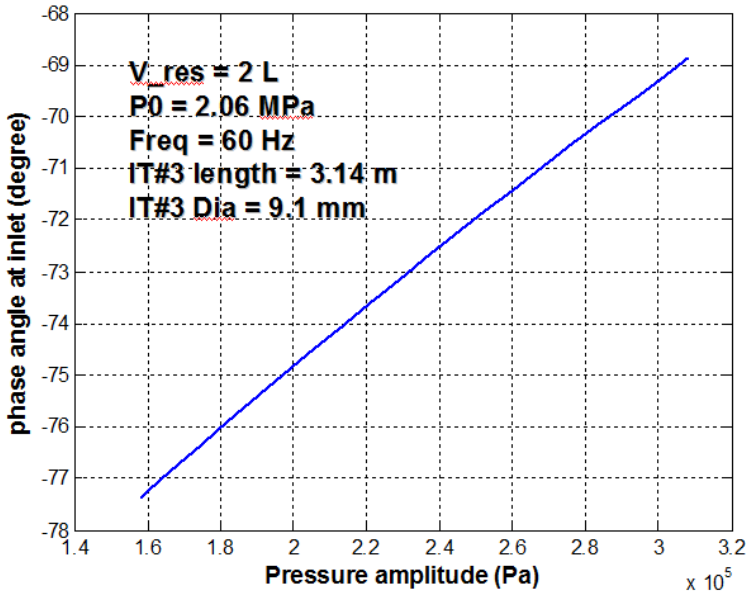

FIGURE 3-23 Phase angle vs. pressure amplitude

The phase angle between the mass flow rate and pressure is not sensitive to the change of the charging pressure, volume of the reservoir and the pressure amplitude, but very sensitive to the change of the operation frequency. In threaded adjustable inertance tube experiment, not only the operation frequency but also the diameter and length of the inertance tube will be changed in the real time to detect the phase angle shift performance of the threaded adjustable inertance tube.

3.4 Design and fabrication of key hardware components

The three key components for the experimental measurements are the threaded adjustable inertance tube, a CFIC Q-Drive model 2S297W TwinSTAR Pressure Wave Generator, and the screen-pack mass flow meter. The top of the threaded adjustable inertance tube includes a fin array to help dissipate heat from the reservoir to the environment. As shown in FIGURE 3-24, the two-liter reservoir is located inside the top

cover of the adjustable inertance tube assembly. The inertance tube is created by the channel between the root of the inner screw and the teeth of the outer screw. There are stops at each end of the threaded channel. The top stop is fixed to outer screw and the bottom stop is fixed to the inner screw so that as the outer screw travels from the bottommost position to the topmost position the length of large diameter inertance tube will increase from 0 to 1.86 m. At the bottommost position, the inertance tube length and effective diameter are 1.74 m and 7 mm respectively. The inner screw remains stationary while the outer screw is rotated from bottom to top. The rotating process can occur while the pulse tube cryocooler is operating so that the change in the dimensions of the inertance tube will cause a change in the phase angle at the cold end of the regenerator. This feature provides a convenient and direct method to determine the optimum working conditions of the specific pulse tube.

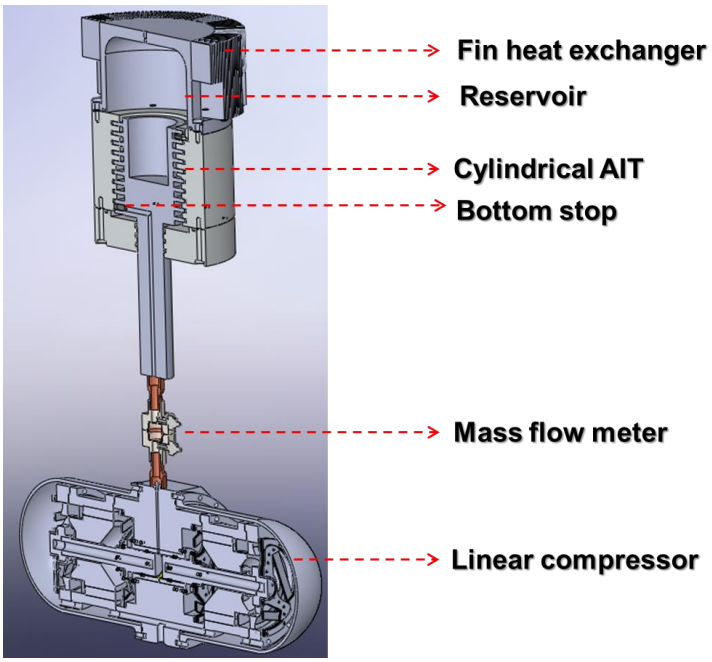

FIGURE 3-24 Configuration of the threaded adjustable inertance tube

The mass flow meter is located at the inlet of the threaded adjustable inertance tube and consists of two pressure transducers mounted on each side of the copper screen pack. By measuring the pressure drop across the screen pack, we can determine the magnitude and phase of the oscillating mass flow at the inertance tube inlet.

Two cooling water systems are used to cool the working gas coming out of the compressor. One removes heat directly from the compressor and the other reduces the working gas temperature to the ambient temperature before it enters the inertance tube. The linear compressor generates a large amount of joule heat when running for a long time, heat that must be removed or it will melt the aluminum case and copper coil inside the linear motor. A second cooling water coil is used to remove heat from the helium gas before it enters the regenerator in order to increase the cooling capacity at the cold tip of the pulse tube cryocooler.

The main parts of the adjustable threaded inertance tube, which are inner screw and outer screw, are made of 6061 aluminum alloy. FIGURE 3-25 shows the fabricated inner screw. The left photo is the inner screw before hard coat anodizing the surface, while the right one shows the inner screw after the hard coat anodizing. Originally, a Teflon coating was envisioned to reduce the friction coefficient between the threads of two screws. However, after discussion with the coating company, the Teflon coating approach was abandoned in favor of the hard coat anodizing applied to the surface of inner screw because the anodizing is relative easy to implement, decreases the friction force between the two screws, and reduces the leak path between the screws.

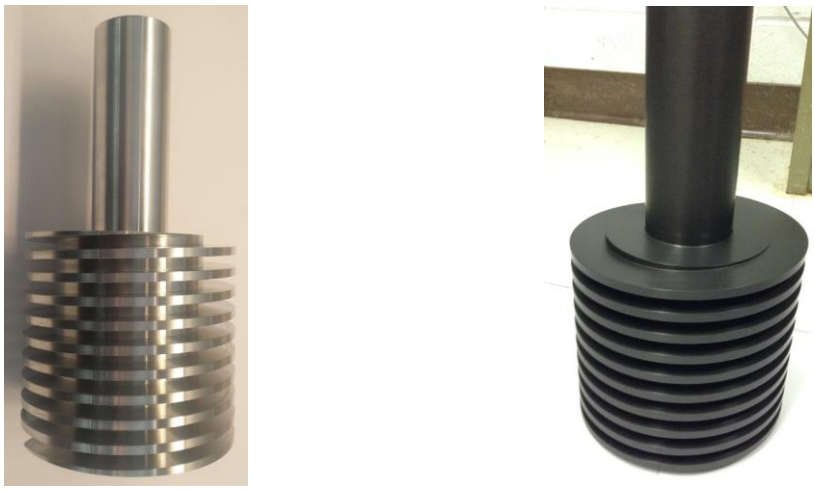

FIGURE 3-25 Photos of inner screw (left) without (right) with anodizing surface

After receiving the anodized inner screw, the outer screw is manufactured in accordance with the coated dimensions of the inner screw so that the tolerance between the threads of two screws could be minimized.

The top cover surrounded with fins generates the reservoir volume at the outlet of the inertance tube, as is shown in FIGURE 3-26. The dimensions of the fins were calculated based on maintaining the reservoir temperature no higher than 323K so that the phase shift behavior would not be affected by the change of the gas temperature in the reservoir. The fins were cut by CNC machine in the COE shop.

FIGURE 3-26 Photo of top cover with fin heat exchangers

The assembly of the adjustable inertance tube is shown in FIGURE 3-27. The inner screw is anchored to the linear compressor and remains fixed with respect to the top of the linear compressor. The bottom cover, outer screw and top cover are fixed to each other by using several bolts. The pressure inside the adjustable inertance tube is 300 psig while the ambient pressure is 14.7 psi. Three O-rings are embedded at the inner diameter of the bottom cover to seal the entire pressure vessel from the ambient pressure.

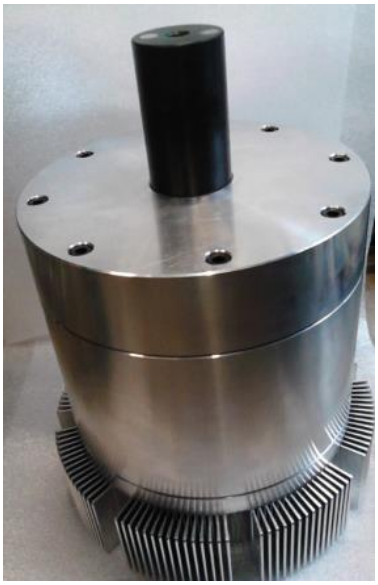

FIGURE 3-27 Assembly of adjustable threaded inertance tube

During the experiment test, the oscillation flow generated by the linear compressor enters the adjustable inertance tube from the bottom of the inner screw. By rotating the outer screw, the length and diameter of the adjustable inertance tube can be changed in the real time while the pulse tube is operating.

3.5 Summary

Conical and cylindrical threaded adjustable inertance tube were investigated and designed via the distributed component model. From the model prediction, the threaded adjustable inertance tube has the potential to produce a large phase angle shift while keeping the acoustic power as constant. Therefore, the threaded adjustable inertance tube was chosen for fabrication and assembly, in order to test the phase angle shift ability of the adjustable inertance tube.

The detailed design parameters of the adjustable inertance tube have also been determined. Through several iterative discussions with the COE machinists, the final parameters, such as the dimensions of finned heat exchanger, the required torque to rotate the outer screw, the number of bolts required the accommodate the operating pressure, and the diameter of the channel connecting the warm end of the pulse tube and inlet of the adjustable inertance tube have been determined through appropriate calculations.

4 Modified Distributed Component Model and Experimental Results

The components of the threaded adjustable inertance tube were fabricated in the college of engineering shop. The helical groove for the inner screw and outer screw were manufactured by using a CNC machine. After fabrication, the entire adjustable inertance tube was mounted on the top of the linear compressor, which is used as a pressure wave generator. The screen pack mass flow meter connects the outlet of linear compressor and adjustable inertance tube. The two pressure transducers mounted at each end of the mass flow meter measure the pressure waves. The pressure difference between these two pressure transducers can be used to estimate the amplitude and phase angle of the mass flow rate at inlet of inertance tube[46]. The inner screw is fixed and rigidly mounted to the linear compressor while the outer screw is bolted to the top cover that seals the adjustable inertance tube and forms the reservoir at the far end of the adjustable inertance tube. During the operation of the pulse tube cryocooler, the phase angle between the mass flow rate and pressure wave can be adjusted by rotating the outer screw from the bottommost position to the topmost position. Before running the adjustable inertance tube experiment, several theoretical predictions were made using the Distributed Component Model.

4.1 Modified Distributed Component Model

4.1.1 Distributed Component Model Prediction

The distributed component model was first introduced by Schunk, Nellis and Pfotenhauer in 2005[35]. This model separates the inertance tube into several segments, and calculates the compliance, inertia and resistance for each section by using the local Reynolds Number and local frication factor, so that it can predict the phase angle behavior of the inertance tube at each location. A two-section version of the distributed component model, introduced in chapter two, was adopted where the length of the first section is 1.74 m and the second section varies from 0 m to 1.86 m. The phase angle distribution caused by rotating of the outer screw of the adjustable threaded inertance tube can be generated by using a MATLAB version of the distributed component model.

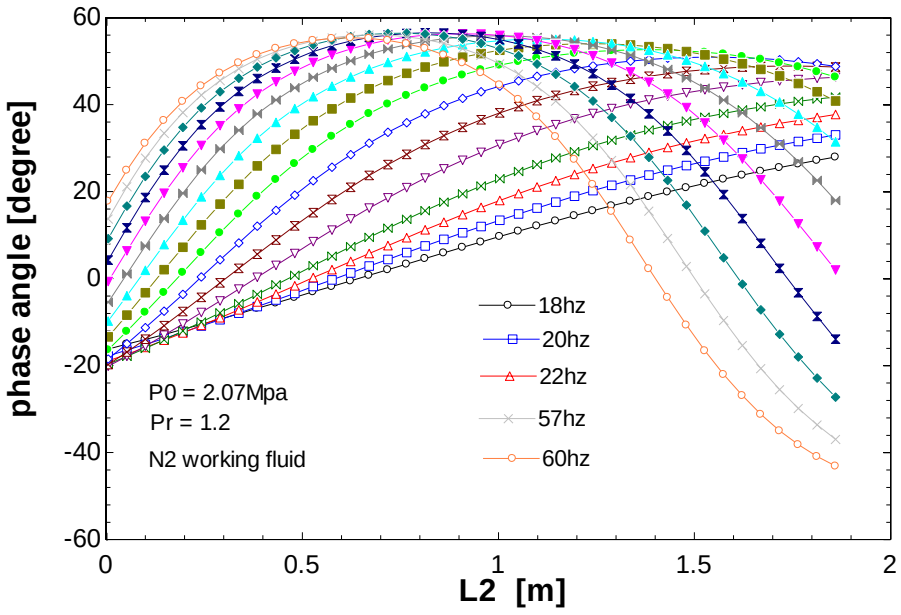

FIGURE 4-1 Phase angle shift with length of larger diameter inertance tube

FIGURE 4-1 illustrates the phase angle at the pulse tube end of the inertance tube as a function of length change of the large diameter portion of the cylindrical threaded

inertance tube, as calculated by the distributed component model. The results shown in FIGURE 4-1, are calculated with nitrogen as the working fluid, with a 2.07 MPa charge pressure, and the operating frequencies ranging from 18 Hz to 60 Hz, at 3 Hz intervals. From this plot, the phase angle varies from 60° to -60° as the length of the large diameter threaded inertance tube increase from 0 m to 1.8 m. This amount of phase angle shift is large enough to allow the detection of the optimum phase angle for a specific pulse tube cryocooler. Some commercial pulse tube cryocoolers work in the 60 Hz frequency range, and could benefit from such a large phase angle shift by adjusting the inertance tube length and diameter in order to optimize the pulse tube performance.

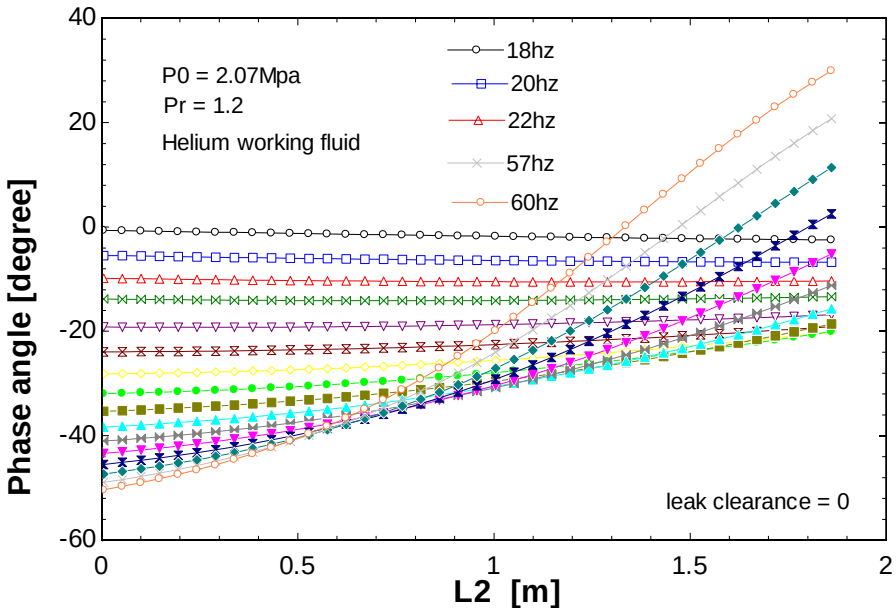

FIGURE 4-2 Phase angle shift with length of large diameter inertance tube using He

The results shown in FIGURE 4-2, are calculated with helium as the working fluid and the charge pressure of 2.07 MPa. From the FIGURE 4-2, the phase angle varies

from -50° to 30°, as the length increases from 0 m to 1.8 m. When the frequency is 18 Hz, there is essentially no phase angle change as the length varies from 0 m to 1.8 m. Because the viscosity of helium is fairly small, it is easier to produce a large phase angle shift at a higher frequency, such as 60 Hz, in comparison of the lower frequency, as shown in FIGURE 4-2. If the operating frequency increases to 60 Hz, the phase angle at the inlet of the inertance tube increases from -50° to 30°, as the length rises from 0 m to 1.8 m. The results shown in both FIGURE 4-1 and FIGURE 4-2 are from a version of the Distributed Component Model that does not account for leaks between the threads of the two screws or the entrance effect along the threads.

The simple distributed component model only accounts for the compliance, resistance, and inertia caused by the inertance tube. However, the adjustable inertance tube as built, includes leaks between the threads and entrance effects from the inertance tube channel to the leak gap. Therefore, the model has been modified in order to better match the experimental measurement.

4.1.2 Leak resistance estimation

The inertance tube channel is formed by gap between the teeth of the inner and outer screws, thus, a tiny leakage channel between the screws introduces an additional flow conductance (or resistance) in the threaded adjustable inertance tube. As a first step in characterizing the influence of the leaks in the threaded adjustable inertance tube, it is helpful to compare the leak resistance with the total inertance tube channel resistance. The geometry of the leak passage is depicted in FIGURE 4-3 below. In FIGURE 4-3, the

inertance tube is formed by the gap between the root of the inner screw and the teeth of the outer screw. There are two different heights of the outer screw teeth, generating two inertance tubes with different effective diameters. The engagement length of the threads is different in these two regions, resulting in two different leak passages from the main inertance tube channel to the average pressure condition. Note that the gap between the root of the outer screw and the teeth of the inner screw remains at the average (or charge) pressure. In the region of the smaller diameter tube, the leak is small because the leak channel engagement length is larger. The length of the small leak is shown on FIGURE 4-3, indicated as $L_{small,lk}$. For the large diameter threaded inertance tube, the engagement length is small, leading to a large leak. The length of the large leak passage is shown on FIGURE 4-3, depicted as $L_{large,lk}$.

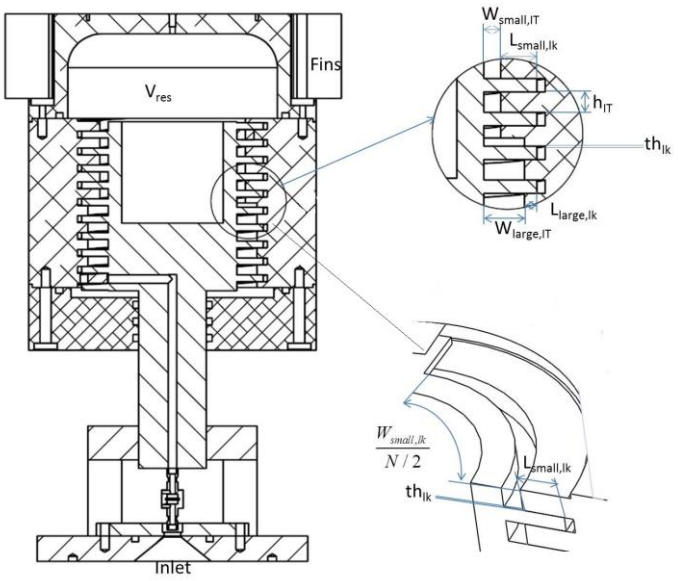

FIGURE 4-3 Schematic of the adjustable threaded inertance tube (4.5 turns)

Since the geometry of the adjustable inertance tube is different from the traditional inertance tube configuration and there is no leakage in a conventional inertance tube, the leak resistance needs to be introduced in the fluid circuit. The magnitude of the leak resistance and the magnitude of the inertance tube resistance are compared to figure out the significance of the leak resistance. In the geometry, the length of small leak is 14 mm; the length of large leak is 5 mm. The cross sectional area of the leak is calculated by using the clearance gap of the leak passage and the total perimeter of the leak passage, and the leak resistance is shown in the equation below:

$$R_{leak,large} = \frac{L_{leak,large}}{A_{leak,large}} = \frac{L_{leak,large}}{th_{lk} \cdot num \cdot \pi D_{leak,large}} \tag{4-1}$$

$$R_{leak,small} = \frac{L_{leak,small}}{A_{leak,small}} = \frac{L_{leak,small}}{th_{lk} \cdot num \cdot \pi D_{leak,small}} \tag{4-2}$$

where $D_{leak,small}$ and $D_{leak,\ large}$ are the average diameter of helical groove between outer screw and inner screw, and *num* is the total number of turns of the adjustable threaded inertance tube. The approximate fluid resistance of the main inertance tube is:

$$R_{large,IT} = \frac{4 \cdot num \cdot D_{leak,large}}{D_{large,IT}^{\ 2}} \tag{4-3}$$

$$R_{small,IT} = \frac{4 \cdot num \cdot D_{leak,small}}{D_{small,IT}^{\ 2}} \tag{4-4}$$

Here $R_{Lage,IT,}$ and $R_{small,IT,}$ stand for the inertance tube channel resistance. $D_{Lage,IT,}$ and $D_{small,IT,}$ are the effective diameter of large inertance tube and small inertance tube,

respectively. Using the associated dimensions for the inertance tube channels, one finds that the flow resistance for the large and small tubes is around 11858 1/m and 22568 1/m respectively. If the clearance gap thickness is set as 20 um, the large leak resistance is 575 1/m, and the small leak resistance is 1768 1/m. The large leak resistance is only 4.85% of the large tube resistance, and the small leak resistance is approximately 7.83% of the small tube resistance. The conclusion is that the fluid will primarily go through the leak passage directly to the average pressure without passing through the entire inertance tube. Therefore, it is difficult to eliminate the leak conductance since the leak is inherent in the threaded adjustable inertance tube configuration.

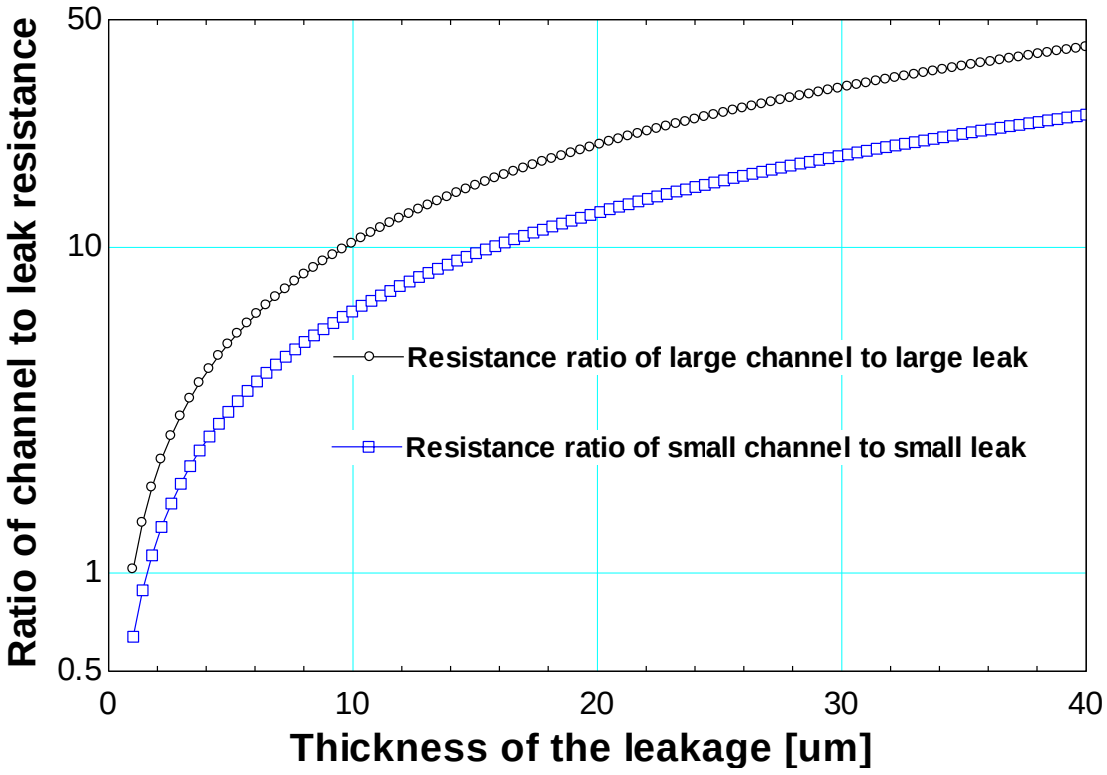

FIGURE 4-4 Ratio of channel to leak resistance vs. clearance gap thickness

In order to compare the magnitude of the leak resistance to the inertance tube channel resistance as a function of the clearance gap thickness, a resistance ratio plot has been generated as shown in. FIGURE 4-4. The resistance ratio for the large diameter inertance tube approaches to 1 if the clearance gap thickness is only 1 um. For the smaller diameter inertance tube, the resistance ratio is 1 if the clearance gap thickness is close to 3 um. If the clearance gap thickness is greater than 10 um, the channel resistance is 10 times larger than that of the leak, resulting in large leaks through the clearance gap. In reality, the clearance gap thickness between the threads of inner screw and outer screw is hard to reduce, and the large leaks between the threads of the two screws will definitely deteriorate the phase shifting ability of the threaded adjustable inertance tube.

Since there are some leaks in the adjustable inertance tube, the original distributed component model could not precisely predict the phase angle behavior of the new adjustable threaded inertance tube. A modified distributed component model has therefore been generated, including the leak resistance and entrance effect inside the device.

4.1.3 Modified Distributed Component Model

The schematic of the adjustable inertance tube is depicted in FIGURE 4-5. By turning the outer screw from its top position to its bottom position, the length of the small diameter passage remains constant while the portion of large diameter tube will be reduced.

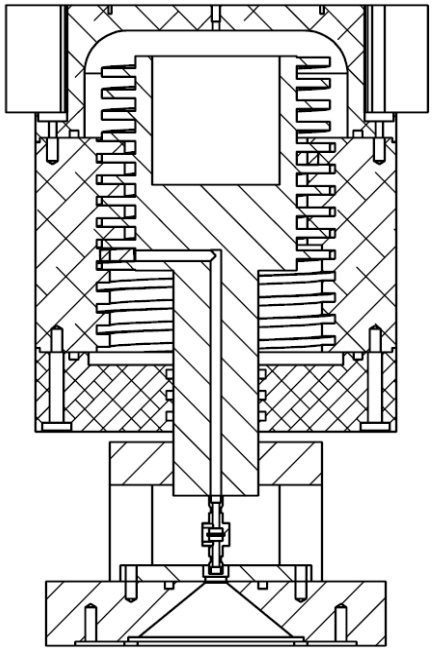

FIGURE 4-5 Schematic of the adjustable threaded inertance tube

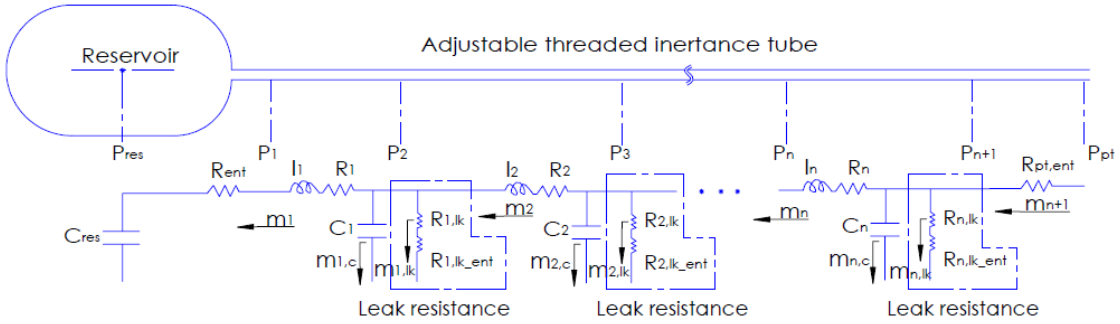

FIGURE 4-6 Modified adjustable inertance tube fluid impedance network

A schematic of the fluid impedance network including the additional components that are used to model the leakage path (which include both an entrance effect and frictional loss) is shown in FIGURE 4-6; note that the additional fluid components are shown in the dashed line boxes in FIGURE 4-6. The details regarding the calculation of

the fluid resistance, compliance and inertia can be found in the papers [35, 47]. Here, we will confine our discussion to the leakage and entrance effect resistances that have been added to the fluid network. The leakage and entrance effect resistances are in series and they are together placed in parallel with the compliance and the rest of the impedance, as depicted in FIGURE 4-6.

The resistance of the leak is given by:

$$R_{lk} = \frac{\Delta P_{lk}}{\dot{m}_{lk}} = \frac{f_{lk}\frac{L_{lk}}{D_{lk}}(\frac{1}{2}\rho_{lk}V_{lk}^2)}{\rho_{lk}V_{lk}th_{lk}W_{lk}/N} = \frac{V_{lk}f_{lk}L_{lk}N}{2D_{lk}th_{lk}W_{lk}} \qquad (4\text{-}5)$$

where V_{lk} is the velocity through the leak, L_{lk} ($L_{small,lk}$ and $L_{large,lk}$ in FIGURE 4-3) are the engagement depths for each screw, (separate dimensions for the large thread region $L_{large,lk}$ and the small thread region $L_{small,lk}$ are listed in TABLE 4-1); n in FIGURE 4-6 is the number of subsections used to model the total inertance tube, half of the number of subsections are used for the large thread region and half for the small thread region; D_{lk} is the hydraulic diameter of the leak channel, which is calculated as four times the cross sectional area divided by the wetted perimeter of the leakage path. th_{lk} is the gap thickness between the threads of the two screws, and W_{lk} is the width of the leak gap, which is the helical thread length from the inlet to the outlet of each section. These dimensions are depicted in FIGURE 4-3 and their values are listed in TABLE 4-1. Since the maximum Reynolds number going through the leak passage is less than 1400 for the conditions considered here f_{lk} is the friction factor associated with the developing region for laminar flow in a rectangular duct given by the equation below[49]:

$$\bar{f}_{lk} \approx \frac{4}{\mathrm{Re}_{lk}}\left[\frac{\frac{3.44}{\sqrt{L^+}}+\frac{\frac{1.25}{4L^+}+\frac{f_{fd,h}\,\mathrm{Re}_{lk}}{4}-\frac{3.44}{\sqrt{L^+}}}{1+\frac{0.00021}{(L^+)^2}}}\right] \tag{4-6}$$

where $f_{fd,h}$ is $96/Re_{lk}$, since the aspect ratio of the leak passage approaches 0[49]. Re_{lk} is the Reynolds number for this leakage:

$$\mathrm{Re}_{lk} = \frac{\rho V_{lk} D_{lk}}{\mu} \tag{4-7}$$

The parameter ρ is the gas density and μ is the viscosity of the working fluid. The gas properties are determined by assuming room temperature and the average or charge pressure measured in the adjustable inertance tube. L^+ is defined in the following equation:

$$L^+ = \frac{L_{lk}}{D_{lk}\,\mathrm{Re}_{lk}} \tag{4-8}$$

In order to estimate the entrance effect from the inertance tube to the leak passage, an orifice equation is used [50].

$$R_{ent} = \frac{\sqrt{\Delta P_{ent}}}{\sqrt{2\rho} C_{ent} F_{ent} A_{ent}} \tag{4-9}$$

where $\triangle P_{ent}$ is a pressure difference through leak passage, A_{ent} is the cross sectional area of the leak, calculated as the product of the gap thickness and the width of the leak within the subsection, and C_{ent} is the discharge coefficient given by the equation below[50]

$$C_{ent} = 0.5959 + 0.0312\beta^{2.1} - 0.184\beta^{8} + 91.71\beta^{2.5}\,\mathrm{Re}_{lk}^{-0.75} + \frac{0.0389\beta^{4}}{1-\beta^{4}} - 0.0158\beta^{3} \tag{4-10}$$

$$\beta = \frac{D_{lk}}{D_{p}} \tag{4-11}$$

D_p is the hydraulic diameter of the threaded helical section from main inertance tube channel to the leakage channel, calculated by using equation (4-12);

$$D_{p} = \frac{4 \cdot h_{IT} \cdot (W_{small,lk} + W_{large,lk})}{h_{IT} + (W_{small,lk} + W_{large,lk})} \tag{4-12}$$

F_{ent} is given by the equation (4-13):

$$F_{ent} = \sqrt{\frac{1}{1-\beta^{4}}} \tag{4-13}$$

The calculation procedure used for the modified distributed component model is iterative. The total inertance tube, including both the large diameter and small diameter inertance tubes in series, is divided into n elements with half used for the large diameter tube and half used for the small diameter tube, and including the leak and entrance effect resistance in each element. The starting point for the iteration process includes an estimation of the Reynolds numbers, the velocity through the leak and the pressure difference across the leak at each node. The initial guess values of Reynolds number are estimated by assuming turbulent flow in the inertance tube channel. The pressure drop across the leak is assumed to be half of the pressure amplitude in the inertance tube. The

velocity going through the leakage is set as 100 m/s at beginning. The iteration process begins with the known impedance values for each node and the pressure amplitude at the interface between the pulse tube and the inertance tube, which are calculated based on the guess values. Then, the fluid network is solved in order to determine the new Reynolds numbers, new velocities through the leaks and the new pressure difference across the leaks. If the differences between these values and the values from the previous iteration are smaller than a tolerance limit ε, typically set to about 1e-11 for the Reynolds number, 1e-11 m/s for the leak velocity and 1e-11 pa for the leak pressure difference, then the calculation process is terminated and the acoustic power and phase angle at the pulse tube interface are calculated.

TABLE 4-1 Basic geometry parameters of the threaded adjustable inertance tube

Variables	Values	Variables	Values	Variables	Values
$L_{small,IT}$	1.74 m	$L_{large,IT}$	0-1.86 m	$W_{small,IT}$	6.35e-3 m
$W_{large,IT}$	15.24e-3m	h_{IT}	7.62e-3 m	V_{res}	1.5e-3 m^3
$L_{small,lk}$	14mm	$L_{large,lk}$	5mm	th_{lk}	16um

TABLE 4-1 summarizes the geometric parameters of the threaded adjustable inertance tube that was fabricated. The adjustable inertance tube has two different dimensioned channels in series; one channel is 6 mm in width and 8 mm in height, with length of 1.74 m; the other channel is 15 mm in width and 8 mm in height with length of

1.86 m. The hydraulic diameter of the small and large inertance tubes are 7 mm and 10 mm respectively. The leak gap thickness is assumed to be 16 um in the table, based on the theoretical leak resistance calculations. The thread engagement length is treated as the length of the leak passage, which are 13.7 mm and 4.8 mm for small diameter tube and large diameter pipe, separately.

Results from the two section Modified Distributed Component Model are verified by comparing them with those from the two section Distributed Component Model in the limit when the value th_{lk} approaches zero. The calculated phase angle at the compressor inlet in both cases is precisely -43.45 degree, and the mass flow through the channel for both the models is 0.0324 kg/s. Therefore, the Modified Distributed Component Model has the same phase angle prediction ability as the original Distributed Component Model.

FIGURE 4-8 shows the mass flow rate of nitrogen at the inlet of both the main inertance tube channel and through the leak. When the leak thickness is less than 34 μm, the flow that goes into the inertance tube is higher than the mass flow through the leak, and the threaded adjustable inertance tube can provide a phase angle shift ability as the outer screw was turned from 0 turns to 4.5 turns.

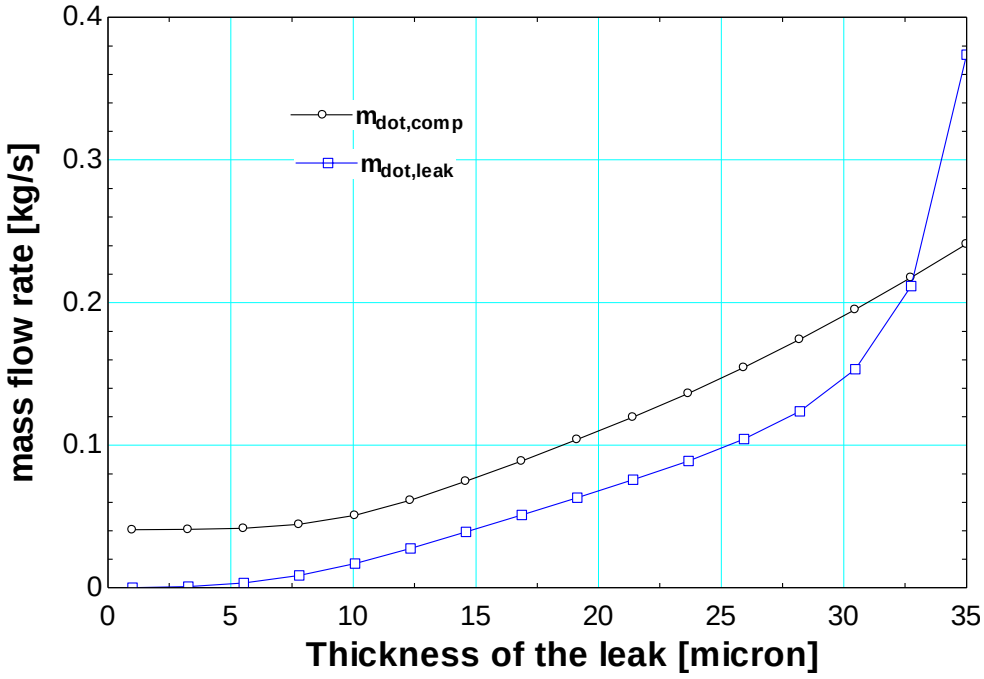

FIGURE 4-7 Mass flow rate with the increase of gap thickness (from 5 um to 35 um)

However, if we continue to increase the leak gap thickness to 40 μm, the mass flow through the leak will be larger than what flows through the main inertance tube channel, deteriorating the phase angle shift ability of the adjustable inertance tube. In order to maintain the pressure ratio at the inlet of 1.2, almost 40 kg/s of nitrogen is needed to fulfill this working condition with a 40 μm clearance gap thickness. In such a case, the gas will flow through the leak at the inlet without passing along the inertance tube. The result is also verified by FIGURE 4-7, showing that the mass flow through the channel is equal to the total mass flow through the leak, when the leak thickness is 34 μm.

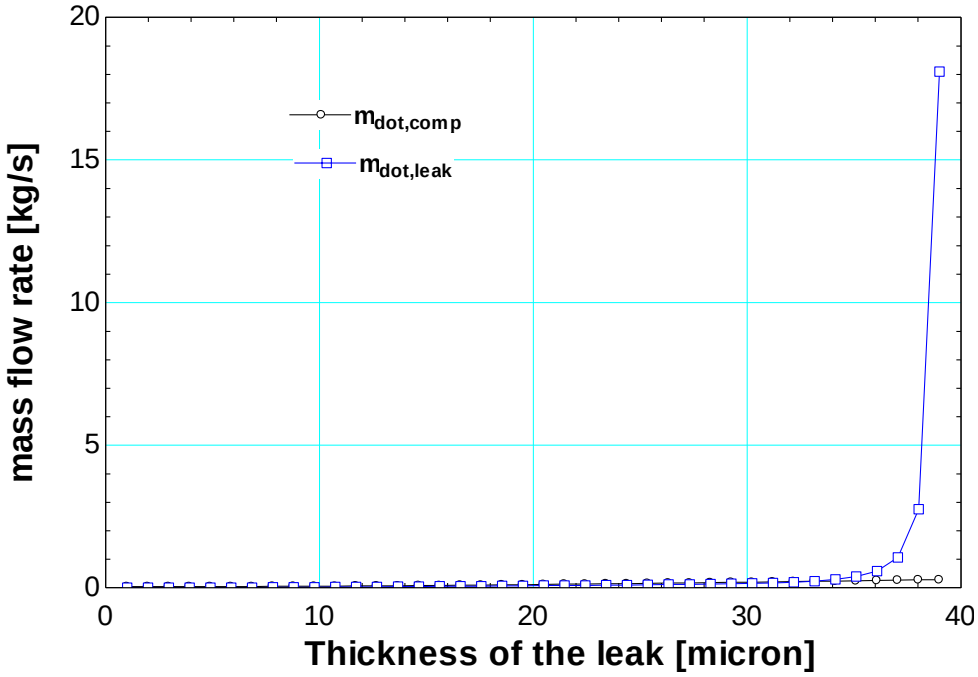

FIGURE 4-8 Mass flow rate with the increase of gap thickness (from 5 um to 40 um)

Furthermore, if we calculate the velocity at the inlet under the conditions of constant pressure ratio when the leak thickness is 34 μm, the local velocity at the leak passage is 353 m/s, which is equal to the local speed of sound of nitrogen 353 m/s; therefore, the flow is chocked at this thickness. FIGURE 4-9 shows the velocity at the leak entrance with the increase of the leak thickness all the way from 5 μm to 40 μm. Because the pressure ratio at the inlet is held constant at 1.2, the mass flow rate will increase dramatically up to 20 kg/s due to the chocked flow at the leak.

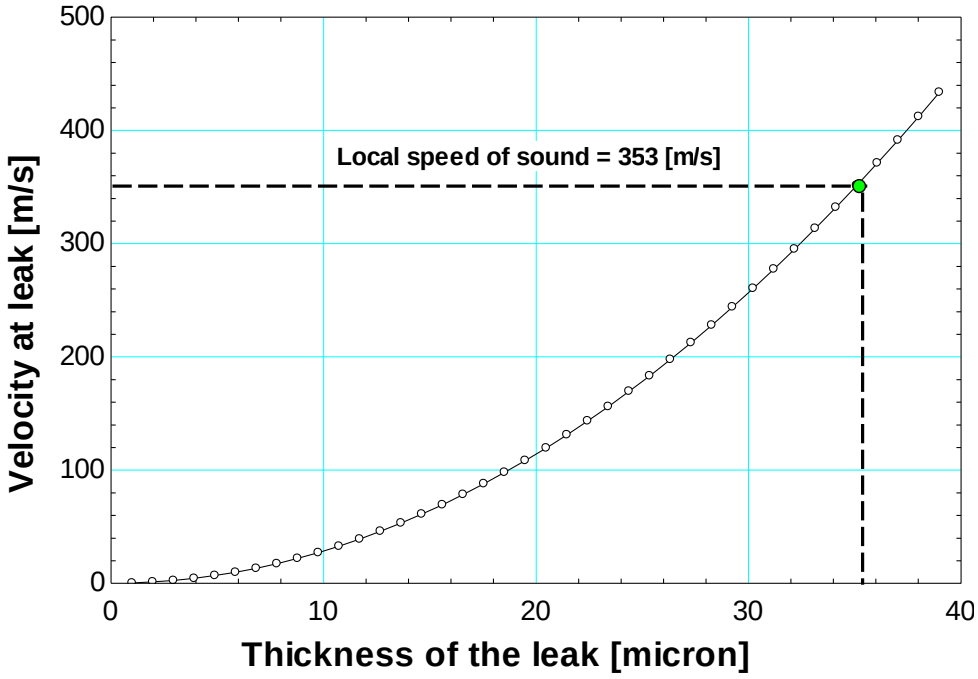

FIGURE 4-9 Velocity at leak with the increase of leak gap

In FIGURE 4-10, the leak gap is held constant at 36 μm, and the velocity at the leak increases from 40 m/s to 350 m/s as the pressure ratio increases from 1.02 to 1.2. In the modified distributed component model, the pressure ratio at the inlet of the inertance tube is held constant while building up the fluid circuit, which is also true in the experiments.

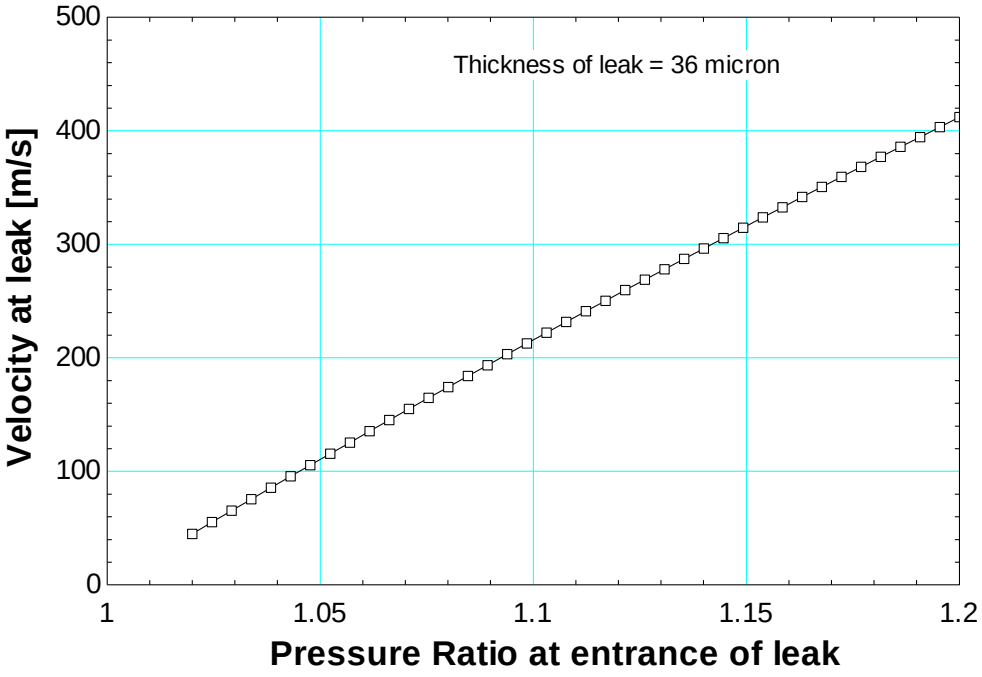

FIGURE 4-10 Leak velocity with the increase of the pressure ratio

After verifying the accuracy of the modified distributed component model, it has been used with a gap of 16 μm to determine the phase angle shift as a function of the length of the second portion of inertance tube, which is shown in FIGURE 4-11 and FIGURE 4-12 below.

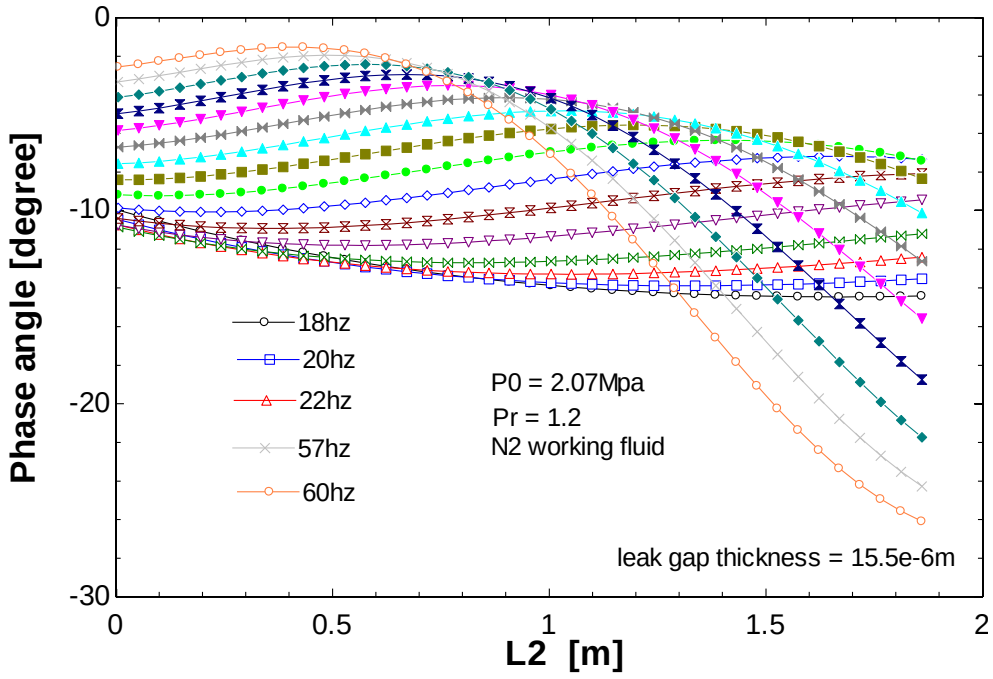

FIGURE 4-11 Phase angle shift computed by the Modified Distributed Component Model when using Nitrogen as the working fluid

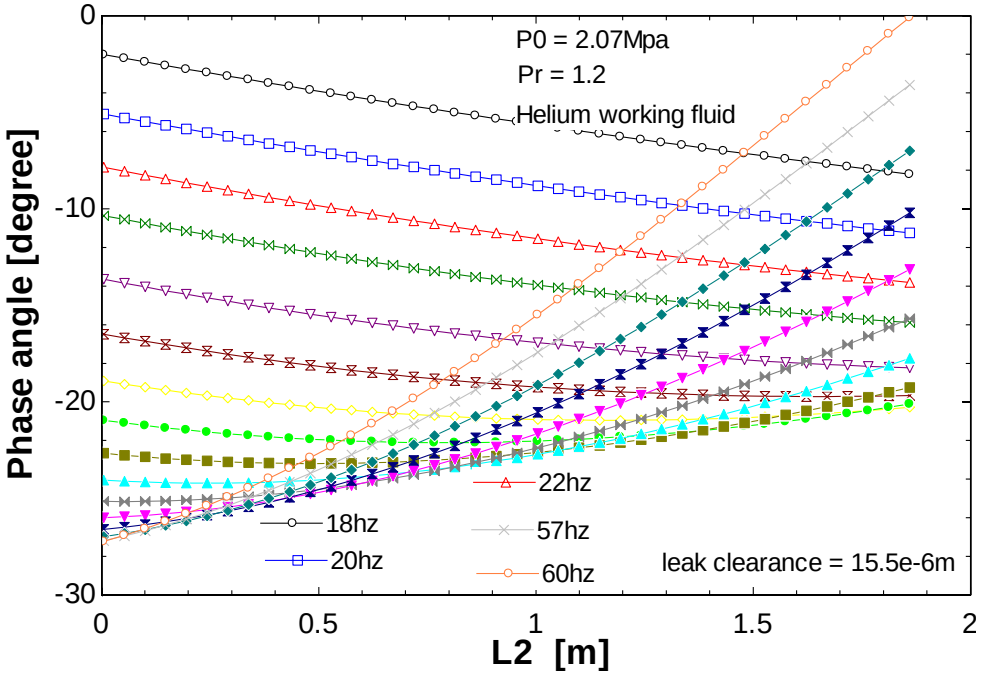

FIGURE 4-12 Phase angle shift by the Modified Distributed Component Model when using Helium as the working fluid

FIGURE 4-11 and FIGURE 4-12 show the phase angle shift predicted by the Modified Distributed Component Model (MDCM) as a function of the length of large diameter inertance tube; changing this value from 0 to 1.86 m corresponds to turning the outer screw from 0 to 4.5 turns. At the beginning of this chapter, FIGURE 4-1 is generated by the Distributed Component Model assuming that there are no leaks between the two screws. Note that the phase angle shift at 60 Hz can be adjusted from 60° to -60°, when the outer screw rotates from 0 turns to 4.5 turns (bottom to the top). Therefore, the adjustable inertance tube is predicted to have very good phase shift ability for the pulse tube cryocooler. However, the thread leakage along the adjustable inertance tube deteriorates the phase shifting performance. The 16 μm clearance leak dramatically reduces the phase angle adjustment; the phase angle will only change from 0° to -25° as the length of the large diameter inertance tube increases from 0 m to 1.86 m. The phase angle changes at lower frequencies are even smaller when the leakage is present.

4.2 Threaded adjustable Inertance Tube Experimental Results

The threaded adjustable Inertance Tube (TAIT) is mounted on the top of a linear compressor, (60 Amp, Q Drive model 2S297W TwinSTAR Pressure Wave generator). A mass flow meter operating by measuring the pressure difference across a copper screen pack is installed at the inlet of the adjustable inertance tube. A detailed description of this

mass flow meter can be found in reference [46]. FIGURE 4-13 displays the 3-D drawing (left) and physical photo (right) of the experiment. The fin heat exchanger around the reservoir dissipates the acoustic power as heat to the surrounding air. The reservoir connected to the exit of the inertance tube has an approximate total volume of 2 liters. The adjustable inertance tube is formed by the channel between the threads of the two screws. There are two stops at each end of the channel, which force the fluid to flow into the inertance tube and exit from the inertance tube into the reservoir.

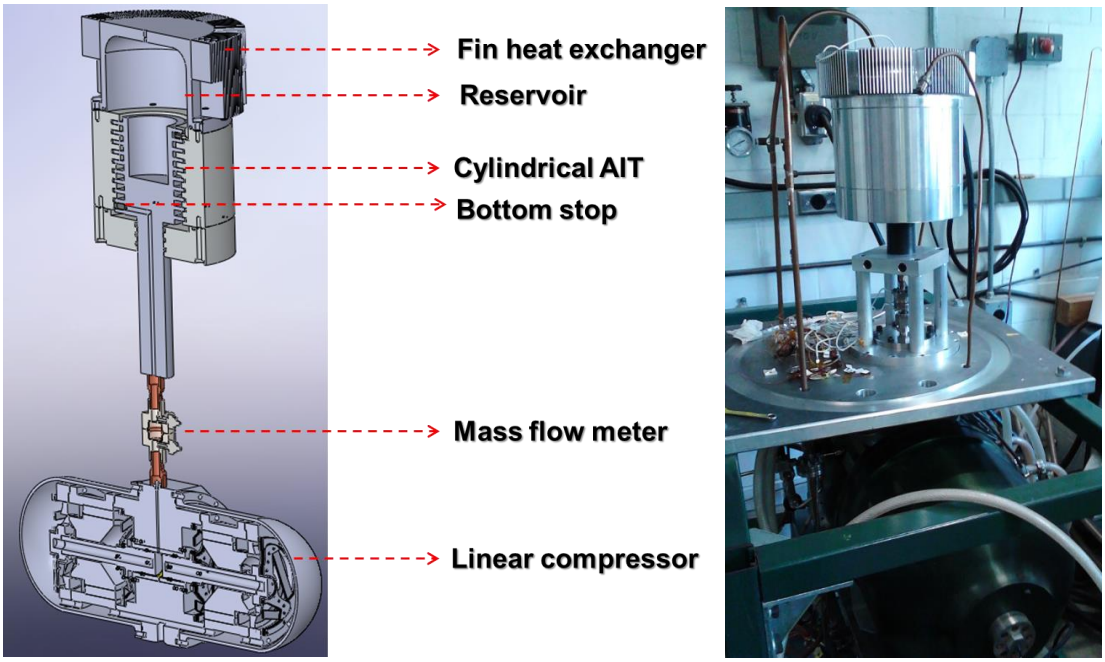

FIGURE 4-13 Configurations of threaded adjustable inertance tube experimental setup

4.2.1 Pressure and phase angle measurement

Endevco pressure transducers, model 8510B (0-500 psig) were used to measure the pressure oscillation across the mass flow meter and reservoir. The oscillation mass flow rate cannot be detected through the traditional direct flow meter, therefore, there are

two pressure sensors assembled on each side of the mass flow meter to measure the pressure differential which is approximately proportional to the mass flow rate at the inlet of adjustable inertance tube.

Nitrogen is used as working fluid with a charge pressure of 300 psig. FIGURE 4-14 shows the sinusoidal pressure wave generated by the linear compressor. The sinusoidal wave with the greatest amplitude represents the pressure at the inlet of the mass flow meter (from pressure transducer 1, P1); the smaller amplitude sinusoidal wave is associated with the pressure wave after the screen pack of the mass flow meter (from pressure transducer 2, P2). The line in the middle is the pressure amplitude at the reservoir side (from pressure transducer 3, P3), which, compared to the pressure across the mass flow meter, is not as obviously a sinusoidal pressure wave. The phase angle of the pressure difference (P1 – P2) with reference to the oscillation of P1 is approximately equal to the phase angle of the mass flow rate with respect to the pressure oscillation P1. Multiple cycles of the pressure wave data are collected to determine the precise phase angle.

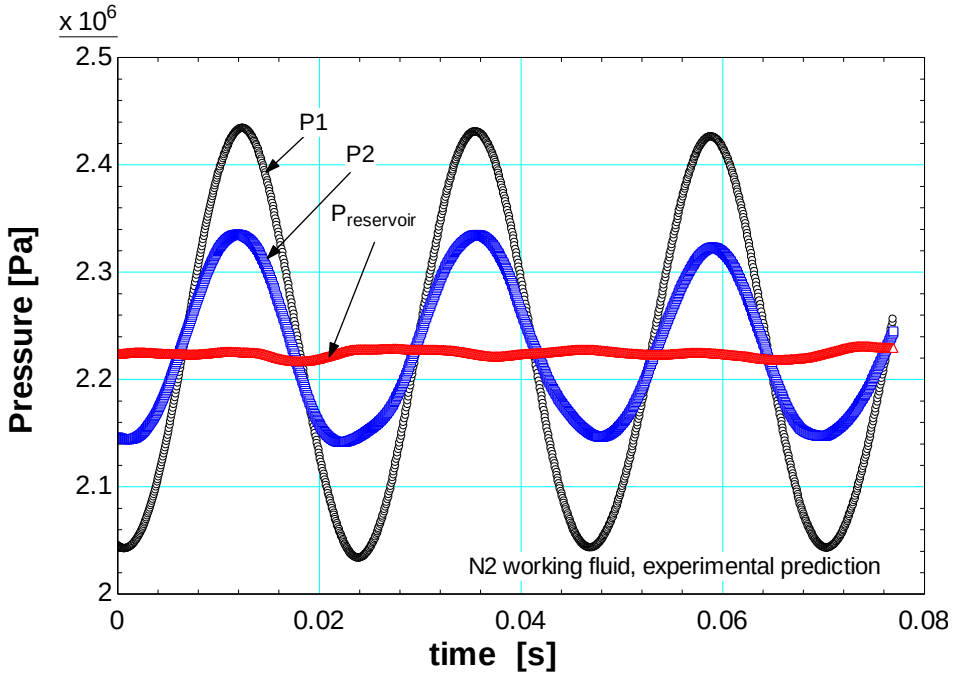

FIGURE 4-14 Pressure data with 300 PSIG charge pressure, 42Hz and 1.5 turns

FIGURE 4-15 shows the method used to determine the phase angle by analyzing the pressure data from the experiment. The pressure waves measured by the Endevco pressure transducers are precise enough to detect the phase angle at the inlet of the adjustable inertance tube. The triangle symbols indicate the pressure data measured from pressure transducer 1 mounted close to linear compressor side on the mass flow meter before the screen pack. The square symbols demonstrate the pressure data from pressure transducer 2 after the copper screen pack. The solid lines are generated from the curve fit equation determined with the MATLAB internal curve fit function. Only one cycle is shown in FIGURE 4-15, indicating that the phase angle difference between P1 and P2 can be calculated using the curve fit equation. In order to precisely determine the phase angle measurement, 42 cycles of pressure data are used to generate 42 sinusoidal curve fit

equations and provide 42 phase angle shifts. Therefore, the standard deviation for the phase angle shift can be calculated as well. The measured phase angle is then compared with the Modified Distributed Component Model prediction.

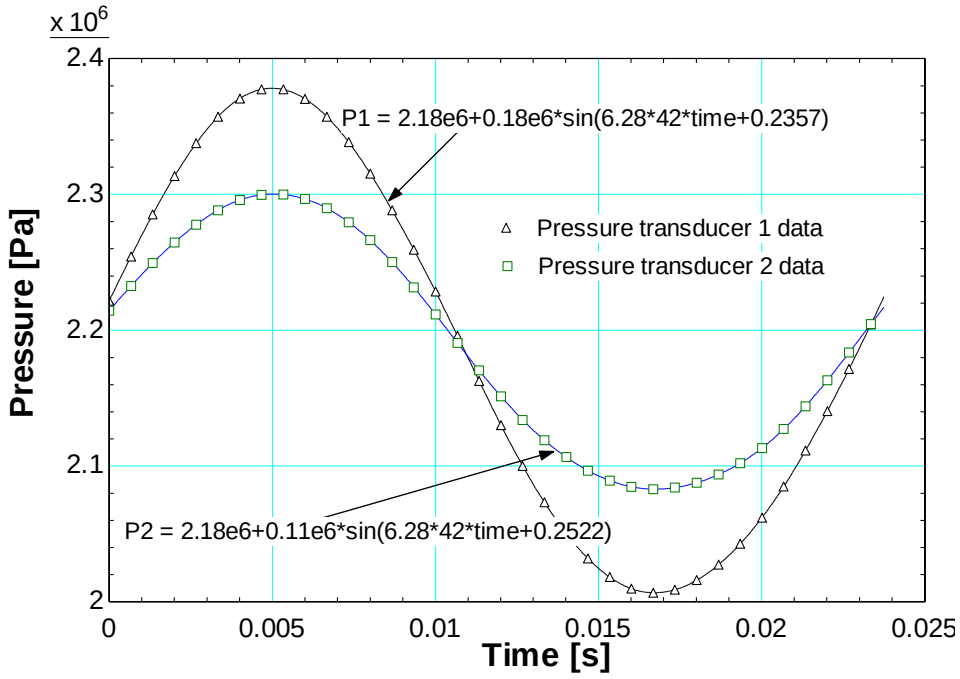

FIGURE 4-15 Sinusoidal curve fit equation to find the phase angle difference

4.2.2 Experiment without vacuum grease

In the primary experiment, nitrogen is used as working fluid with a 300 psig charge pressure. There are totally 4.5 turns for the outer screw to move. When the outer screw sits on the top position (4.5 turns), the length of large diameter inertance tube is 1.86 m, and the length of small diameter inertance tube is 1.74 m. During the experiment, the outer screw is rotated from the top position (4.5 turns) to the bottom position (0 turns), changing the length of large diameter inertance tube from 1.86 m to 0 m while

keeping the length of small diameter inertance tube constant, thus, the phase angle at the inlet of inertance tube could be varied by rotating the outer screw.

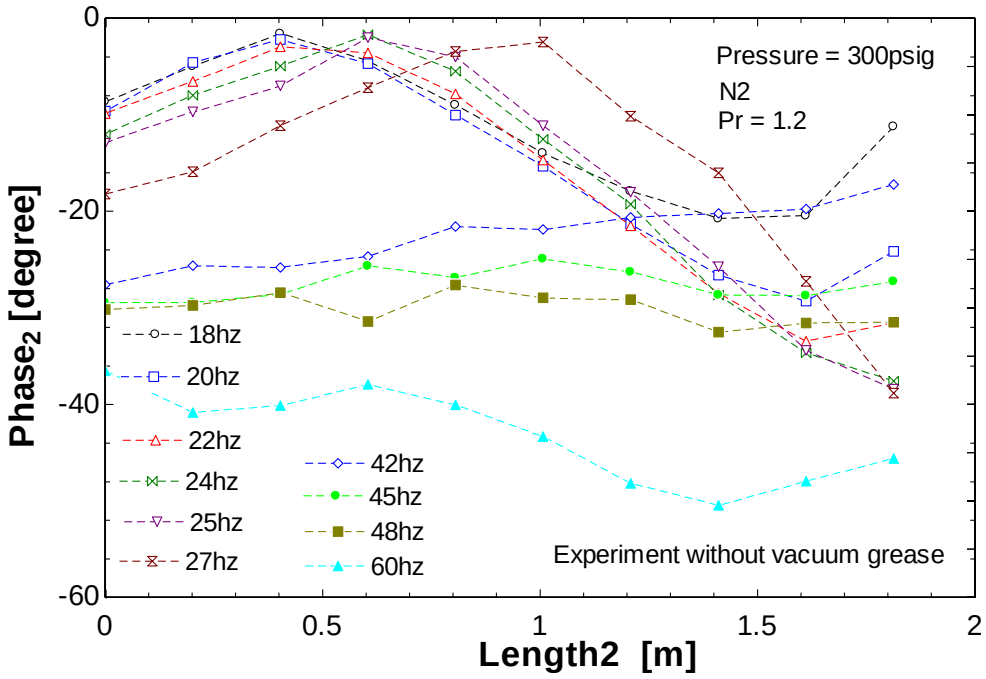

FIGURE 4-16 Phase angle shift vs. the length of the large diameter inertance tube

FIGURE 4-16 illustrates the phase angle shift at the inlet of the cylindrical threaded adjustable inertance tube by varying the length of the large diameter inertance tube from 0 m to 1.8 m. At the lower frequency, around 18 Hz, the phase angle shift is constrained from 0° to -20°. When the frequency is around 45 Hz, the phase angle almost stays constant around -30°, while at 60 Hz, the phase angle decreases a bit from -38° to -48°. The phase angle shift from the experiment is not the same as that predicted by the Distributed Component Model, which is shown in FIGURE 4-1 at the beginning of this chapter. From FIGURE 4-1, we expect the phase angle to vary from 60° to -60°, as the

outer screw is rotated from its bottom position (0 turns) to its top position (4.5 turns). The relatively small phase angle shift is probably caused by the leaks between the threads of the two screws, which deteriorate the phase angle shift ability of the threaded adjustable inertance tube.

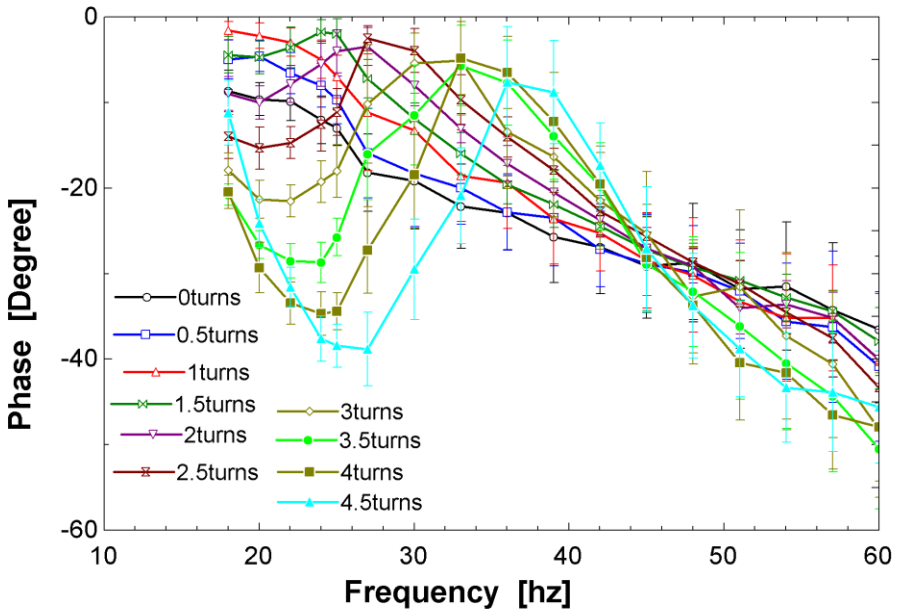

FIGURE 4-17 Phase angle vs. Frequency at different turns of outer screw

FIGURE 4-17 represents the phase angle shift with the operation frequency at different outer screw positions. The phase angle varies from 0° to -50°, as the frequency changes from 18 Hz to 60 Hz. The phase angle is very sensitive to the operating frequency, which is also verified by the Modified Distributed Component Model. From FIGURE 4-17, when the outer screw sits at the bottom position, the phase angle will decrease from -10° to -40° as the frequency increases from 18 Hz to 60 Hz. Also, the

maximum phase angle shift occurs at 27 Hz by changing the length of large diameter inertance tube.

In order to reduce the leak path between the threads, vacuum grease was applied between the threads of the two screws in the hope of improving the phase angle shift ability of the threaded adjustable inertance tube.

4.2.3 Phase angle measurement with vacuum grease

In order to decrease the leaks between the threads, a thin layer of vacuum grease was pasted on the threads of the inner and outer screws. The vacuum grease provides a partial seal between the two threads, resulting in some improvement of the phase angle shift ability.

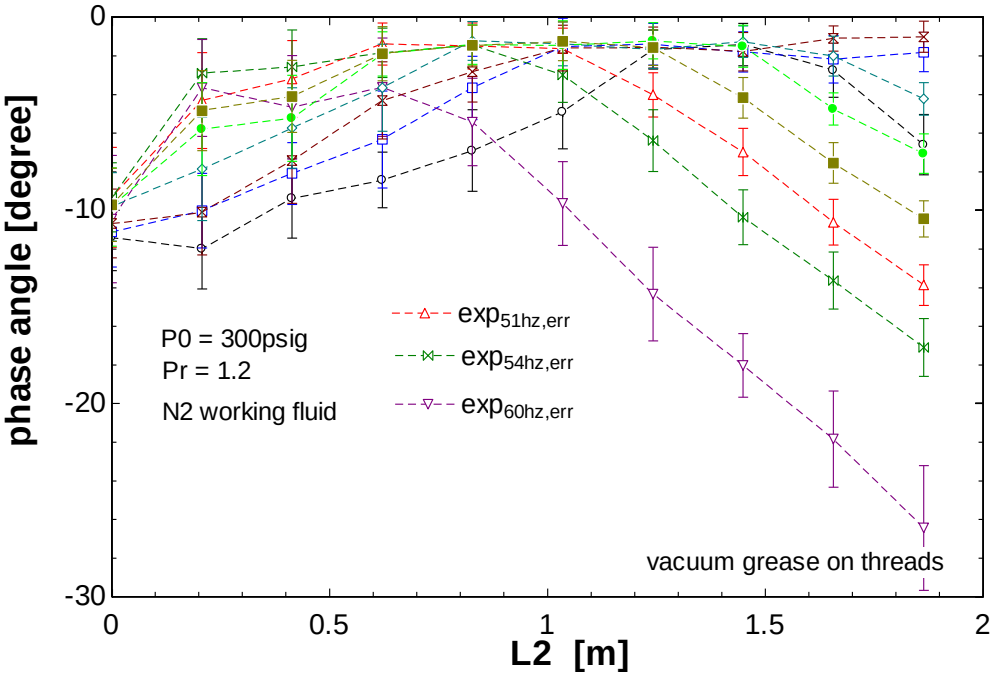

FIGURE 4-18 Phase angle shift at different frequencies from the experimental data

FIGURE 4-18 illustrates the phase angle measured from the experiment. Nitrogen is used as working fluid, with a 300 psig charge pressure. The range of the phase angle is from -2° to -30°. The phase angle changes from -2° to -10° at 30 Hz and from -2° to -30° at 60 Hz. The higher the frequency, the larger the phase angle changes when turning the adjustable inertance tube. However, the phase angle shift detected by the experiment does not uniformly agree with the Distributed Component Model. Presumably several leaks between the two threads of the screws still exist, deteriorating the performance of the adjustable inertance tube phase angle shift ability.

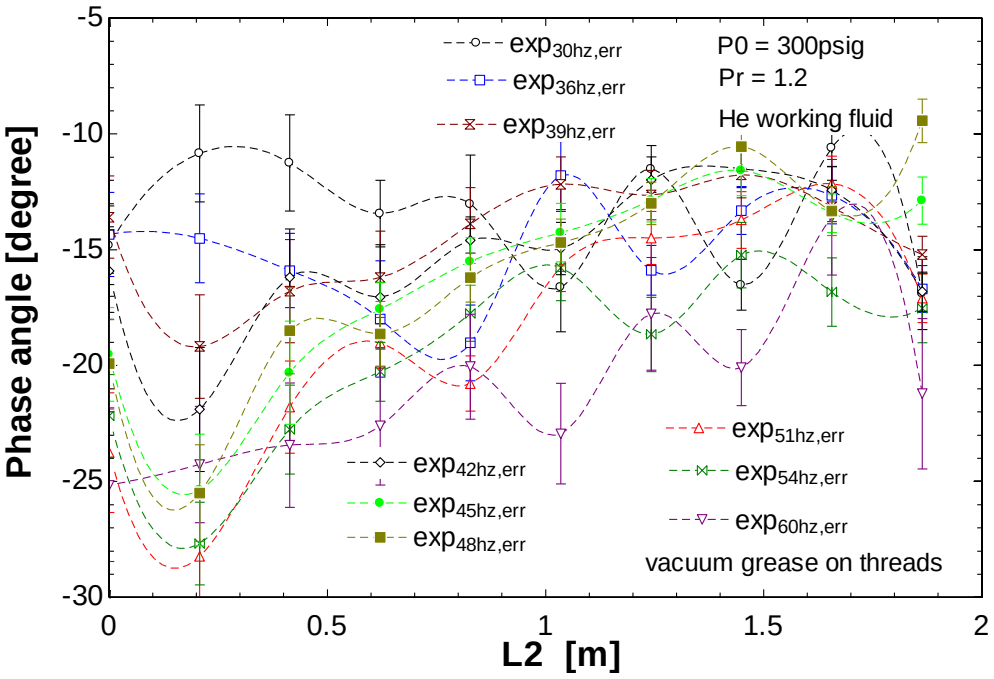

FIGURE 4-19 Phase angle shift at different frequencies by using Helium

FIGURE 4-19 demonstrates the phase angle measured in the experiment when using helium as the working fluid, at a 300 psig charge pressure. The measured phase angle shift when using helium does not change a lot by increasing the length and

diameter of the adjustable inertance tube. At 30 Hz, the phase stays at -10° when changing the length. If the frequency increases to 60 Hz, the phase angle increases from -30° to -10° as the total length of the inertance tube increases. Since the viscosity of helium is 1.993e-5 kg/m-s, the measured data from helium results in a larger uncertainty, which is also shown in FIGURE 4-19.

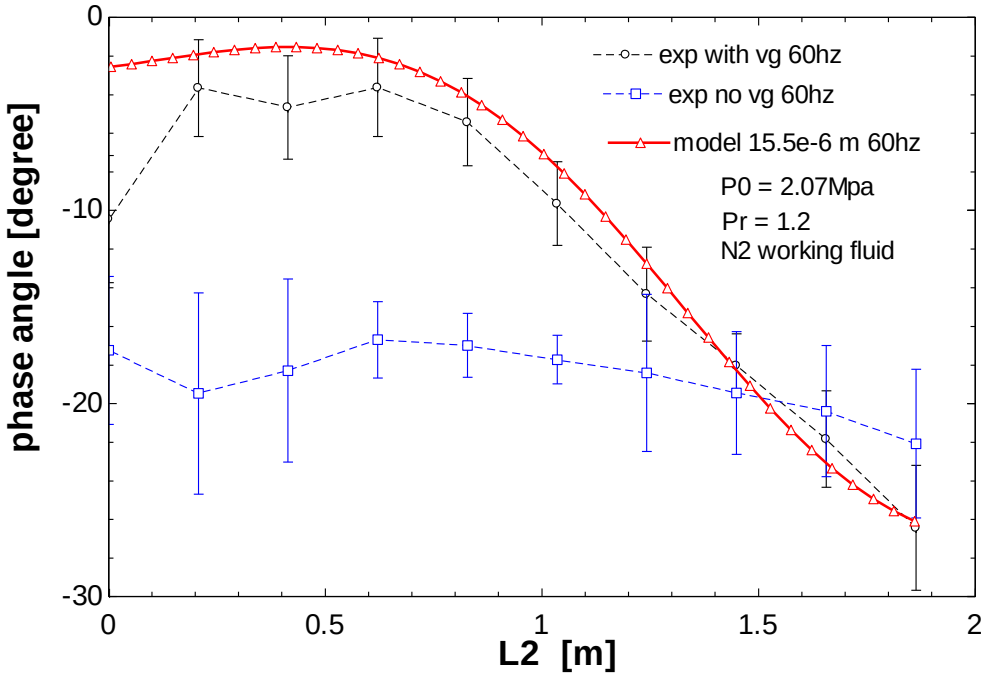

FIGURE 4-20 Phase angle shifts with length of inertance tube at 60 Hz

FIGURE 4-20 shows the measured phase angle as a function of the position of the outer screw when the device is operated at 60 Hz with nitrogen as the working fluid. There are three curves shown in FIGURE 4-20. The triangle symbols on the solid line indicate the phase angle predicted by the modified distributed component model under the conditions with a clearance gap of 15.5 μm in the calculation. The phase angle increases from -1.5° to -1° and then decreases to -25° as the length of the large diameter inertance tube increases from 0 m to 1.86 m; almost a 24° phase angle change. The

rectangular symbols on a dashed line illustrate the measured phase angle during our initial testing. Because of the leak between the threads, the phase angle between the mass flow and pressure at the inlet of the inertance tube stays almost constant and equal to approximately -20°. It is easy to imagine that the nitrogen flow essentially shortcuts to the reservoir directly after entering the inertance tube. Therefore, no matter what position the outer screw is in, the phase angle remains constant.

The experimental data with vacuum grease on the threads corresponds to the circle symbols on the dashed line in FIGURE 4-22; these experimental measurements agree with the MDCM predictions quite well both in magnitude and trend, The phase angle increases from -10° to -5° and then decreases to -25° as the outer screw is rotated from its bottommost position to its topmost position. The uncertainties shown in the measured phase angle are calculated from the standard deviation in several phase angle measurements. Each pressure wave was measured at least 40 times allowing the phase angle shift to be calculated 40 times at each condition.

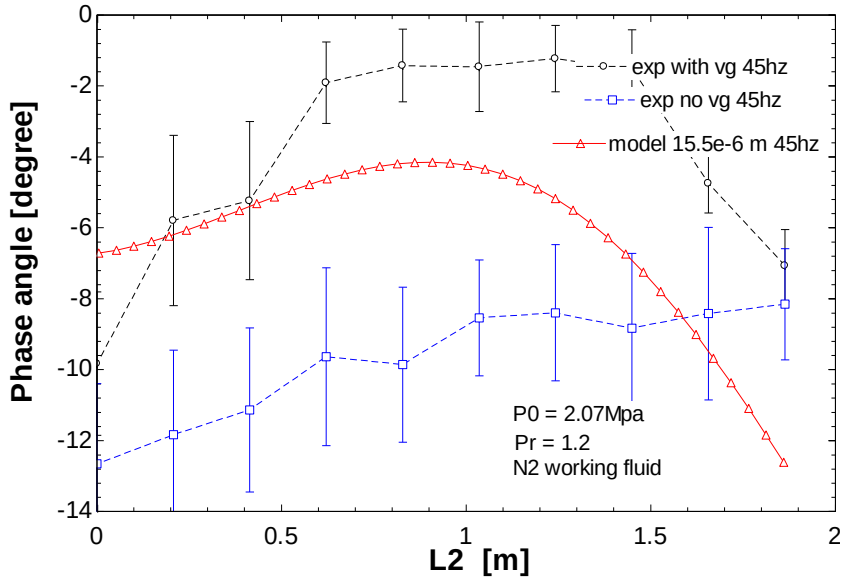

FIGURE 4-21 Phase angle shifts with the length of inertance tube at 45 Hz

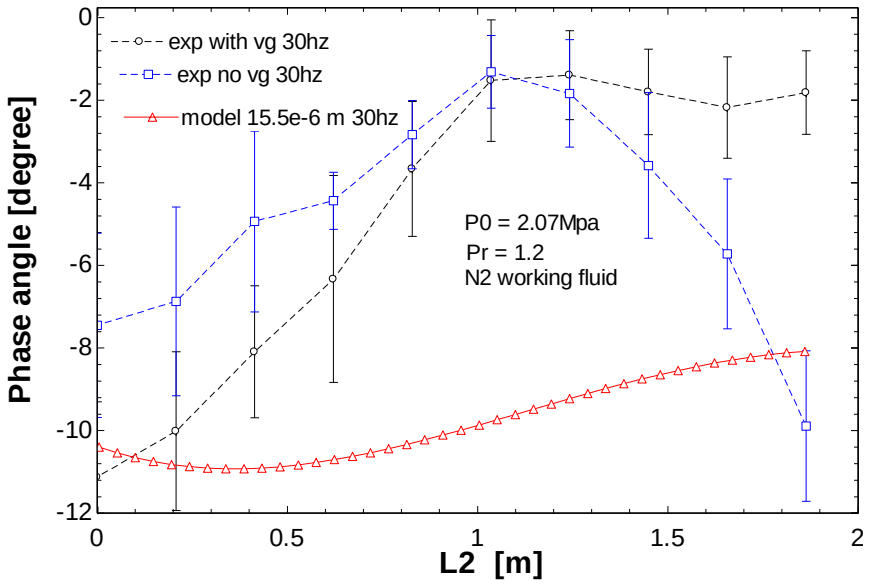

FIGURE 4-22 Phase angle shifts with the length of inertance tube at 30 Hz

FIGURE 4-21 and FIGURE 4-22 show the same information at 45 Hz and 30 Hz. For the 45 Hz case, there is still an 8° phase angle shift predicted by the modified

distributed component model (triangle solid curve), and the vacuum grease experimental data (circle dash curve) shows the same trend. The data without vacuum grease again does not match the calculated phase angle shift because of the huge leak between the threads. At 30 Hz (and lower frequencies), the discrepancies between the simulation and test become large and neither simulation nor experiment show a substantial phase shift.

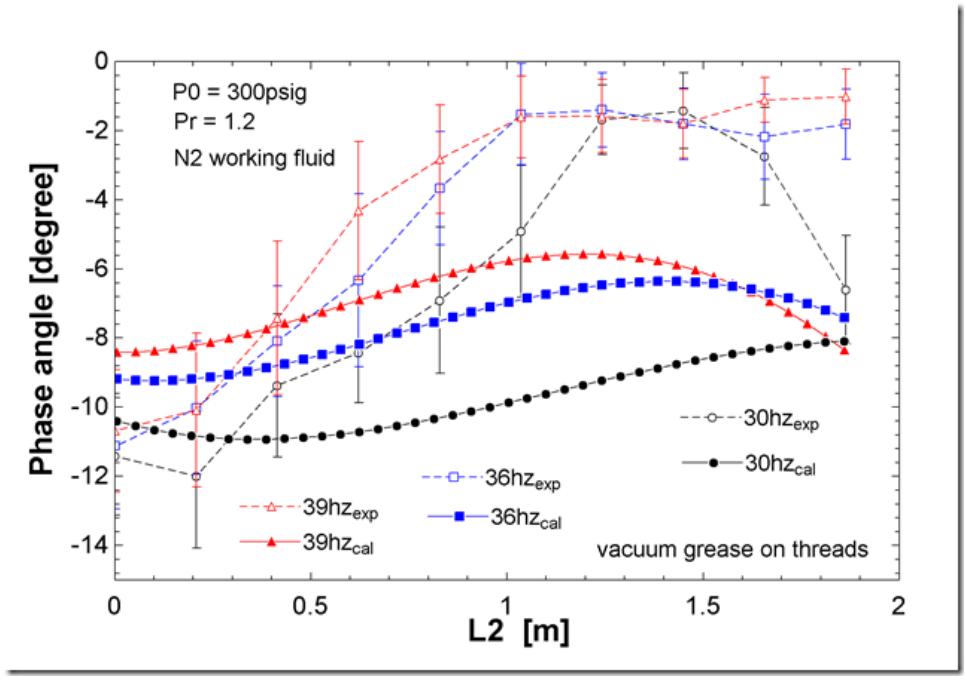

FIGURE 4-23 Phase angle shifts with the length of inertance tube at 30 Hz

FIGURE 4-23 compares the vacuum grease data with the model prediction at lower frequencies. In the experiments, the frequency was increased from 30 Hz to 60 Hz, every 3 Hz interval. The phase angle does not change much as the length of the large diameter inertance tube increases from 0 m to 1.8 m both from distributed component model prediction and from the experiment. However, in the 30 Hz frequency range, both

model and experimental data show the same trend for the change of the phase angle as a function of the inertance tube length.

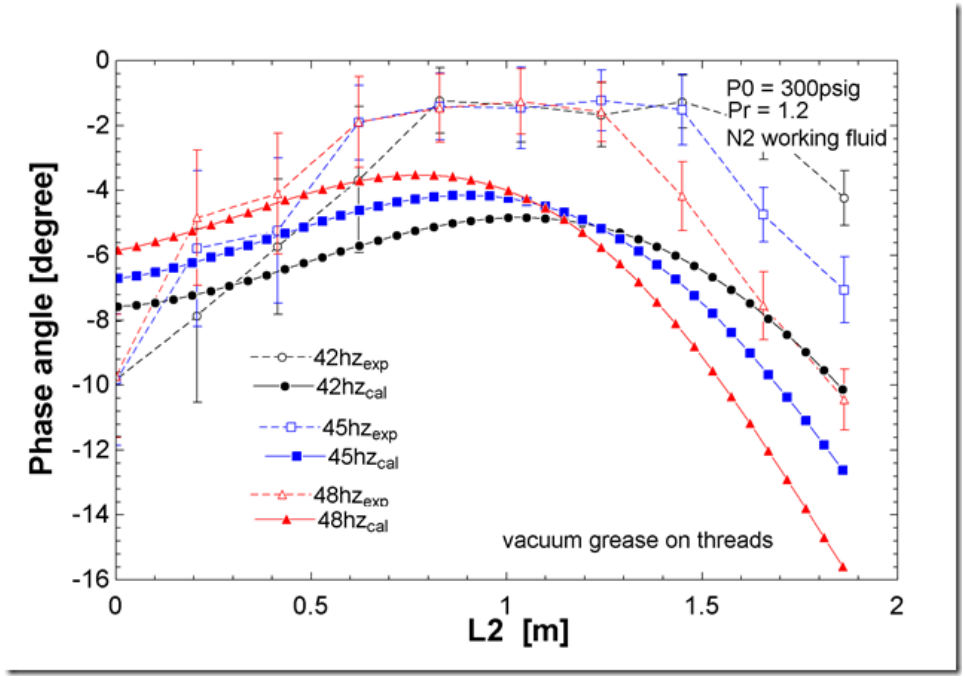

FIGURE 4-24 Phase angle shifts with the length of inertance tube at 30 Hz

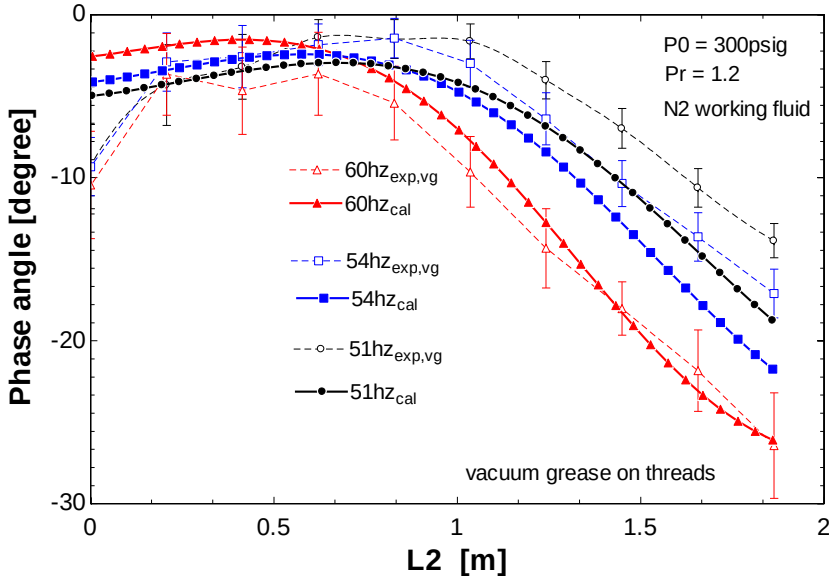

FIGURE 4-25 Phase angle shifts with the length of inertance tube at 30 Hz

FIGURE 4-24 and FIGURE 4-25 also shows the phase angle shift as the outer screw is rotated from its bottommost position to the topmost position at different frequencies. In FIGURE 4-24, the operation frequencies are in the 40 Hz range. The phase angle varies from -6^0 to -16^0 both from the modified model prediction and experiments. At the higher frequencies such as 54 Hz and 60 Hz shown in FIGURE 4-25, both the modified model and experimental measurements display a large phase angle shift, indicating that the adjustable inertance tube has a large phase shifting potential and could be used to optimize the phase angle for the pulse tube cryocooler.

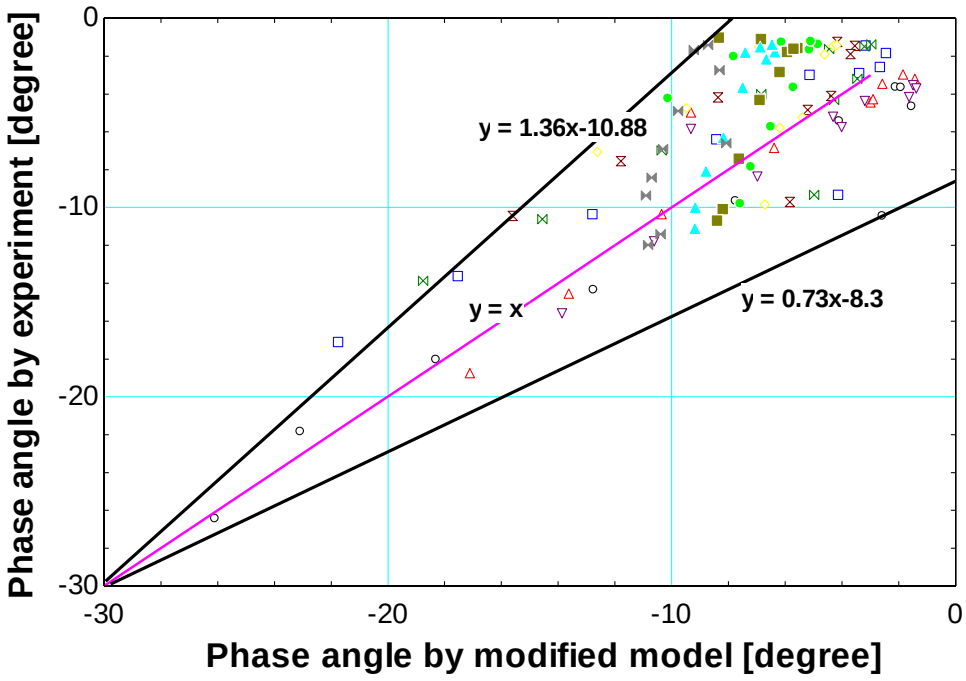

FIGURE 4-26 Phase angle shift performance using helium at 30 Hz

The measured phase angle is also compared with the model prediction, which is shown in FIGURE 4-26. Here, the phase angle predicted by the model at different frequencies is used as a reference, and the phase angle measured from the experiment is compared with the reference. From FIGURE 4-26, the measured phase angle is around 36% higher or 27% lower than the theory. The deviation of the measured phase angle from the model is also affected by the experimental uncertainty from the pressure transducer and from the NI DAQ. The noise from the pressure transducer is generated by the interference from the magnetic field of the linear compressor.

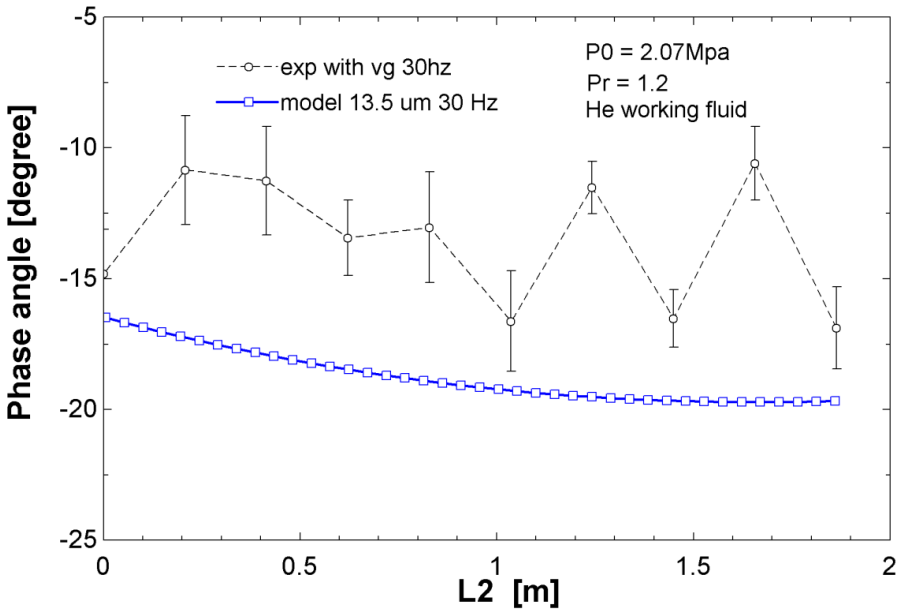

FIGURE 4-27 Phase angle shift performance using helium at 30 Hz

Helium is used as working fluid in some of the adjustable inertance tube experiments. FIGURE 4-27 illustrates the phase angle change with the length of the large

diameter inertance tube at 30 Hz when using helium. From the plot, both modified model and the experimental data predict a relatively small phase angle variation at 30 Hz. Due to the small viscosity of helium, the uncertainty measured by the helium is relatively large from the experiment, but the trend of the phase angle variation is very close to the model prediction.

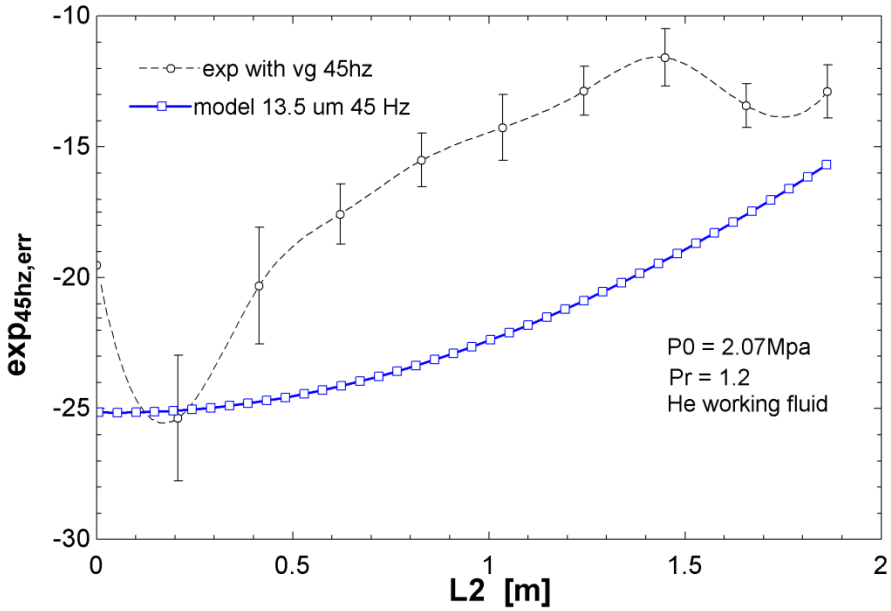

FIGURE 4-28 Phase angle shift performance using helium at 45 Hz

FIGURE 4-28 and FIGURE 4-29 demonstrate the phase angle shift performance of the adjustable inertance tube when using helium as the working fluid at 45 Hz and 60 Hz, respectively. The discrepancy between experimental data and numerical model calculation is around 10° at 45 Hz, as shown in FIGURE 4-28. As the length of the large diameter inertance tube increases, both the model and experimental data shows a 10°

phase angle change. The operation frequency is 60 Hz in FIGURE 4-29. The model predicts a 25° phase change while the experimental data only displays a 10° phase shift.

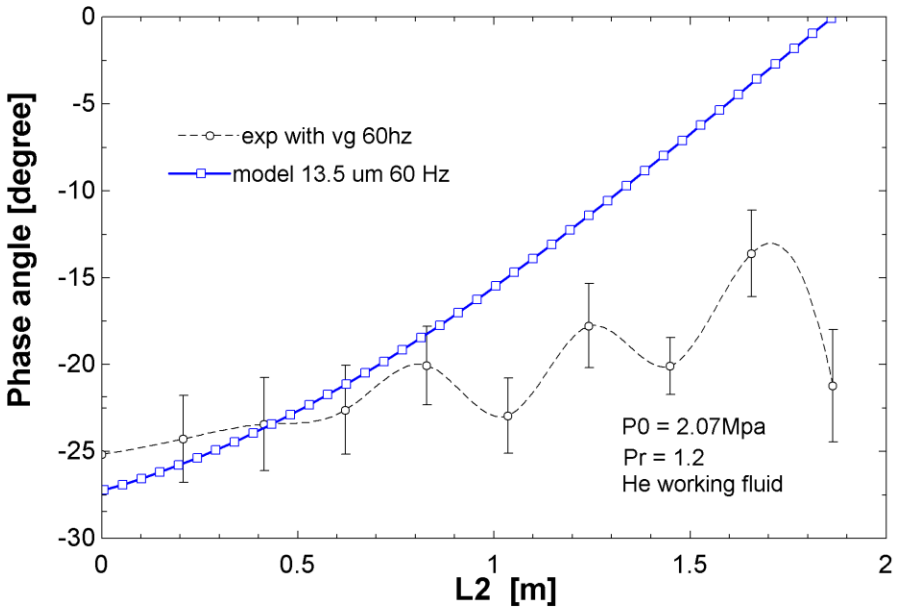

FIGURE 4-29 Phase angle shift performance using helium at 60 Hz

4.2.4 Acoustic power comparison

Acoustic power is also another important parameter for the design of an adjustable inertance tube. Therefore, the comparison of acoustic power between model and experiment is also discussed in this section. In the experiment, the adjustable inertance tube and the reservoir produce an impedance load for the linear compressor. During the experiment, the acoustic power transforms into heat both inside the inertance tube and reservoir and is taken away via the fin heat exchanger around the reservoir. The

mass flow rate, pressure oscillation and volumetric flow rate are all sinusoidal waves, therefore, the acoustic power can be determined using the equation below:

$$W_{ac} = \frac{1}{2}|P_{d2}||\dot{V}|\cos\theta \tag{4-14}$$

Here, P_{d2} is the pressure amplitude from the inlet of the inertance tube, that is from pressure transducer 2 in the experiment. $\dot{V}$ is the volumetric flow rate at the entrance of the inertance tube, and θ is the phase angle difference between the pressure and volumetric flow rate, since they are both sinusoidal waves. The mass flow rate at the inlet of the adjustable inertance tube can be approximately calculated as[46]:

$$\dot{m}_{in} = 2\pi f \frac{P_{d2}V_{res}}{\gamma R T_0}\cos 2\pi ft \tag{4-15}$$

Here P_{d2} is the pressure amplitude from pressure transducer 2 mounted at the other end of the mass flow meter. V_{res} is the volume of the reservoir, T_0 is the temperature at the inertance tube inlet, and f is the operating frequency of the linear compressor. By substituting equation 4-15 into equation 4-14, therefore, equation 4-14 can be rewritten as:

$$W_{ac} = \frac{1}{2}|P_{d2}|\left|\frac{\dot{m}_{in}RT_0}{P_0}\right|\cos\theta = \frac{1}{2}|P_{d2}|\left|\frac{2\pi f P_{d2}V_{res}T_0}{P_0\gamma T_{res}}\right|\cos\theta \tag{4-16}$$

T_0 is the temperature at the inlet of the reservoir, which is approximately equal to room temperature, and γ is the specific heat ratio of working fluid. The acoustic power from the modified distributed component model could be determined directly using equation 4-14

since the pressure amplitude, volumetric flow rate and phase angle have already been determined through the calculation of the modified distributed component model.

FIGURE 4-30 shows the model calculation of the acoustic power consumption by the adjustable inertance tube. The variation of the acoustic power changes from 310 W to 210 W, as the outer screw moves from its bottommost position to its topmost position. The pressure ratio is constant as 1.2 at the pulse tube end of the inertance tube. If the operation frequency is 60 Hz, the acoustic power will first increase and then decrease as the length of the large diameter inertance tube increases. The variation of the acoustic power is caused by the impedance change of the load, which verifies the effectiveness of the impedance shifting ability of the threaded adjustable inertance tube.

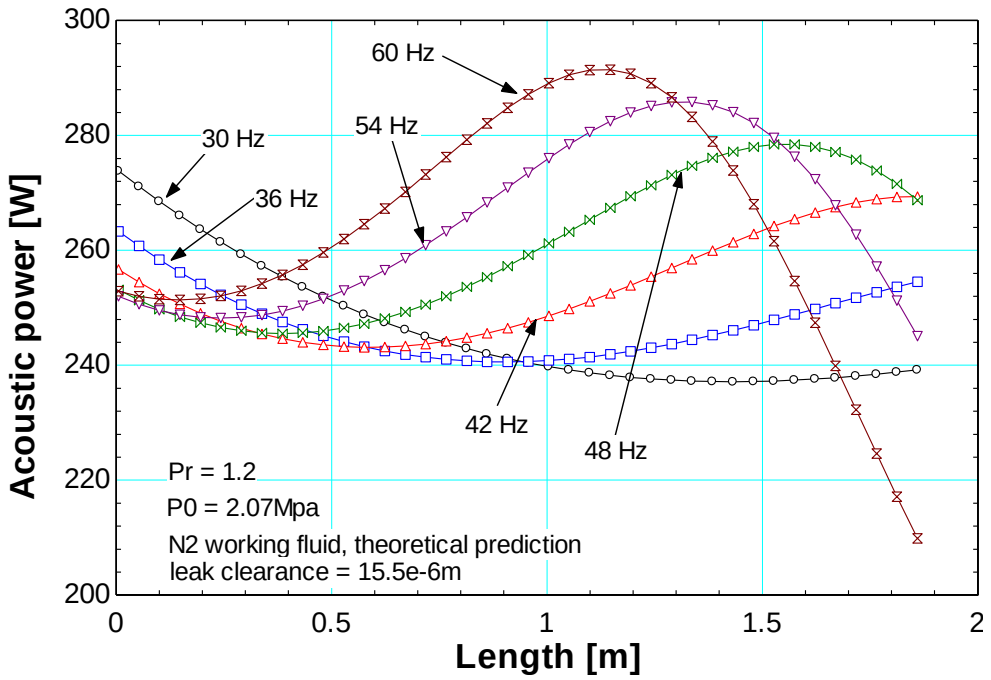

FIGURE 4-30 Calculated acoustic power change vs. length of the large inertance tube

FIGURE 4-31 illustrates the acoustic power consumption by the experiment at different operation frequencies. The acoustic power varies between 245 W to 280 W. The acoustic power stays almost constant in the 30 Hz to 40 Hz range and decreases a little bit in the 60 Hz range. The behavior is not as the same as predicted by the model.

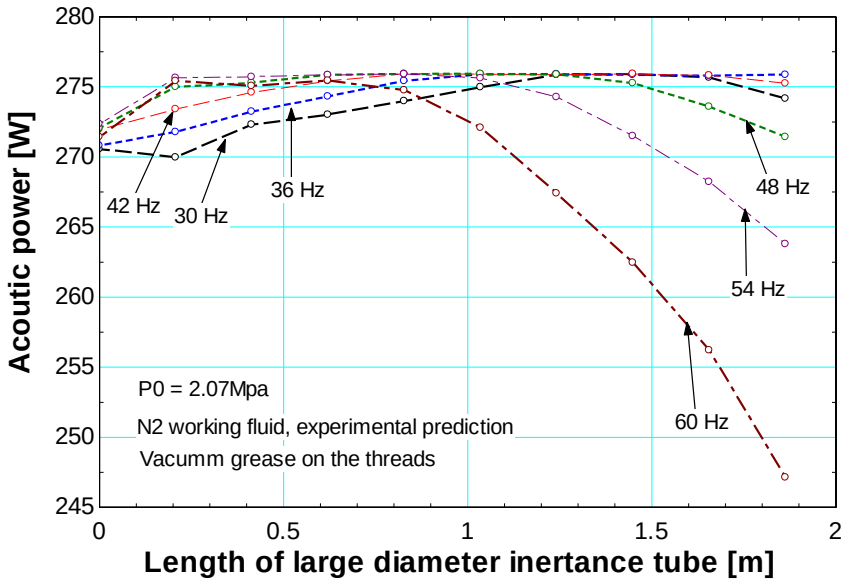

FIGURE 4-31 Measured acoustic power change vs. length of the large inertance tube

FIGURE 4-32 compares the measured acoustic power and calculated acoustic power in the 60 Hz range. The measured acoustic power does not follow the behavior of the model, but the values are in the same range.

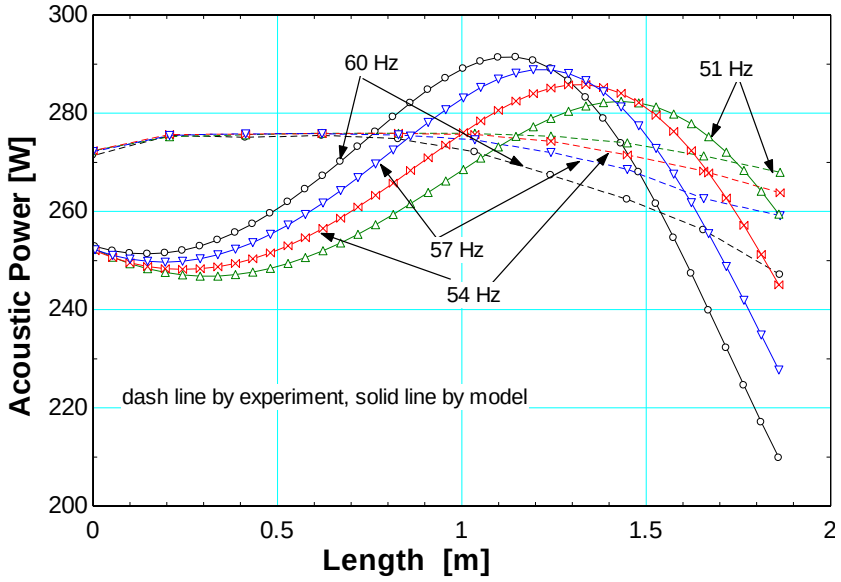

FIGURE 4-32 Comparison of acoustic power shift determined by the model and experiment

4.3 Adjustable Inertance Tube Design Approach

The above results from both the experimental measurements with the threaded adjustable inertance tube and the model, demonstrate the ability of the threaded adjustable inertance tube to shift the phase angle while maintaining a relatively constant acoustic power. Based on the reasonable agreement between the measurements and theory, one may justifiably use the modified distributed component model as a design tool to determine the dimensions of other adjustable inertance tubes. The following paragraphs describe the necessary steps for such a design exercise.

The distributed component modeled was originally written to calculate acoustic power and phase angle for an inertance tube of specified length and diameter. However, in many cases, the design of an inertance tube begins with desired parameters such as

phase angle and acoustic power needed for the pulse tube operation. The steps and procedure to generate a map defining the range of diameter and length necessary for a desired range of acoustic power and phase shift are shown in the following block diagram. A detailed version of the Matlab code for the Distributed Component Model is provided in the appendix section 7.2.

To begin, the user will input the range of acoustic power (Wac) and phase angle (theta) values into the section of code named 'Run_DCMLW_12.' This section in turn will call the routine 'findL2' that determines the length and diameter corresponding to the values of Wac and theta. The routine 'findL2' calls another routine named 'ftheta2' that determines the error between the desired theta and a calculated value of theta. The calculated value of theta is gathered from the routine named 'DCMLW_12.' In addition 'DCMLW_12 determines a value for D.

In order for DCMLW_12 to be able to determine values for D and theta, it relies on three other nested subroutines. These subroutines, from the outer to the inner layers are respectively named 'findD', 'fWac', and 'DCM_12.'

In FIGURE 4-33, the acoustic power and phase angle are set to be an input parameter, after calling different functions, length and diameter are calculated as output diameter. Each of the function in FIGURE 4-33 is listed in the appendix 7.2.

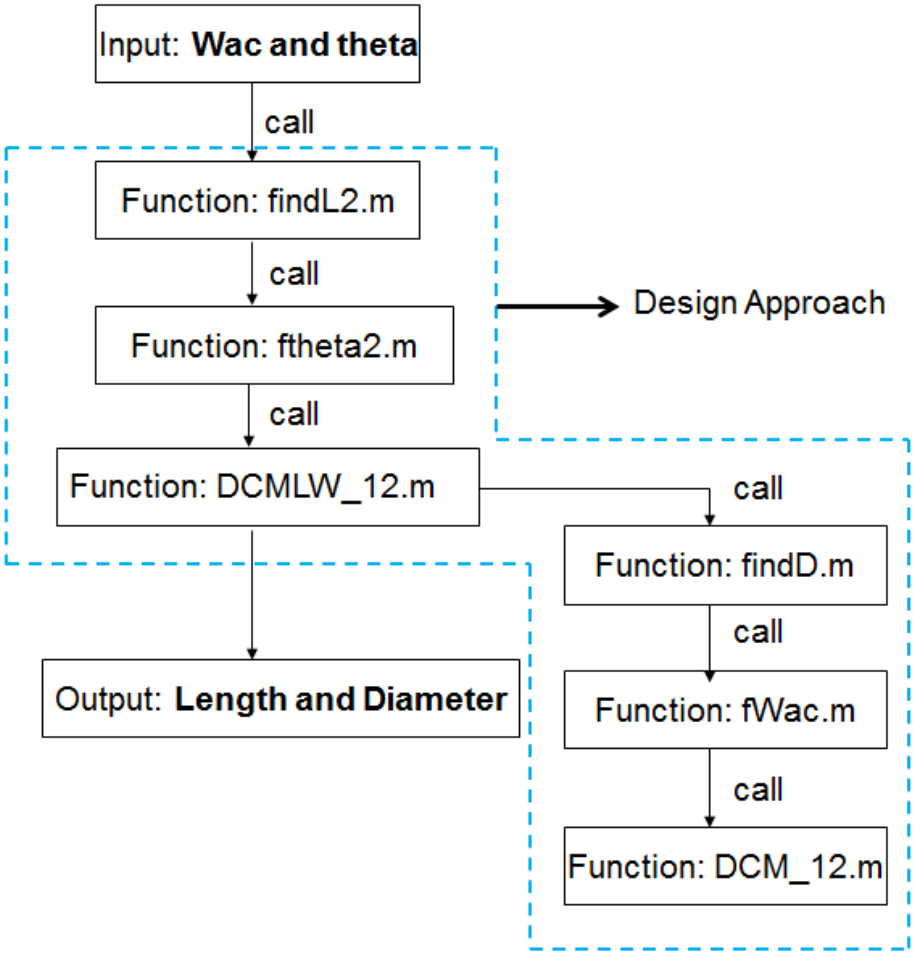

FIGURE 4-33 Flow chart of using acoustic power and phase angle to determine the length and diameter

A result of the subroutines 'findD', 'fWac', and 'DCM_12' called by DCMWL_12 in which values of length and acoustic power are used to calculate the phase angle and diameter is shown in Figure 4-34. In the calculation, the length ranges from 1 m to 2.5 m and the acoustic power changes from 100 W to 2500 W.

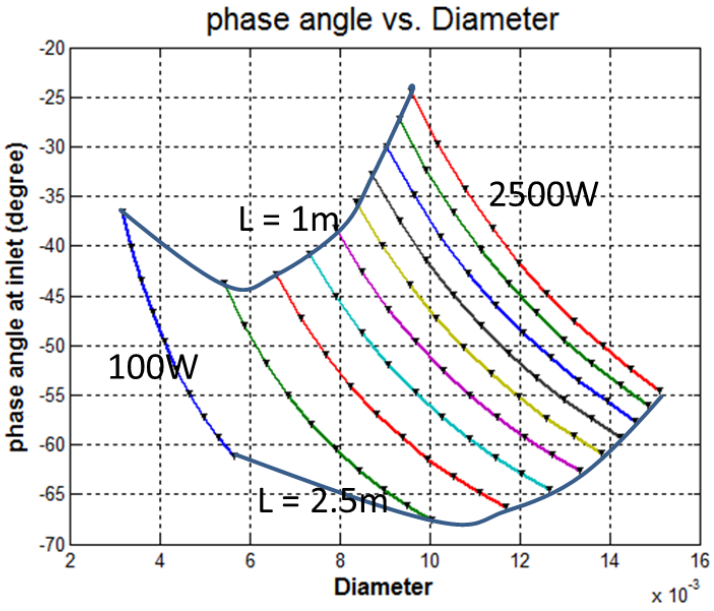

FIGURE 4-34 Contour plots of setting length and acoustic power as input parameters to find the diameter and phase angle

From FIGURE 4-34, the diameter and phase angle can be easily be found if length and acoustic power are given as the design parameters. For example, with a length of 1 m and acoustic power of 100 W, the diameter is 3mm and the phase angle is -36°.

The contour plots in FIGURE 4-35 show the calculation results from using the phase angle and acoustic power to find the specific diameter and length of an inertance tube. Typically, the phase angle at the inlet of the inertance tube ranges between -30° and -60° and the acoustic power ranges from 100W to 1500W. The calculation diameter ranges from 3mm to 14mm and length varies from 0.6m to 2.4m, as shown in FIGURE 4-35.

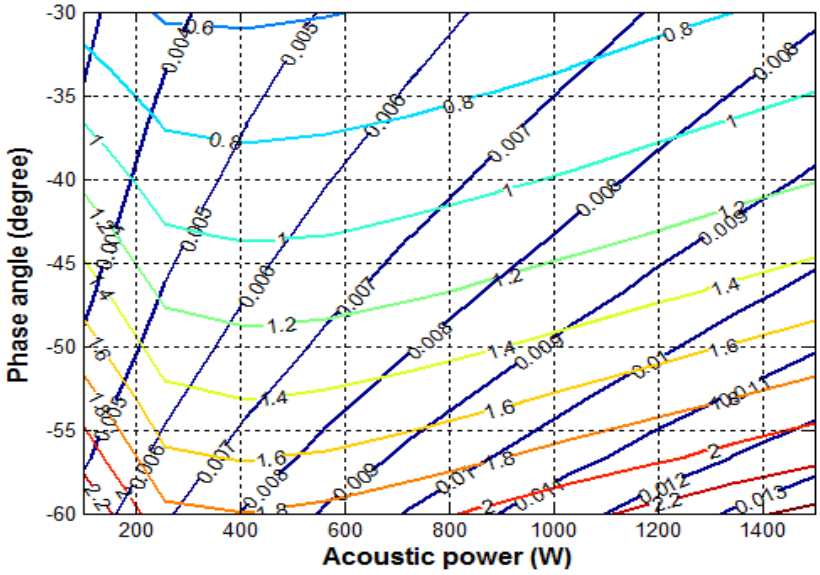

FIGURE 4-35 Contour plots of setting phase angle and acoustic power as input parameters to find length and diameter

In order to verify the above method, the function "DCM_12.m" has also been used with diameter and length as input parameter to directly calculate associated values of acoustic power and phase angles. The results are shown in a separate contour plot shown in FIGURE 4-36. The left figure in FIGURE 4-36 is the original plot generated by the function "DCM_12.m", which shows the entire range of the acoustic power and phase angle with the specific diameter and length. The right hand plot shows an enlarged region of the plot on the left for the acoustic power range from 100W to 1000W and phase angle range from -60° to -30°. The right figure is exactly the same as FIGURE 4-35, which verifies the effectiveness of the design method.

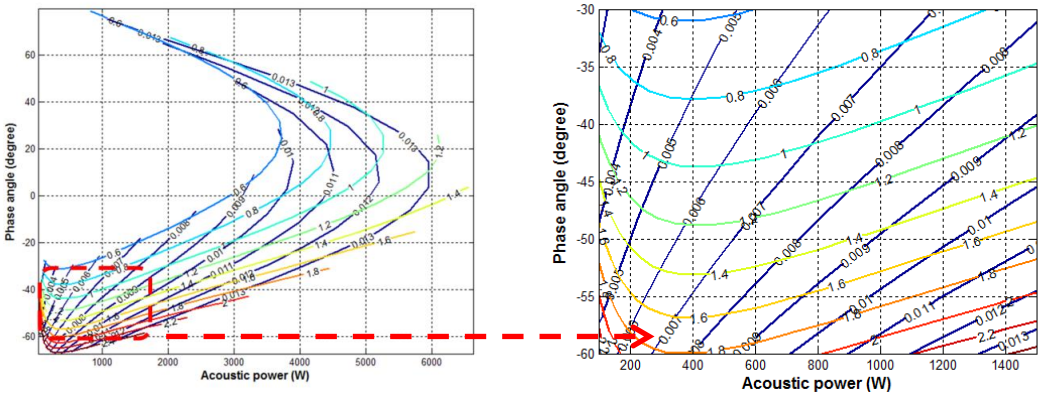

FIGURE 4-36 Verification of inertance tube design approach

4.4 Uncertainty analysis

Two sources of uncertainties are discussed in this section, the uncertainty from measuring devices and the uncertainty from the statistics of a sample of measurements. The uncertainty based on the statistics of a sample of measurements can be determined after the measurement. The uncertainty from the measuring devices can be determined before the measurement. Therefore, the total uncertainty can be computed using the following method:

$$U_{total} = \sqrt{U_{pre}^2 + U_{act}^2} \tag{4-10}$$

Where U_{pre} represents uncertainty from statistics of a sample of measurements and U_{act} stands for uncertainty from measuring device. U_{pre} can be calculated by the result of standard deviation from the experimental data S_x multiplies the coefficient from the Student's distribution t_{95}.

$$U_{pre} = S_x \cdot t_{95} \tag{4-11}$$

Here the standard deviation can be found using equation 4-12:

$$S_x = \sqrt{\frac{\sum (P_{curve} - P_{meas})^2}{N^2}} \tag{4-12}$$

Where P_{curve} is data obtained from the calibration process, and P_{meas} is the measured data from the experiment. Here demonstrates a specific example about the pressure uncertainty analysis in our previous linear adjustable inertance tube experiment.

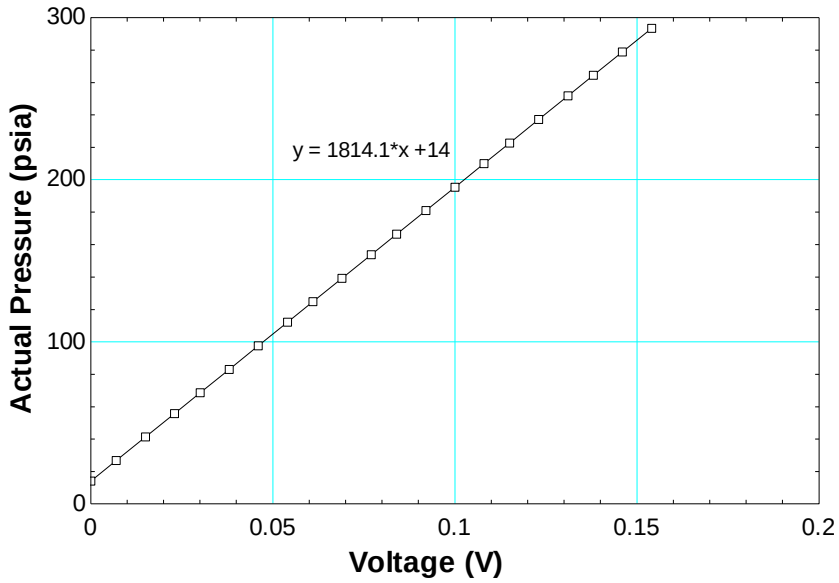

FIGURE 4-37 Calibration curve for Endevco pressure transducer

FIGURE 4-37 shows the calibration curve of pressure transduce in the previous experiment. Here we measure the voltage of the pressure transducer and convert it into pressure P_{curve}. The equation of P_{curve} is also shown on FIGURE 4-37. The P_{meas} can be determined by the following equation:

$$P_{meas} = (V_{meas} - V_1) \cdot \frac{Span_{pressure}}{Span_{volt}} \tag{4-13}$$

Where V_{meas} is the voltage measure during the calibration process, V_1 is the first voltage data from the measurement. $Span_{pressure}$ is the pressure range and $Span_{volt}$ is the voltage range in the measurement.

The accuracy uncertainties can be calculated using the following equation:

$$U_{act} = \frac{Span_{DAQ}}{2^{N_{DAQ}}} \cdot \frac{Span_{pressure}}{Span_{vol}} \tag{4-14}$$

Where $Span_{DAQ}$ is the voltage range of my DAQ device, and N_{DAQ} is the analog input digit of the DAQ device. In the previous experiment $Span_{DAQ}$ is 20 V, and N_{DAQ} is 14. Therefore, we can get the actual uncertainty and precision uncertainty by using these equations. Here is an example of how to determine the pressure uncertainty from the specific pressure transducer. The U_{pre} for the pressure transducer 1 measurement in the experiment is about 262.61 Pa and U_{act} for the measurement DAQ device is about 3825.66 Pa. Thus, the total uncertainty is about 3834.66 Pa, which is only 1.7% of the pressure amplitude 230000 Pa by the readings of the pressure transducer itself.

Above is the way to determine the pressure uncertainty, the phase angle uncertainty also needs to be figured out by using the pressure data. The phase angle measurement uncertainty is determined by the standard deviation of the multiple pressure cycles. The pressure measurement is stable enough so that the phase could be determined.

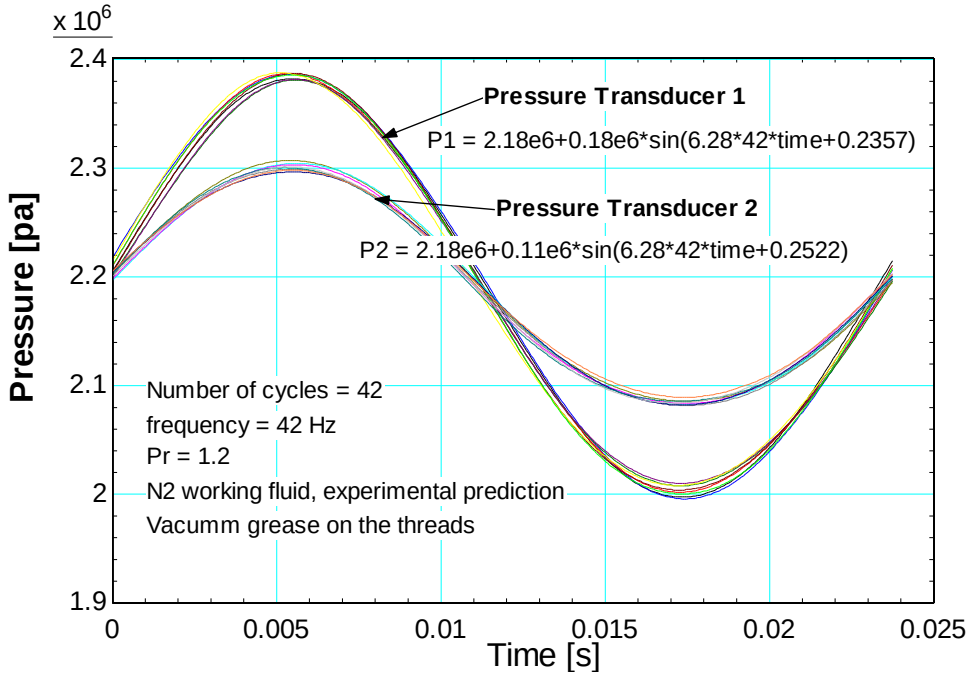

FIGURE 4-38 Measured pressure at 42 Hz for 42 cycles

FIGURE 4-38 shows 42 different pressure cycles captured by pressure transducer 1 and pressure transducer 2 mounted on each side of mass flow meter. The pressure measurement is relatively stable so that they almost overlap on each other, with only a small variation. This precise pressure measurement ensures the phase angle prediction by the pressure data is repeatable and stable for different diameters and lengths of the adjustable inertance tube.

For each of the pressure measurement, there are 30 to 60 repeatable pressure cycles, therefore, the random errors of the phase angle could be determined through the following method. In FIGURE 4-39, the triangle symbols indicate one cycle of pressure data from pressure transducer 1, the square symbols represent one cycle of pressure transducer 2 data, and the circle symbols are pressure different between pressure transducer 1 and pressure transducer 2. By applying the curve fit function for each of the

pressures, three curve fit equations are labeled on the figure. Thus, the phase angle difference between mass flow and pressure wave at the hot end of pulse tube could be determined through the phase angle of P1-P2 and P2 curve fit equations. Specifically, the phase angle on FIGURE 4-39 is (0.1272-0.2522)/3.14*180 = -7.16°.

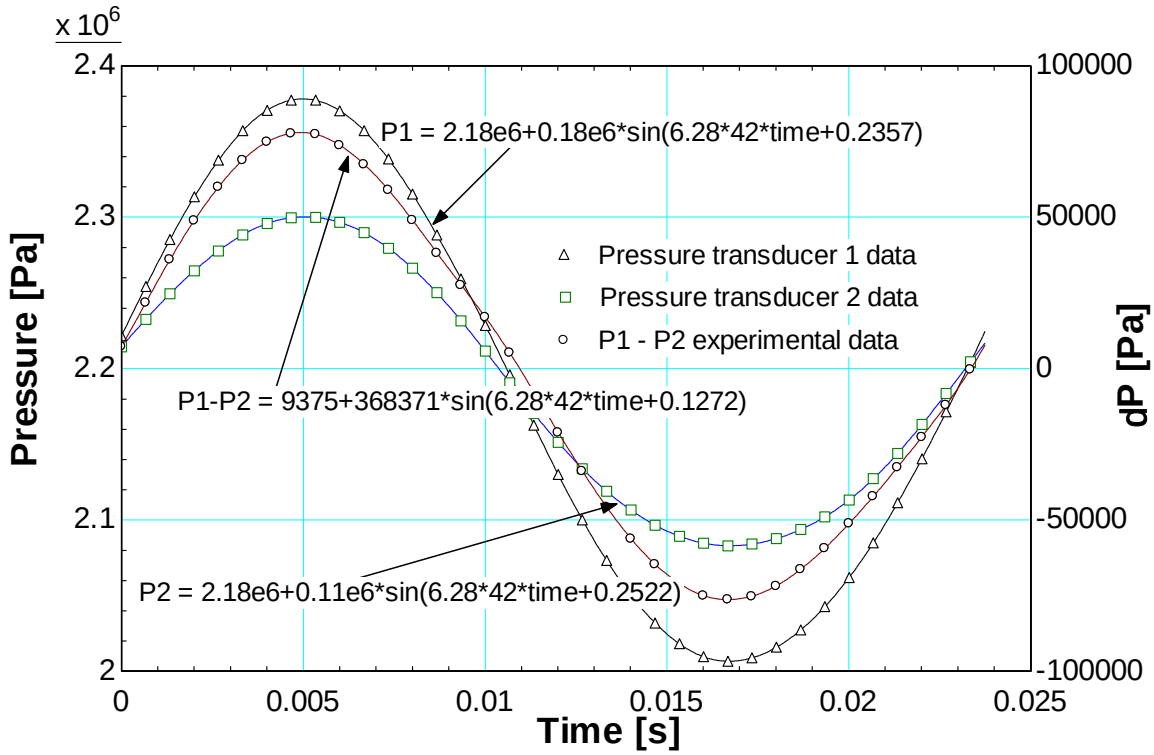

FIGURE 4-39 Phase angle difference prediction method

For the phase angle at 42 Hz, there are 42 cycles of pressure data resulting 42 slightly different phase angles. Therefore, the average phase angle could be determined by the equation below:

$$\phi_{ave} = \frac{\sum_{i=1}^{N} \phi_i}{N} \tag{4-15}$$

The uncertainty in the phase angle measurement is:

$$\Delta\phi = \sigma = \sqrt{\frac{\sum_{i=1}^{N}(\phi_i - \phi_{ave})^2}{N}} \tag{4-16}$$

And the uncertainty in the mean phase angle is:

$$\Delta\phi_{ave} = \frac{\sigma}{\sqrt{N}} \tag{4-17}$$

Therefore, the phase angle could be calculated via:

$$\phi_m = \phi_{ave} \pm \Delta\phi_{ave} \tag{4-18}$$

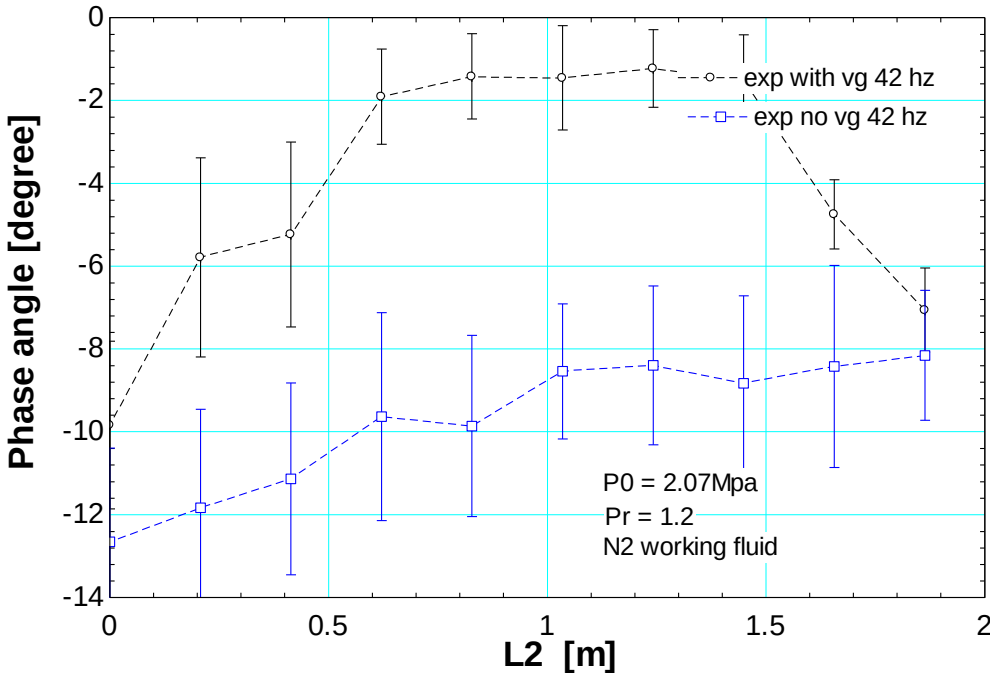

FIGURE 4-40 Measured phase angle uncertainty

The measured phase angle uncertainty at 42 Hz is shown in FIGURE 4-40. The phase angle between the mass flow rate and pressure oscillation at the inlet of the inertance tube was detected via the two pressure transducers across the mass flow meter. There are at least 42 cycles of pressure oscillation measured from these two pressure transducers, therefore, 42 phase angles are detected from these pressure measurements, and the uncertainties of these 42 phase angles at different inertance tube position are

calculated and depicted in the FIGURE 4-40. From FIGURE 4-40, the uncertainty is around 1 ° or 2 ° for each of the phase angle at different length of the inertance tube.

5 Results Discussion and Future Work

The cylindrical threaded adjustable inertance tube was designed, fabricated, and tested in the lab. The experimental measurements closely follow the modified distributed component model prediction, and consequently characterize the phase angle shift performance of the adjustable inertance tube. Due to the configuration of the cylindrical threaded adjustable inertance tube, the adjustable inertance tube channel is enclosed by the threads of the two screws and the leaks between the screws deteriorate the phase angle shift performance. Various possibilities to eliminate the leak have been considered and could be realized with modifications on the next version of this device. Some recommendations are listed below for the future advice.

5.1 Recommendations for the cylindrical threaded inertance tube

As shown above, the presence of the leaks between the threads of the cylindrical adjustable inertance tube limited its phase angle shift ability. Several improvements can be implemented to avoid the leaks inherent in the device, such as increasing the engagement length of the two screws, and generating two inertance tubes in parallel.

In the first option, one may decrease the magnitude of the leaks by increasing the engagement length of the two screws. For the threaded adjustable inertance tube, there are two portions of the inertance tube channels, the large diameter passage and the small diameter passage. The engagement length of small diameter channel is longer than that of

the large diameter inertance tube, resulting in smaller leaks through the smaller diameter passage, which is shown in FIGURE 5-1 below. Therefore, if the engagement length of the large diameter inertance tube is big enough to eliminate the leaks via the two screws, it is possible to decrease the leak effects of threaded adjustable inertance tube. However, a deeper engagement length will increase the difficulty in manufacturing the outer screw and also increase the cost of the adjustable inertance tube device.

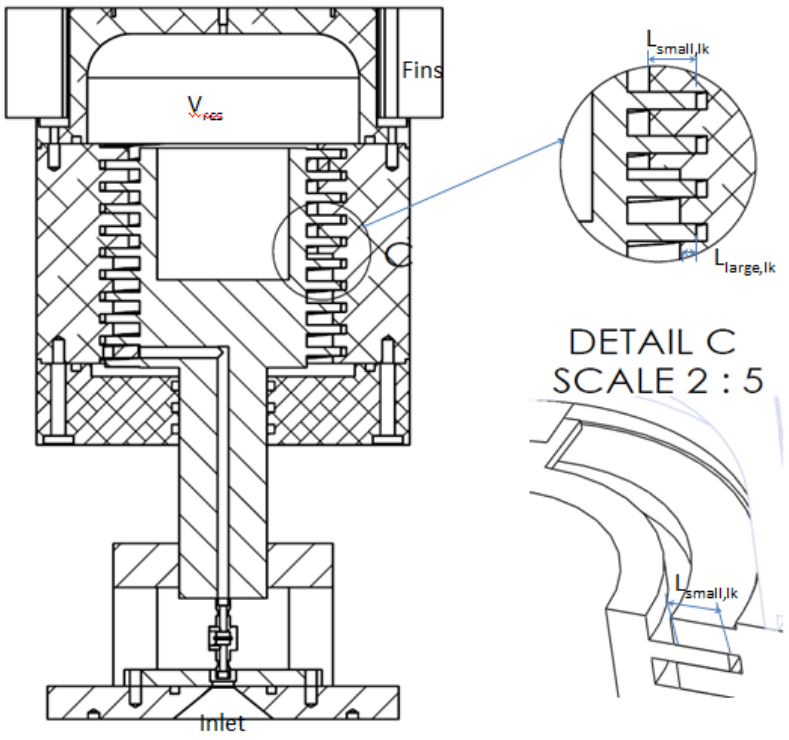

FIGURE 5-1 Detailed engagement length of the large and small leaks

As a second option, one may consider configuring the gas flow to produce two parallel inertance paths. Since there is presently some flow (leak) from the channel at the base of the inner screw to the channel at the base of the outer screw, the second channel

of the inertance tube could be connected to the main channel of the adjustable inertance tube in parallel. In this way, the leak will also be reduced or eliminated by using the two inertance tubes. Including the second inertance tube in parallel will require an additional stop at each end of the second channel formed by the two screws. This modification will also increase the cost of the adjustable inertance tube.

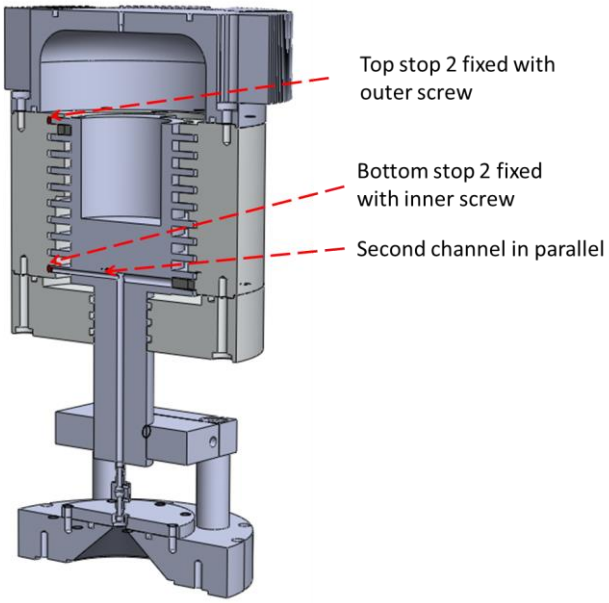

FIGURE 5-2 Configuration of two inertance tube in parallel

FIGURE 5-2 illustrates the geometry of the two-parallel inertance tubes. The working fluid will be separated into two directions after entering the threaded inertance tube. The bottom stop #2 is attached with the inner screw, which constrains the fluid inside the second inertance tube. The top stop #2 is fixed with the outer screw. While the outer screw moves up and down, the top stop #2 travels with the outer screw and the

bottom stop #2 stays at the same location with the inner screw. This configuration reduces the leakage effect from the main inertance tube to the parallel inertance tube.

The phase angle shift ability of the parallel inertance tube can be estimated by the Distributed Component Model. FIGURE 5-3 shows the phase angle shift of a single inertance tube (channel) as a function of the length of the large diameter inertance tube. The phase angle increases from -70° to 38°, as the length of large diameter inertance tube increases from 0 m to 1.86 m. Such a large phase angle shift is certainly desired for an adjustable inertance tube. However, due to the leakage through the inertance tube to the mean pressure reservoir, the phase angle shift is limited with only 0° to -40° as shown above in both calculation and experiment.

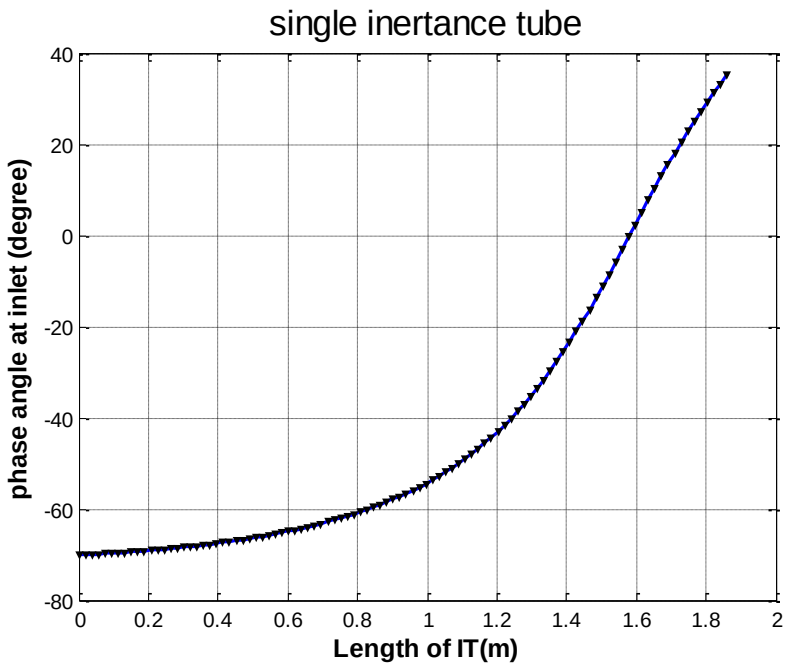

FIGURE 5-3 Phase angle shift ability of single adjustable inertance tube

FIGURE 5-4 demonstrates the phase angle shift ability of the parallel threaded adjustable inertance tube. Since the leak going through the main inertance tube channel to the second inertance tube cannot be ignored, the effective diameter of the parallel inertance tube could be modeled by combining the these two spiral channels together and figure out the hydraulic diameter of the two parallel inertance tubes. The calculated hydraulic diameter of the small inertance tube is 5.8 mm, while the hydraulic diameter of the large inertance tube is 8.5 mm. Therefore, the phase angle shift ability of the parallel inertance tube with the increasing length of the large diameter inertance tube is shown in FIGURE 5-4.

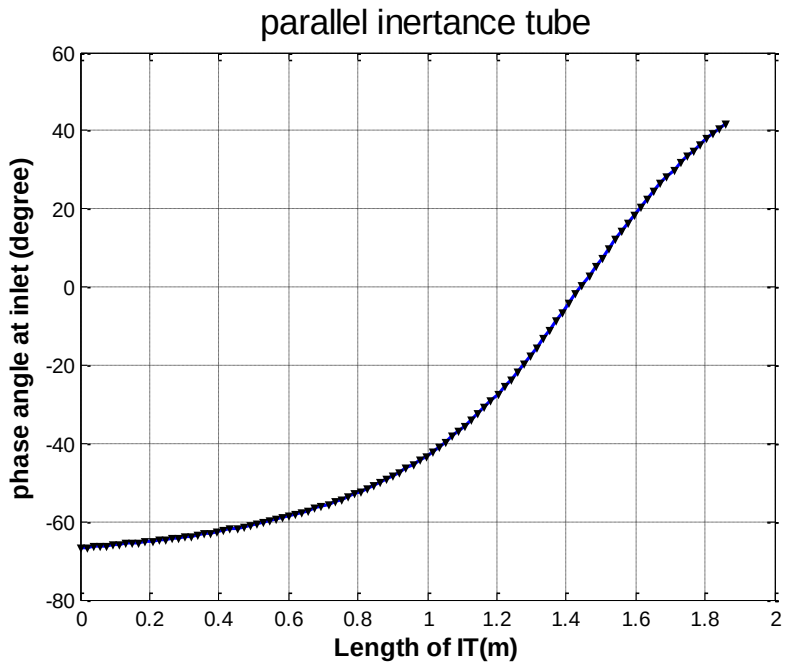

FIGURE 5-4 Phase angle shift ability of parallel adjustable inertance tube

FIGURE 5-4 displays a phase angle shift from -65 ° to 40 ° as the large inertance tube length increases from 0 m to 1.86 m. This phase angle shift is close to the phase angle change of the single inertance tube without any leaks. Therefore, the parallel inertance tube almost has the same phase angle shift ability as that of the single adjustable threaded inertance tube without any leak.

5.2 Summary and Discussion

This work has investigated three possible configurations for adjustable inertance tubes. The linear adjustable inertance tube and threaded adjustable inertance tube have been designed, fabricated and experimentally characterized. Both the modified distributed component model and experimental measurements show that the adjustable inertance tube can provide phase angle shift ability for optimizing the performance of the pulse tube cryocooler.

The linear adjustable inertance tube experimental measurements match the distributed component numerical simulation results. The experiment results show that the phase shift is most sensitive to the length changes of the inertance tubes at the lowest frequency, 27 Hz. A maximum phase shift is observed in the mass flow amplitude and acoustic power around 42 Hz, also in agreement with the model. The largest percentage change to the inertance tube length in this linear configuration is limited to only 16% of total length, which limits phase angle shift ability of linear adjustable inertance tube.

Conical and cylindrical threaded adjustable inertance tubes have been explored in order to increase the phase angle shift ability by not only varying the diameter but also

changing the length of inertance tube in the real time during the experiment. The phase angle is very sensitive to the diameter and length of inertance tube. The theoretical model suggests that the threaded cylindrical type of adjustable inertance tube can provide a large phase angle shift ability while maintaining the acoustic power constant. Therefore, the threaded cylindrical adjustable inertance tube has been fabricated and experimentally characterized.

Experimental results show that the phase angle at the inlet of inertance tube can be changed from -2 ° to -30 ° at 60 Hz and -6 ° to -12 ° at 30 Hz. The experimental data matches the modified distributed component model fairly well. The flow channel of the adjustable inertance tube, formed by the gap between the threads of the two screws results in the leaks from the main channel to the average pressure, and the leaks deteriorate the phase angle shift performance of the threaded adjustable inertance tube, as confirmed by the model.

5.3 Future work

Three different adjustable inertance tubes have been explored with the goal of increasing the cooling performance and efficiency of the pulse tube cryocooler. The linear adjustable inertance tube shows its phase angle ability in the real time during the operation, however, its phase angle shift performance is limited by the range of length variation of the linear adjustable inertance tube. The cylindrical threaded adjustable inertance tube provides a large phase shift ability but its performance is deteriorated by the leaks between the threads of the two screws. Various approaches could be used to

reduce the leakage effect, such as increasing the engagement length or connecting the two inertance tubes in parallel.

If the second version of threaded adjustable inertance tube is designed, the long engagement length of the two threads must be implemented to reduce the leakage effect. Because of the long engagement length, it might be more difficult to rotate the outer screw to change the effective length and diameter in the real time. Surface anodizing method could be used to reduce the friction between the two screws. The inner screw could be anodized, leaving the outer screw with hard surface of aluminum, so that the friction effect could be minimized. Besides, since it is a pressure vessel, the charge pressure of the empty chamber is around 300 psig; resulting in a huge pressure difference between the average pressure and pressure in the adjustable inertance tube. Thus, it is relatively hard to rotate the device during the experiment. In order to solve this problem, the recommendation is to enlarge the bottom surface area of the outer screw so that the force could be balanced from top reservoir surface and bottom outer screw surface.

Another way to reduce the leakage effect is to connect the two flow channels formed between the threads, thereby configuring two inertance tubes in parallel. From the theoretical prediction, the parallel inertance tube could dramatically decrease the existing leak effect in the adjustable inertance device, and increase its ability to shift the phase angle.

6 References

1. Gifford, W.E. and R.C. Longsworth, *Pulse-Tube Refrigeration.* Journal of Engineering for Industry, 1964. **86**(3): p. 264-268.
2. Mikulin, E.I., A.A. Tarasov, and M.P. Shrebyonock. *Low temperature expansion pulse tube*. in *Advances in Cryogenics Engineering*. 1984.
3. Richardson, R.N., *Pulse tube refrigerator — an alternative cryocooler?* Cryogenics, 1986. **26**(6): p. 331-340.
4. Zhou, W.J., et al. *The performance of a linear compressor with triangle flexure bearings*. in *Advances in Cryogenics Engineering*. 2011. Spokane, Washington, USA.
5. Zhou, W.J., et al. *The performance comparison of Oxford and triangle flexure bearings*. in *Advances in Cryogenics Engineering*. 2011. Spokane, Washington, USA.
6. Yan, P., *Theoretical and experimental research on a two-stage stirling-type pulse tube cryocooler* Dissertation for the Philosophy Doctoral degree in engineering of Zhejiang University, 2009.
7. Evans, B.E. and R.N. Richardson, *Pulse tube coolers for HTS devices.* Cryogenics, 1997. **37**(10): p. 695-697.
8. Radebaugh R, Zimmerman J, and D.R. S. *A comparison of three types pulse tube refrigerators: new methods of reaching 60K*. in *Advances in Cryogenic Engineering*. 1986: Plenum Press.
9. Zhu, S., W. P, and C. Z, *A single stage double inlet pulse tube refrigerator capable of reaching 42 K*. Cryogenics, 1990. **30**: p. 257-261.
10. Chen, G., et al., *Experimental study on a double-orifice two-stage pulse tube refrigerator*. Cryogenics, 1997. **37**(5): p. 271-273.
11. Wang, C., G. Thummes, and C. Heiden, *Control of DC gas flow in a single-stage double-inlet pulse tube cooler*. Cryogenics, 1998. **38**(8): p. 843-847.
12. Jiang, Y., G. Chen, and G. Thummes. *Experimental investigation on DC flow control in a single-stage pulse tube refrigerator operating below 20 K*. in *ICCR 2003*. 2003. Beijing, China: ICCR'2003 International Academic Publishers.
13. Yuan, K., J. Liang, and Y. Ju. *Experimental investigation of a GM type coaxial pulse tube cryocooler*. in *Cryocooler 12*. 2003: Kluwer Academic/Plenum Publishers.
14. Kanao, K.-i., N. Watanabe, and Y. Kanazawa, *A miniature pulse tube refrigerator for temperatures below 100K.* Cryogenics, 1994. **34**(Supplement 1): p. 167-170.
15. Godshalk K. M., Jin C, and K. Y. *Characterization of 350Hz thermoacoustically driven orifice pulse tube refrigerator with measurements of the phase of the mass flow and pressure*. in *Advances in Cryogenic Engineering*. 1995. Columbus, Ohio, USA: Plenum Press, New York.
16. Gardner, D.L. and G.W. Swift, *Use of inertance in orifice pulse tube refrigerators.* Cryogenics, 1997. **37**(2): p. 117-121.
17. Matsubara, Y. and A. Miyake. *Alternative methods of the orifice pulse tube refrigerator* in *Cryocooler 5*. 1988. Monterey, Carnifonia.
18. Ishizaki, Y. and E. Ishizaki. *Experimental performance of modified pulse tube refrigerator below 80K down to 23K*. in *Cryocooler 7*. 1992. Santa Fe, New Mexico.

19. Tanida, K., et al., *Three-Staged Pulse Tube Refrigerator Controlled by Four-Valve Method*, in *Advances in Cryogenic Engineering*, P. Kittel, Editor. 1996, Springer US. p. 1503-1509.
20. Zhu S, et al. *Phase shift effect of the long neck tube for the pulse tube refrigerator*. in *Cryocooler*. 1996. Waterville Valley, New Hampshire, USA: Plenum Press.
21. West, C.D., *Liquid piston Stirling engines*. 1983: Van Nostrand Reinhold.
22. Tang, K., et al., *A standing-wave thermoacoustic engine with gas-liquid coupling oscillation.* Applied Physics Letters, 2009. **94**(25): p. 254101.
23. Cheadle, M., G. Nellis, and S. Klein, *Analytical model for a pulse tube cryocooler bellows phase shifter and experimental results.* AIP Conference Proceedings, 2012. **1434**(1): p. 1608-1615.
24. Haruyama T and I. H. *Cooling characeristics of a modified miniature pulse tube refrigerator*. in *Advances in Cryogenic Engineering*. 1995. Columbus, Ohio, USA: Plenum Press, New York.
25. Roach, P.R. and K. A. *Pulse tube coolers with an inertance tube : Theory, modeling, and practice*. in *Advances in Cryogenics Engineering*. 1998: Plenum Press, New York.
26. Hofmann, A. and H. Pan, *Phase shifting in pulse tube refrigerators.* Cryogenics, 1999. **39**(6): p. 529-537.
27. Hou Y, Ju Y, and Y. L., *Experimental study on a high frequency miniature pulse tube refrigerator with inertance tube*, in *Advances in Cryogenic Engineering*. 2001, Plenum Press, New York. p. 731-738.
28. Luo, E., R. Radebaugh, and M. Lewis, *Inertance Tube Models and Their Experimental Verification.* AIP Conference Proceedings, 2004. **710**(1): p. 1485-1492.
29. Park, S.J., et al., *An Experimental Study for the Coaxial Inertance Tube Pulse Tube Cryocooler.* AIP Conference Proceedings, 2004. **710**(1): p. 1353-1359.
30. Flake, B. and A. Razani, *Phase Shift and Compressible Fluid Dynamics in Inertance Tubes*, in *Cryocoolers 13*, R.G. Ross, Editor. 2005, Springer US. p. 275-284.
31. Gustafson, S., B. Flake, and A. Razani, *CFD Simulation of Oscillating Flow in an Inertance Tube and its Comparison to Other Models.* AIP Conference Proceedings, 2006. **823**(1): p. 1497-1504.
32. Lewis, M.A., et al. *Measurements of Phase Shifts in an Inertance Tube*. in *Cryocoolers 13*. 2005: Springer US.
33. Lewis, M.A., Bradley, P. E, Radebaugh, R, Gan, Z. H., *Characterization of Inertance Tubes Using Resonance Effects.* Cryocoolers, 2006. **14**: p. 263-270.
34. Lewis, M.A., P.E. Bradley, and R. Radebaugh, *Impedance Measurements of Inertance Tubes.* AIP Conference Proceedings, 2006. **823**(1): p. 1557-1563.
35. Schunk, L.O., G.F. Nellis, and J.M. Pfotenhauer, *Experimental Investigation and Modeling of Inertance Tubes.* Journal of Fluids Engineering, 2005. **127**(5): p. 1029-1037.
36. Dai, W., J. Hu, and E. Luo, *Comparison of two different ways of using inertance tube in a pulse tube cooler.* Cryogenics, 2006. **46**(4): p. 273-277.
37. Matsubara, Y., *Chapter 42 - Future trend of pulse tube cryocooler research*, in *Proceedings of the Twentieth International Cryogenic Engineering Conference (ICEC20)*, Z. Liang, et al., Editors. 2005, Elsevier Science: Oxford. p. 189-196.
38. Gan, Z.H., et al., *A two-stage Stirling-type pulse tube cryocooler with a cold inertance tube.* Cryogenics, 2010. **50**(6–7): p. 426-431.

39. Wang, B., B.Y. Fan, and W.J. Zhou. *Study of a 35 K regenerator performance operating at high frequency*. in *Cryocooler 16*. 2010. Altlanta, Georgia, USA: ICC Press, Boulder, CO.
40. Zhou W. J. , G.Z.H., Zhang X. B. *Clearance loss analysis in linear compressor with CFD Method*. in *Cryocooler 16*. 2010. Atlanta, Georgia, USA.
41. Radebaugh, R. *Development of the pulse tube refrigerator as an efficient and reliable cryocooler*. in *Proc. Institute of Refrigeration*. 2000.
42. Storch, P.J. and R. Radebaugh. *Development and experimental test of an analytical model of the orifice pulse tube refrigerator*. in *Advances in Cryogenics*. 1987. Saint Charles, IL: New York, Plenum Press.
43. Rawlins, W., et al., *Energy Flows in an Orifice Pulse Tube Refrigerator*, in *Advances in Cryogenic Engineering*, P. Kittel, Editor. 1994, Springer US. p. 1449-1456.
44. Ju, Y.L., et al., *Experimental measurements of the flow resistance and inductance of inertance tubes at high acoustic amplitudes.* Cryogenics, 2003. **43**(1): p. 1-7.
45. Bradley, P.E., et al., *Comparison of Measurements and Models for a Pulse Tube Refrigerator to Cool Cryo-Surgical Probes*, in *Cryocoolers 13*, R. Ross, Jr., Editor. 2005, Springer US. p. 671-679.
46. J. M. Pfotenhauer, T. Steiner, and L.M. Qiu. *Continuously Variable Inertance Tubes for Pulse Tube Refrigerators*. in *Cryocoolers*. 2010. Atlanta, Georgia: ICC Press, Boulder, CO.
47. W.J. Zhou and J.M. Pfotenhauer, *Real Time Phase shifting with an Adjustable Inertance Tube*. Cryocoolers, 2012. **17**: p. 229-238.
48. Radebaugh, R., et al. *Proposed rapid cooldown technique for pulse tube cryocoolers*. in *Cryocooler*. 2007: ICC Press, Boulder, CO.
49. Nellis, G. and S. Klein, *Heat Transfer*. 2012, Madison, WI.
50. White, F.M., ed. *Fluid Mechanics*. 7th edition ed. 2009. 425-427.

7 Appendix

7.1 Operation procedure

1. Rotate the outer screw to the top position via the fin heat exchanger on the top surface of the device so that during the experiment, it can be rotate clockwise from the top to the bottom, decreasing the length of large diameter inertance tube;

2. Vacuum the linear compressor and adjustable inertance tube until the vacuum gauge reading is less than 1e-4 torr. Close the valves between the adjustable inertance tube and vacuum pump;

3. Pressurize the device with high purity nitrogen or helium gas. Open the main valve on the nitrogen cylinder, then, open the middle valve on the pressure regulator by rotating it clockwise way to increase the pressure to be around 300 psig. Then, slowly open the last valve on the pressure regulator and watch the pressure rise in the inertance tube from the LabView file called “RC_zhou.vi”; close the valve between adjustable inertance tube and gas cylinder every 50 psi interval to let the pressure inside the device to achieve equilibrium. Continue to open the pressure valve until the pressure in the adjustable inertance tube reaches 300 psig (The reading is from LabView data collecting program.). Then, close the last valve on the pressure gauge and the main valve (first valve) on the pressure gauge.

4. Open the cooling water valves half way which located on the window wall, allowing the cooling water to cool the linear compressor and high temperature nitrogen exiting the linear compressor.

5. Turn on the power controller. Open the main power switch on the wall. Decrease the current on the power controller panel to 0 (or close to 0 AMP) by rotating the pin switch counter clockwise all the way to the end. Then, turn the black power switch on the control panel 90 ° to the "on" position.

6. Slowly increase the current by rotating the current switch counterclockwise way. Watch the pressure ratio for pressure transducer 1 on the LabView program to reach 1.2, then, stop increase the current. Or if the current is higher than 80 Amp, even though the pressure ratio is smaller than 1.2, stop increase the current, because the maximum allowable current for this linear compressor is 80 Amp, 40 Amp for each compressor.

7. The total turns of the outer screw of the adjustable inertance tube is 4.5; therefore, you can rotate half turn each time to collect the data. Taking the pressure data at 60 Hz and then rotate the frequency switch on the control panel to change the operation frequency to 57Hz. Decrease the frequency from 60 Hz to 30 Hz, 3 Hz each intervals to collect the pressure data from three pressure transducers.

8. After taking all the data, goes to shut down procedure. Decrease the current switch to 0 AMP by slowly rotating the switch counterclockwise way to the end. Move the black power switch on the control panel to "Off" position. Close the cooling water valve on the window wall. Release the pressure in the adjustable inertance tube by

open the releasing valve connected to the linear compressor inlet. Lower the vacuum jar to protect the equipment from dust.

7.2 MATLAB code of the model

Distributed Component Model

```
% Distributed component model matlab version, Wenjie Zhou
% Feb. 27, 2013
%% Function: DCM_12 function used to find the required length and acoustic power.
function[theta_compressor,W]=DCM_12(L1,D1)

% set up constant
Pbar = 2068427.19;  % Mean pressure [Pa]
DP = 228010;        % pressure amplitude, [pa]
% L1 = 2.5;          % lenght of inertance tube, [m]
% D1 = 0.003505;      % outer diameter of the tube [m]
R_ent = 0;          % measured entrance effect
V_res = 1e-3;       % volume of the resevoir [m^3]
freq = 50;          % frequency of the compressor [Hz]
Tbar = 293;         % average temperature [K]
Rg = 2077;          % molarmass of helium [J/kg-K]
cpg = 5192;         % specific heat at constant pressure of helium [J/kg-K]
k = cpg/(cpg-Rg);   % ratio of cp/cv at adiabatic boundary condition
mu = 1.968e-5;      % viscosity of helium [Pa-s]
rho = Pbar/(Rg*Tbar);% ideal gas desity [kg/m^3]
omega = 2*pi*freq;   % angular velocity [rad/s]


L_line1=4*L1/(pi*D1^2);            %Inertance of the entire 1st section of line
C_res=V_res/(k*Rg*Tbar);           %Reservoir compliance
Zr=(1/(1i*omega*C_res));           %Reservoir impedance of compliance
C_line1=pi*D1^2*L1/(4*k*Rg*Tbar);   %Compliance of entire 1st section of tube


%%
N = 100;                           % number of nodes
%Calculate the compliances and their impedance
Z_Cn1=(1/(1i*omega*C_line1/(N)));       %Impedance of the compliance of one
increment
Z_L1=1i*omega*L_line1/N;           %Impedance of the inertance of one increment


%set initial values of Re_old
for index = 1:N
   Re_old(index) = 1.204e6;
end
```

```
%% iteration method begin
%%%%%%%%%%%%%%%%%%%%%%%%%%%%%%%
epsilon = 1e-8;                %converge criteria
delta = 1;                     %difference between P(k+1) and P(k)
number  = 8000;                  %number of iteration
k          = 0;
while (delta > epsilon)
   k = k+1;
   if (k > number)
      disp('No Converge');
   end
   delta = 0.0;

% calculate the first node: node 1
   m_dot_mag(1)= Re_old(1)/(8/(pi^2*2*D1*mu));   % Calculate the resistance 1st
element
   f(1) = 0.046*Re_old(1)^(-0.2);           % Calculate the friction factor 1st element"
   R(1)=f(1)*64*m_dot_mag(1)*L1/N/(pi^3*rho*D1^5);         %Impedance of the
resistance of 1st increment
   Zrl(1)=R(1)+Z_L1;                             % Impedance of Resistance and inertance
combined

%Set up entire impedance starting from the inside"
   Z_res=R_ent+Zr;                          %Total reservoir impedance (including entrance
effect)
   Z_s(1)=Z_res+Zrl(1);                   % First impedance in series
   Z_p(1)=(Z_s(1)^(-1)+Z_Cn1^(-1))^(-1);   %% First impedance in parallel

% calculate the node from 2 to N
for do = 2:N
   m_dot_mag(do) = Re_old(do)/(8/(pi^2*2*D1*mu));   % Calculate the mass flow
magnitude
   f(do) = 0.046*Re_old(do)^(-0.2);                   % Calculate the friction factor 1st
element"
   R(do)=f(do)*64*m_dot_mag(do)*L1/N/(pi^3*rho*D1^5);      %Impedance of the
resistance of 1st increment
   Zrl(do)=R(do)+Z_L1;                           % Impedance of Resistance and inertance
combined
   Z_s(do)=Z_p(do-1)+Zrl(do);                 %Impedance in series
   Z_p(do)=(Z_s(do)^(-1)+Z_Cn1^(-1))^(-1);     %Impedance in parallel
%%%%%%%%%%%%%%%%%%%%%%%%%%%%%%%%%
 %%%%%%%%%%%%%%%%%%%
end
%change index of pressure and mass flow from 1 to N
   P_s(1)= DP;                              %Pressure drop across elements
```

```
   m_dot_c_s(1) = DP/Z_Cn1;                % mass flow through the compliance
   m_dot_s(1)=DP/Z_p(N);                   %Calculate mass flow at inertance inlet
   m_dot_mag_s(1)= abs(m_dot_s(1));        %Mass flow Magnitudes
   Re_s(1)=m_dot_mag_s(1)*8/(pi^2*2*D1*mu);       % Calculate the resistance per
element
   delta = delta + abs(Re_s(1)-Re_old(N));        % calculate the error between Re_old
and Re_s

for do = 2:N
   m_dot_s(do) = m_dot_s(do-1)-m_dot_c_s(do-1);    %Kirchhoffs Law
   P_s(do)=  P_s(do-1)-m_dot_s(do)*Zrl(N-do+1);              %Pressure drop across
elements
   m_dot_c_s(do)=P_s(do)/Z_Cn1;                    %Mass flow accumulated in the
elements
   m_dot_mag_s(do)= abs(m_dot_s(do));        %Mass flow Magnitudes
   Re_s(do)=m_dot_mag_s(do)*8/(pi^2*2*D1*mu);        % Calculate the resistance
per element
   delta = delta + abs(Re_s(do)-Re_old(N-do+1));
end
% update the Re_old
for index = 1:N
   Re_old(index) = Re_s(N-index+1);
end

   delta = delta/(N)

end
%% end of iteration method to find m_dot(1)

m_dot_compressor=m_dot_mag_s(1);          %Mass flow at compressor outlet
m_dot_reservoir=m_dot_mag_s(N);           %Mass flow into reservoir
theta_compressor =-angle(Z_p(N))*180/pi;     %Phase angle of impedance
W=0.5*Rg*Tbar/Pbar*m_dot_mag_s(1)*DP*cos(theta_compressor*pi/180);  %Acco
ustic power

end
```

Modified Distributed Component Model

```
% calculate properties based on nitrogen
% Lossy Distributed component model matlab version, Wenjie Zhou
% two sections of inertance tube
% Feb. 27, 2015
% Function: generate the function DCM_10 to calculate two section inertance tubes
% clear all;clc;
% function[theta_compressor,W]=DCM_10_2leak7_ent(L2,freq)
function[theta_compressor,W]=DCM_10_2leak7_ent(L2,freq)
% function[m_dot_compressor,m_leak_total]=DCM_10_2leak6(L2,th_leak)
% function[v_leak_first,m_leak_total]=DCM_10_2leak6(L2,th_leak)

% set up constant
Pbar = 2192532.82 ;  % Mean pressure [Pa] 318psi  2192532.82  1825042.26
Pr = 1.2;           %pressure ratio in the experiment
DP = Pbar*(Pr-1)/(Pr+1); % pressure amplitude, [pa]
L1 = 1.737;         % lenght of inertance tube, [m]1.372;
D1 = 0.006927;      % inner diameter of the tube [m]
% % % L2 = 1.86;        % length of inertance tube section 2 [m]
D2 = 0.01016;     % inner diameter of the tube section 2 [m]
R_ent = 5.7e6;      % measured entrance effect, DP/m_dot at reservior5.7e6
V_res = 2e-3;     % volume of the resevoir [m^3]
% % % freq = 60;        % frequency of the compressor [Hz]
Tbar = 300;       % average temperature [K]
Rg = 296.8;       % molarmass of n2 [J/kg-K]
cpg = 1038;       % specific heat at constant pressure of helium [J/kg-K]
k_gas = cpg/(cpg-Rg);   % ratio of cp/cv at adiabatic boundary condition
mu = 1.82e-5;     % viscosity of n2 [Pa-s], 1.744e5 for helium
rho = Pbar/(Rg*Tbar);% ideal gas desity [kg/m^3]
omega = 2*pi*freq;   % angular velocity [rad/s]

C_res=V_res/(k_gas*Rg*Tbar);          %Reservoir compliance
Zr=(1/(1i*omega*C_res));          %Reservoir impedance of compliance

C_line1=pi*D1^2*L1/(4*k_gas*Rg*Tbar);    %Compliance of entire 1st section of
tube
L_line1=4*L1/(pi*D1^2);           %Inertance of the entire 1st section of line

C_line2=pi*D2^2*L2/(4*k_gas*Rg*Tbar);    %Compliance of entire 2st section of
tube
L_line2=4*L2/(pi*D2^2);           %Inertance of the entire 2st section of line
%%
N = 100;                      % number of nodes
%Calculate the compliances and their impedance
Z_Cn1=(1/(1i*omega*C_line1/(N/2)));      %Impedance of the compliance of one
increment
```

```
Z_L1=1i*omega*L_line1/(N/2);                %Impedance of the inertance of one
increment

Z_Cn2=(1/(1i*omega*C_line2/(N/2)));     %Impedance of the compliance of one
increment
Z_L2=1i*omega*L_line2/(N/2);                %Impedance of the inertance of one
increment

%dimensions of leak
th_leak = 21.5e-6; %[m]
D_leak = 2*th_leak;
L_leak_small = 13.7e-3; %length of the small leak
L_leak_large = 4.8e-3;      %length of large leak
width_leak_large = 3.725/2;   %width of large leak, 2 leak passage in parallel
width_leak_small = 3.474/2;   %width of small leak


%set initial values of Re_old
for index = 1:N
    Re_old(index) = 1.204e6;
    v_leak_old(index) = 100; %assume velocity through leak
    DP_or(index) = DP/2;
end

%considering the entrance effect
%small leak first, nodes from resevoir%
d_2_or              = D_leak;                        %effective diameter of leak%
d_1_or              = D1;                    %diameter of the inertance tube%
A_2_or_small= th_leak*width_leak_small/(N/2);                %area   of   the   small
leak%
A_2_or_large= th_leak*width_leak_large/(N/2);           %area of the large leak%
beta_or      = d_2_or/d_1_or;                  %ratio of the diameter %
F_or                = sqrt(1/(1-beta_or^4));          %velocity of approach factor %



%% iteration method begin
%%%%%%%%%%%%%%%%%%%%%%%%%%%%%%%%%%%%%%%%%%%%%%%%%%%%%%%%%%%%%%%%
epsilon = 1e-7;                  %converge criteria
delta = 1;                        %difference between (k+1) and (k)
number  = 8000;                   %number of iteration
k           = 0;
while (delta > epsilon)
    k = k+1;
    if (k > number)
        disp('No Converge');
```

```
    end
    delta = 0.0;



% calculate the first node of first section of IT: node 1
    m_dot_mag(1)= Re_old(1)/(8/(pi^2*2*D1*mu));  % Calculate the resistance 1st element
    f(1) = 0.046*Re_old(1)^(-0.2);          % Calculate the friction factor 1st element"
    R(1)=f(1)*64*m_dot_mag(1)*L1/(N/2)/(pi^3*rho*D1^5);      %Impedance of the resistance of 1st increment
    Zrl(1)=R(1)+Z_L1;                        % Impedance of Resistance and inertance combined

    Re_leak(1) = rho*v_leak_old(1)*D_leak/mu;
    f_leak(1) = 308.78/Re_leak(1);    %laminar flow
    R_leak(1) = 1/2*v_leak_old(1)*f_leak(1)*L_leak_small/(D_leak*th_leak*width_leak_small);
    Z_leak(1) = R_leak(1)*N/2;  %start from small leak

    % calculate the entrance effect through the leak
    Y_or(1)= 1-(.41+.35*beta_or^4)*(DP_or(1))/(k_gas*(Pbar+DP_or(1)));%compressibility factor%
    C_d_or(1)= 0.5959+.0312*beta_or^2.1-.184*beta_or^8+91.71*beta_or^2.5*Re_leak(1)^(-.75)+.0389*beta_or^4/(1-beta_or^4)-.0158*beta_or^3; %discharge coefficient%
    %leak resistance
    Z_or(1)= DP_or(1)/(C_d_or(1)*Y_or(1)*F_or*A_2_or_small*sqrt(2*rho*DP_or(1)));



%Set up entire impedance starting from the inside
    Z_res=R_ent+Zr;                  %Total reservoir impedance (including entrance effect)
    Z_s(1)=Z_res+Zrl(1);             % First impedance in series
    Z_p(1)=(Z_s(1)^(-1)+Z_Cn1^(-1)+1/(Z_leak(1)+Z_or(1))+1/(Z_leak(1)+Z_or(1)))^(-1);     %% First impedance in parallel

% calculate the node from 2 to N/2

for do = 2:(N/2)

    Re_leak(do) = rho*v_leak_old(do)*D_leak/mu;
    f_leak(do) = 308.78/Re_leak(do);    %laminar flow
```

```
   R_leak(do)                                                                          =
1/2*v_leak_old(do)*f_leak(do)*L_leak_small/(D_leak*th_leak*width_leak_small);
   Z_leak(do) = R_leak(do)*N/2;  %start from small leak

   % calculate the entrance effect through the leak
   Y_or(do)=                                                                          1-
(.41+.35*beta_or^4)*(DP_or(do))/(k_gas*(Pbar+DP_or(do)));%compressibility
factor%
   C_d_or(do)=                                        0.5959+.0312*beta_or^2.1-
.184*beta_or^8+91.71*beta_or^2.5*Re_leak(do)^(-.75)+.0389*beta_or^4/(1-
beta_or^4)-.0158*beta_or^3; %orifice discharge coefficient%
   %leak resistance
   Z_or(do)=
DP_or(do)/(C_d_or(do)*Y_or(do)*F_or*A_2_or_small*sqrt(2*rho*DP_or(do)));


   m_dot_mag(do) = Re_old(do)/(8/(pi^2*2*D1*mu));   % Calculate the mass flow
magnitude
   f(do) = 0.046*Re_old(do)^(-0.2);                 % Calculate the friction factor 1st
element"
   R(do)=f(do)*64*m_dot_mag(do)*L1/(N/2)/(pi^3*rho*D1^5);   %Impedance of the
resistance of 1st increment
   Zrl(do)=R(do)+Z_L1;                          % Impedance of Resistance and inertance
combined
   Z_s(do)=Z_p(do-1)+Zrl(do);                 %Impedance in series
   Z_p(do)=(Z_s(do)^(-1)+Z_Cn1^(-
1)+1/(Z_leak(do)+Z_or(do))+1/(Z_leak(do)+Z_or(do)))^(-1);             %Impedance  in
parallel
% % % % % % % % % % % % % % % % % % % % % % % % % % % % % % % % % %
 % % % % % % % % % % % % % % % % % %
end
% calculate the node from N/2+1 to N
for do = (N/2+1):N

   Re_leak(do) = rho*v_leak_old(do)*D_leak/mu;
   f_leak(do) = 308.78/Re_leak(do);    %laminar flow
   R_leak(do)                                                                          =
1/2*v_leak_old(do)*f_leak(do)*L_leak_large/(D_leak*th_leak*width_leak_large);
   Z_leak(do) = R_leak(do)*N/2;  %start from small leak

   % calculate the entrance effect through the leak
   Y_or(do)=                                                                          1-
(.41+.35*beta_or^4)*(DP_or(do))/(k_gas*(Pbar+DP_or(do)));%compressibility
factor%
```

```
   C_d_or(do)= 0.5959+.0312*beta_or^2.1-
.184*beta_or^8+91.71*beta_or^2.5*Re_leak(do)^(-.75)+.0389*beta_or^4/(1-
beta_or^4)-.0158*beta_or^3; %orifice discharge coefficient%
   %leak resistance
   Z_or(do)=
DP_or(do)/(C_d_or(do)*Y_or(do)*F_or*A_2_or_large*sqrt(2*rho*DP_or(do)));

   m_dot_mag(do) = Re_old(do)/(8/(pi^2*2*D2*mu)); % Calculate the mass flow
magnitude
   f(do) = 0.046*Re_old(do)^(-0.2); % Calculate the friction factor 1st
element"
   R(do)=f(do)*64*m_dot_mag(do)*L2/(N/2)/(pi^3*rho*D2^5); %Impedance of the
resistance of 1st increment
   Zrl(do)=R(do)+Z_L2; % Impedance of Resistance and inertance
combined
   Z_s(do)=Z_p(do-1)+Zrl(do); %Impedance in series
   Z_p(do)=(Z_s(do)^(-1)+Z_Cn2^(-
1)+1/(Z_leak(do)+Z_or(do))+1/(Z_leak(do)+Z_or(do)))^(-1); %Impedance in
parallel
% % % % % % % % % % % % % % % % % % % % % % % % % % % % % % % % %
 % % % % % % % % % % % % % % % % % %
end
%change index of pressure and mass flow from 1 to N
   P_s(1)= DP; %Pressure drop across elements
   m_dot_c_s(1) = DP/Z_Cn2; % mass flow through the compliance
   m_dot_leak(1) = (DP/(Z_leak(N)+Z_or(N))); %mass flow through the leak
   DP_or_new(1) = abs(m_dot_leak(1)*Z_or(N));
   v_leak_new(1) = abs(m_dot_leak(1)/rho/(th_leak*width_leak_large/(N/2)));
   m_dot_s(1)=DP/Z_p(N); %Calculate mass flow at inertance inlet
   m_dot_mag_s(1)= abs(m_dot_s(1)); %Mass flow Magnitudes
   Re_s(1)=m_dot_mag_s(1)*8/(pi^2*2*D2*mu); % Calculate the new Renoyld
per element
   delta = delta + (abs(Re_s(1)-Re_old(N))+ abs(v_leak_new(1)-
v_leak_old(N))+abs(DP_or_new(1)-DP_or(N)))/3;

for do = 2:(N/2)
   m_dot_s(do) = m_dot_s(do-1)-m_dot_c_s(do-1)-2*m_dot_leak(do-
1); %Kirchhoffs Law
   P_s(do)= P_s(do-1)-m_dot_s(do)*Zrl(N-do+1); %Pressure drop across
elements
   m_dot_c_s(do)=P_s(do)/Z_Cn2; %Mass flow accumulated in the
elements
   m_dot_leak(do) = (P_s(do)/(Z_leak(N-do+1)+Z_or(N-do+1))); %mass flow
through leak
   DP_or_new(do) = abs(m_dot_leak(do)*Z_or(N-do+1));
   v_leak_new(do) = abs(m_dot_leak(do)/rho/(th_leak*width_leak_large/(N/2)));
```

```
   m_dot_mag_s(do)= abs(m_dot_s(do));            %Mass flow Magnitudes
   Re_s(do)=m_dot_mag_s(do)*8/(pi^2*2*D2*mu);        % Calculate the resistance per element
   delta = delta + (abs(Re_s(do)-Re_old(N-do+1))+ abs(v_leak_new(do)-v_leak_old(N-do+1))+abs(DP_or_new(do)-DP_or(N-do+1)))/3;
end

for do = (N/2+1):N
   m_dot_s(do) = m_dot_s(do-1)-m_dot_c_s(do-1)-2*m_dot_leak(do-1);  %Kirchhoffs Law
   P_s(do)= P_s(do-1)-m_dot_s(do)*Zrl(N-do+1);              %Pressure drop across elements
   m_dot_c_s(do)=P_s(do)/Z_Cn1;                    %Mass flow accumulated in the elements
   m_dot_leak(do) = (P_s(do)/(Z_leak(N-do+1)+Z_or(N-do+1)));
   DP_or_new(do) = abs(m_dot_leak(do)*Z_or(N-do+1));
   v_leak_new(do) = abs(m_dot_leak(do)/rho/(th_leak*width_leak_small/(N/2)));
   m_dot_mag_s(do)= abs(m_dot_s(do));            %Mass flow Magnitudes
   Re_s(do)=m_dot_mag_s(do)*8/(pi^2*2*D1*mu);        % Calculate the resistance per element
   delta = delta + (abs(Re_s(do)-Re_old(N-do+1))+abs(v_leak_new(do)-v_leak_old(N-do+1))+abs(DP_or_new(do)-DP_or(N-do+1)))/3;
end

% update the Re_old
for index = 1:N
   Re_old(index) = Re_s(N-index+1);
   v_leak_old(index) = v_leak_new(N-index+1);
   DP_or(index) = abs(DP_or_new(N-index+1));
end

   delta = delta/N

end
% % % % % % % % % % % % % % %
%% end of iteration method to find m_dot(1)

m_dot_compressor=m_dot_mag_s(1);            %Mass flow at compressor outlet
m_dot_reservoir=m_dot_mag_s(N);             %Mass flow into reservoir
theta_compressor = -angle(Z_p(N))*180/pi;    %Phase angle of impedance
W=0.5*Rg*Tbar/Pbar*m_dot_mag_s(1)*DP*cos(theta_compressor*pi/180);  %Acoustic power


m_leak_total = sum(abs(m_dot_leak));
m_leak_first = abs(m_dot_leak(1));
```

```
v_leak_first = v_leak_new(1);


end


This code is use to run the Modified Distributed Component Model above
% Distributed component model matlab version, Wenjie Zhou
% Feb. 27, 2015
%% DCS mode, length of IT changes from 2m to 3 m
%% DCS model, diameter of IT changes from 0.006m to 0.013m
%% Function: run_DCM_10. run two sections inertance tubes, D1 D2 and L1 L2.
clear;
clc;

NN = 40;    % number of the length segements
MM = 16;     % number of the diameter segements, Dia = 0.005m, 0.01m

% Length2=linspace(0.005,1.863,NN)'; %1.53
Length2=linspace(0.005,1.86,NN)';
% Diameter1=linspace(0.0069,0.014,MM)';
% th_leak =linspace(1e-6,35e-6,MM)';
th_leak =[18;20;22;24;27;30;33;36;39;42;45;48;51;54;57;60];

for i=1:NN
   for j=1:MM
      [angle,power]=DCM_10_2leak7_ent_beta(Length2(i),th_leak(j));
      angle_k(i,j)=angle;
      power_k(i,j)=power;
   end
end

figure (1);
plot(Length2,angle_k,'-v','LineWidth',2,...
            'MarkerEdgeColor','k',...
            'MarkerFaceColor','g',...
            'MarkerSize',2);
legend ('18','20','22','24');
title('phase angle vs. Length of IT','fontsize',16);
xlabel('Length of IT(m)','fontsize',12,'fontweight','b');
ylabel('phase angle at inlet (degree)','fontsize',12,'fontweight','b');
grid on;

figure (2);
plot(Length2,power_k,'-.*','LineWidth',2,...
            'MarkerEdgeColor','k',...
```

```
            'MarkerFaceColor','g',...
            'MarkerSize',4);
legend ('18','20','22','24','27');
title('acoustic power vs. length of IT','fontsize',16);
xlabel('Length of IT(m)','fontsize',12,'fontweight','b');
ylabel('Acoustic power (W)','fontsize',12,'fontweight','b');
grid on;
```

The code is the Adjustable Inertance Tube Design Approach

```
function[Wacerr]=fWac(D,L,Wac_t)
[theta,W_dot_ac]=DCM_12(L,D);
Wacerr=Wac_t-W_dot_ac;
End


function[D,theta]=findD(L,Wac,Dg)
OPTIONS = optimset('Display','iter');
D=fzero(@(D) fWac(D,L,Wac),Dg,OPTIONS);
[theta,W_dot_ac]=DCM_12(L,D);
End


%% Function: call findD.m and fWac.m to calculate diameter and phase angle
MM = 10;
W_dot_ac=linspace(100,1500,MM)';
Lv=linspace(1,2.5,MM)';
Dg=0.003;
for i =1:MM
   for j=1:MM
   [Dv(i,j),thetav(i,j)]=findD(Lv(i),W_dot_ac(j),Dg);
   Dg=Dv(i,j);
   end
end



%% Function: call findD.m using new length and acoustic power to find new
diameter
% and new theta.
function[Dv,thetav]=DCMLW_12(W_dot_ac,Lv)
% W_dot_ac=500;
% Lv=2.0;
Dg=0.003;
[Dv,thetav]=findD(Lv,W_dot_ac,Dg);
Dg=Dv;
end


%% find the theta error between the old one and new one.
function[thetaerr]=ftheta2(Lv,W_dot_ac,theta_t)
   [Dv,thetav]=DCMLW_12(W_dot_ac,Lv);
   thetaerr=theta_t-thetav;
end
```

```
%% find the theta error between the old one and new one.
function[thetaerr]=ftheta2(Lv,W_dot_ac,theta_t)
   [Dv,thetav]=DCMLW_12(W_dot_ac,Lv);
   thetaerr=theta_t-thetav;
end


%% A function to use Acoustic Power and phase to find the length and Diameter
function[L,D]=findL2(W_dot_ac,theta_t,Lg)
   OPTIONS = optimset('Display','iter');
   L=fzero(@(L) ftheta2(L,W_dot_ac,theta_t),Lg,OPTIONS);
   [D,thetav]=DCMLW_12(W_dot_ac,L);
End



%% Use Acoustic Power and Phase to find Length and diameter
%% Function: run_DCMLW_12.m. using theta W to find L and D.
clear all;
MM = 10;
W_dot_ac=linspace(100,1500,MM)';
theta=linspace(-30,-60,MM)';
Lg=2.5;
for i = 1:MM
   for j=1:MM
   [Lx(i,j),Dx(i,j)]=findL2(W_dot_ac(i),theta(j),Lg);
   Lg=Lx(i,j);
   W(i,j) = W_dot_ac(i);
   the(i,j) = theta(j);
   end
end
figure (1);
[~,h] = contour(Lx,Dx,W,'LineWidth',2);
set(h,'ShowText','on','TextStep',get(h,'LevelStep'));
xlabel('Length of IT(m)','fontsize',12,'fontweight','b');
ylabel('Diameter of IT(m)','fontsize',12,'fontweight','b');
grid on;
hold on;
[~,h] = contour(Lx,Dx,the,'LineWidth',2);
set(h,'ShowText','on','TextStep',get(h,'LevelStep'));
xlabel('Length of IT(m)','fontsize',12,'fontweight','b');
ylabel('Diameter of IT(m)','fontsize',12,'fontweight','b');
grid on;
```

7.3 Drawings of the main pieces

1 Assembly

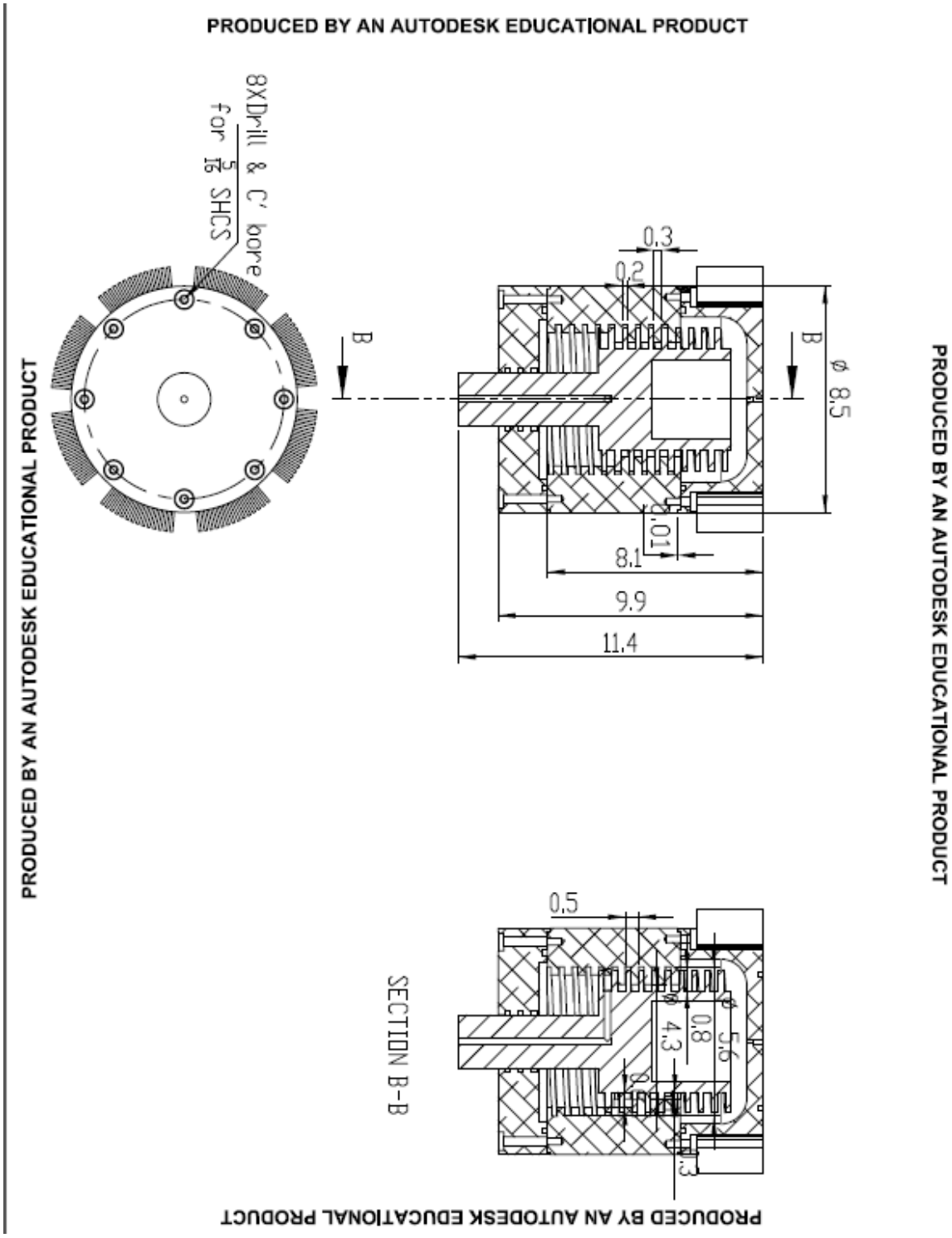

2. Top cover with fin heat exchanger

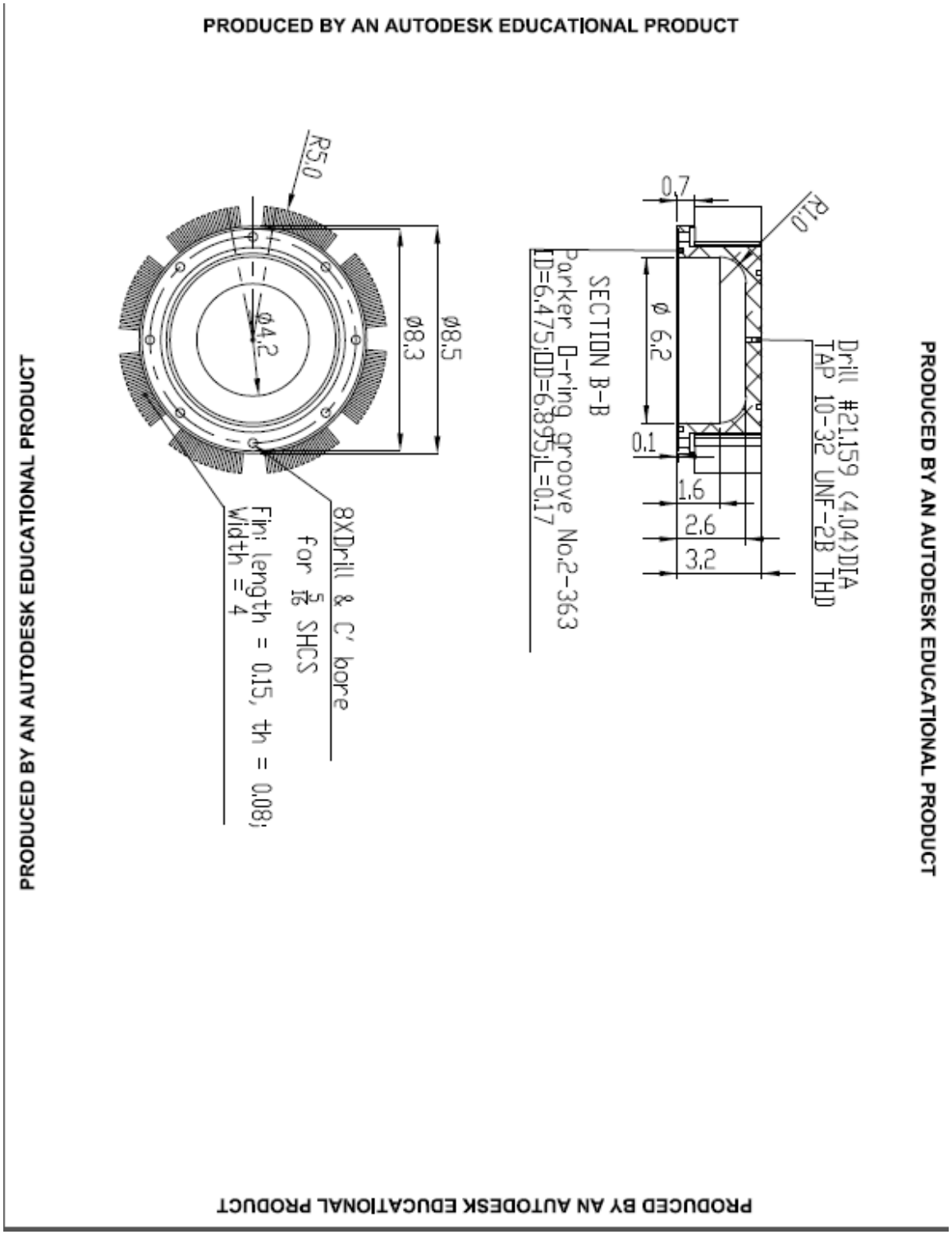

3. Flange connnecting linear compressor to adjustable inertance tube

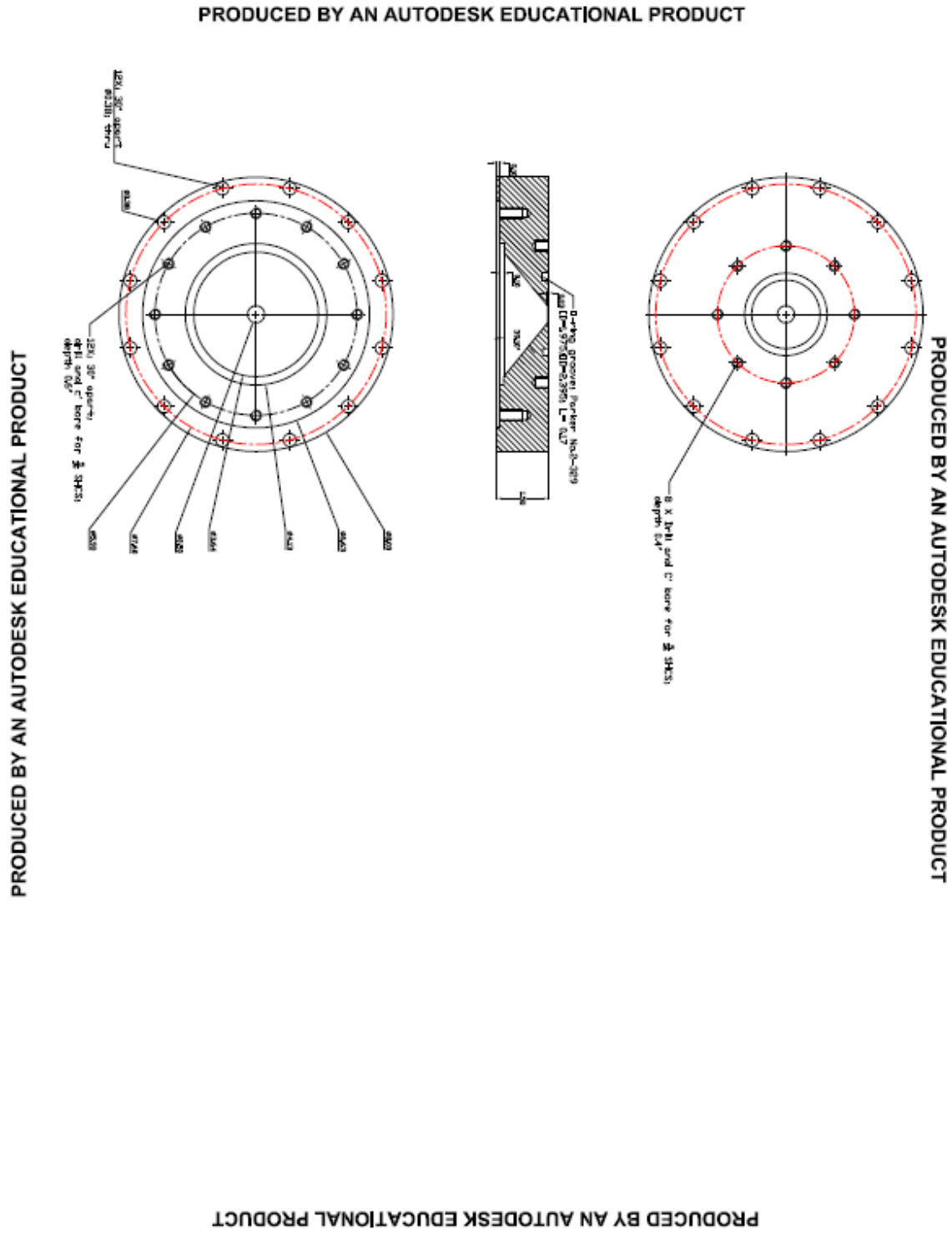

4. Support flange

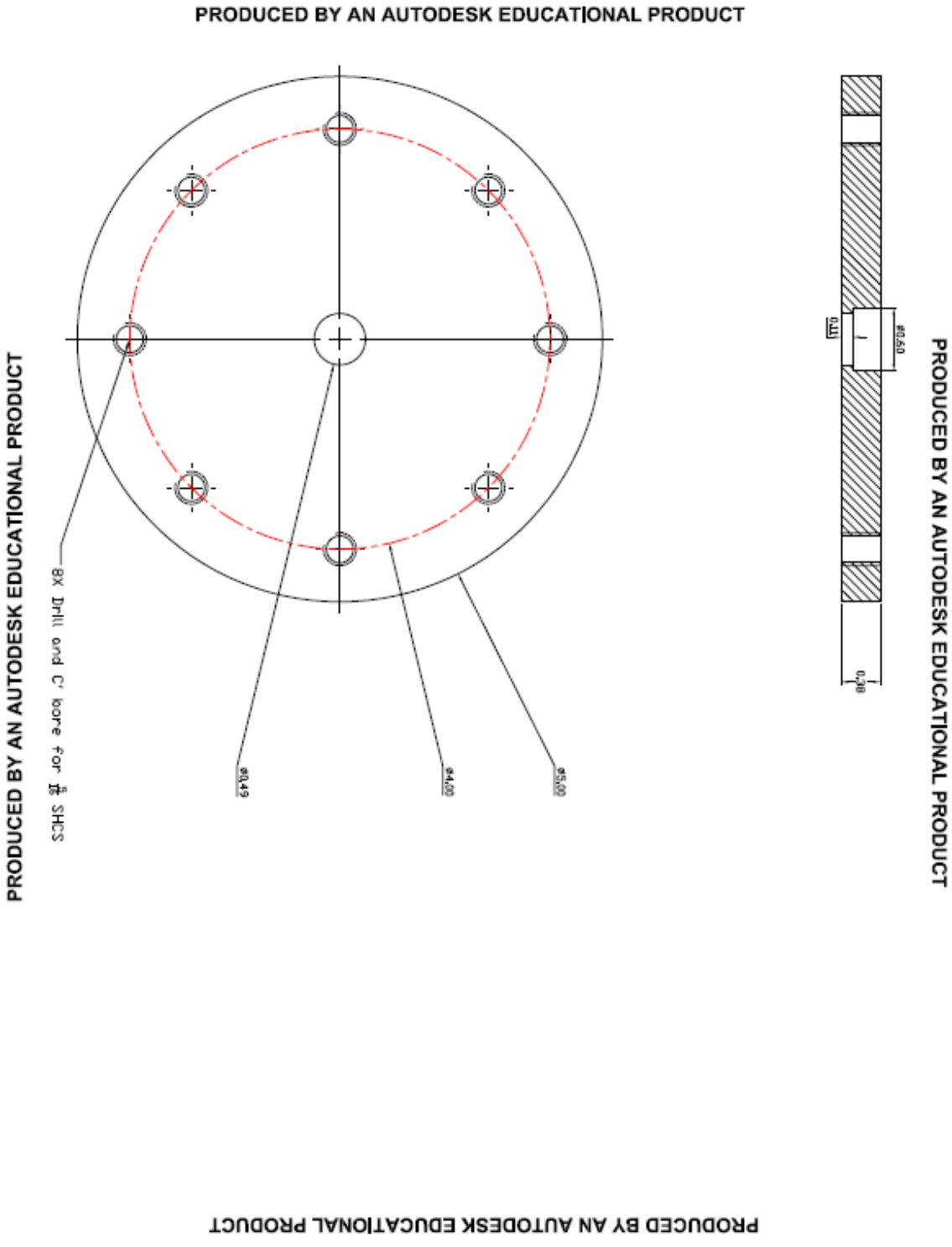

5. Inner screw

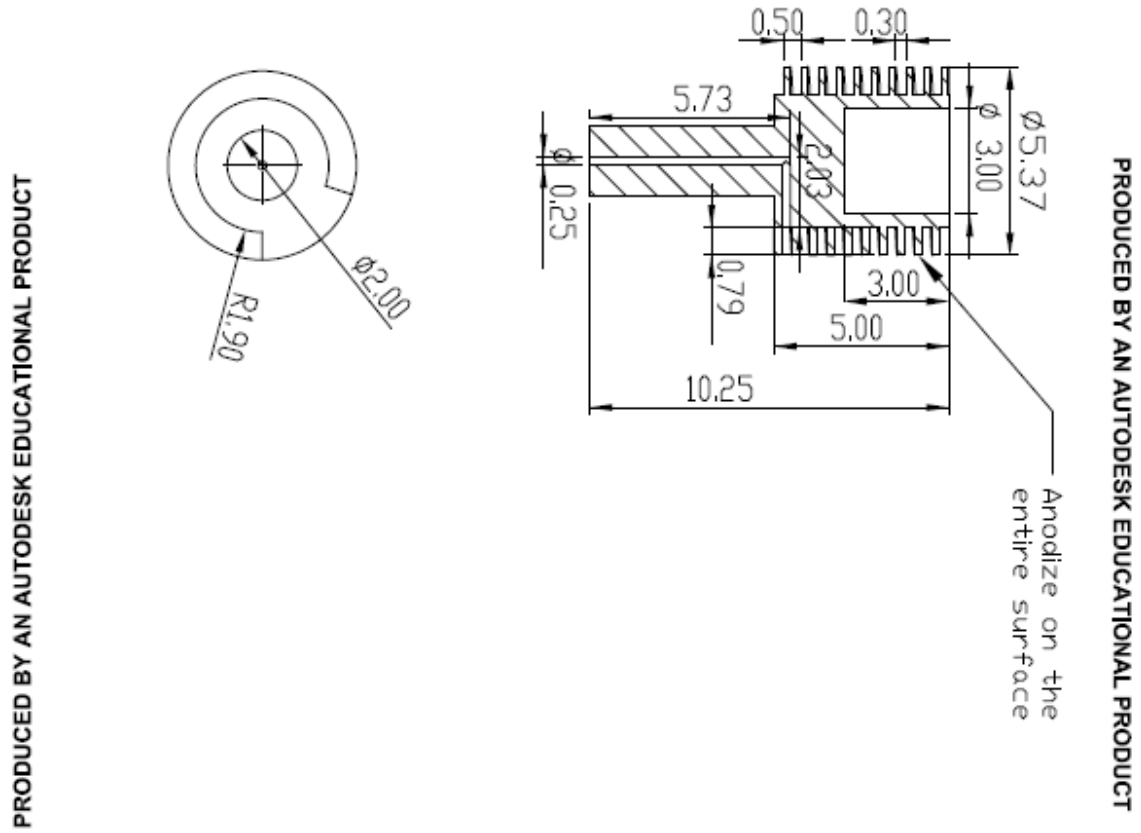

6. Outer screw

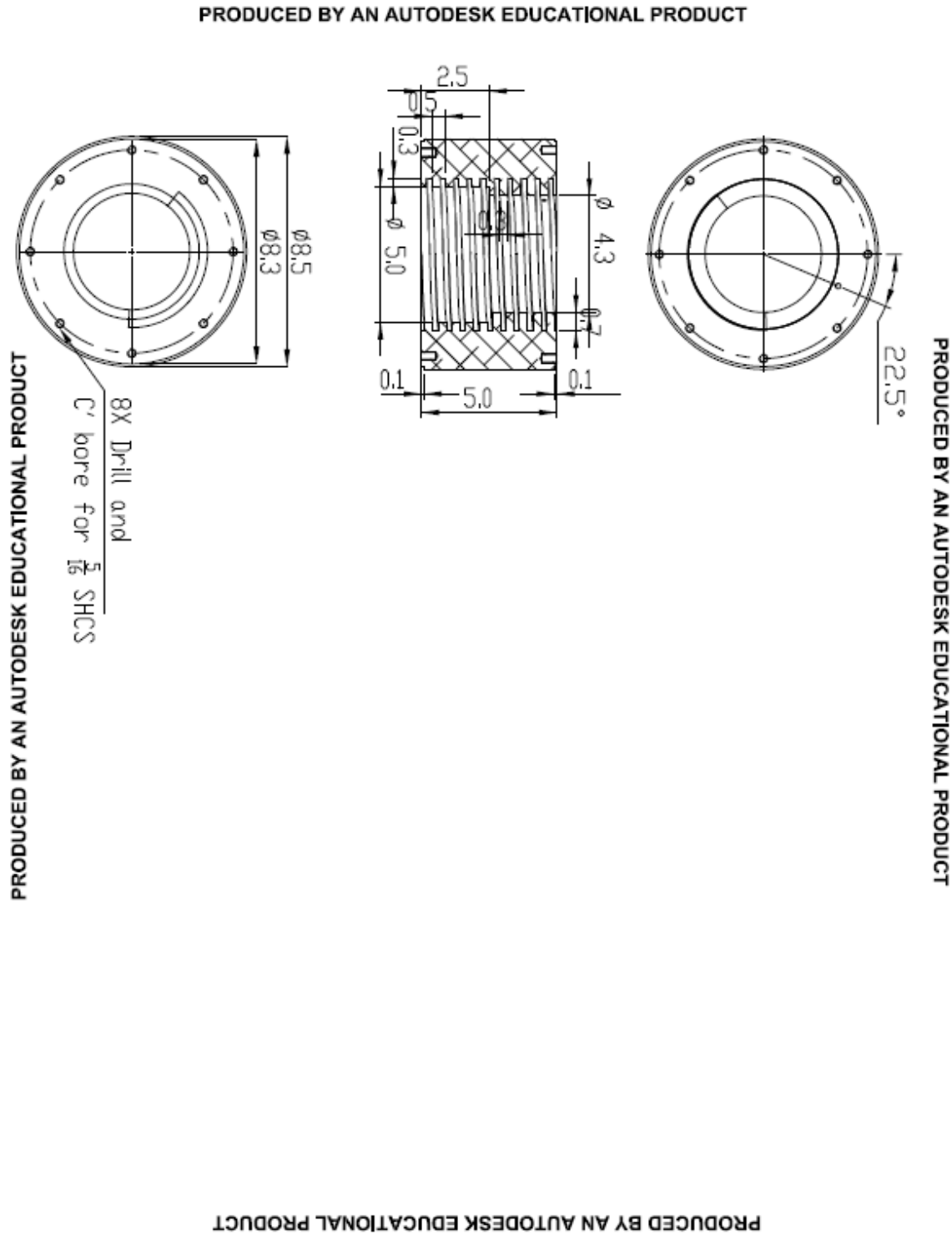

7. Bottom cover to seal the adjusable inertance tube from ambient